Title
Hydrogeology of Ridge-flank Hydrothermal Systems

Author
Winslow, Dustin Mathew

Publication Date
2015

UNIVERSITY OF CALIFORNIA
SANTA CRUZ

HYDROGEOLOGY OF RIDGE-FLANK HYDROTHERMAL SYSTEMS

A dissertation submitted in partial satisfaction
of the requirements for the degree of

DOCTOR OF PHILOSOPHY

in

EARTH SCIENCES

by

Dustin M. Winslow

June 2015

This dissertation of Dustin M. Winslow
is approved:

Professor Andrew T. Fisher, Chair

Professor Slawek Tulaczyk

Professor Gary Glatzmaier

Professor Herbert Lee

Tyrus Miller
Vice Provost and Dean of Graduate Studies

TABLE OF CONTENTS

1.1 Introduction

1.2 Analytic methods

1.3 Results

1.4 Discussion

FIGURES and TABLES

Chapter 1. Characterizing borehole fluid flow and formation permeability in the ocean crust using linked analytic models and Markov chain Monte Carlo analysis

Chapter 2. Sustainability and dynamics of outcrop-to-outcrop hydrothermal circulation

Chapter 3. Three-dimensional modeling of hydrothermal outcrop-to-outcrop circulation on the eastern flank of the Juan de Fuca ridge

ABSTRACT

Hydrogeology of ridge-flank hydrothermal systems

Dustin M. Winslow

Most of the hydrothermal circulation through the ocean crust, in terms of mass, heat, and many solute fluxes, occurs on ridge-flanks. Far from the magmatic influence of mid-ocean ridges, fluid flow is driven by lithospheric heating from below and channeled through volcanic rock outcrops that serve as high-permeability conduits between the ocean and the underlying volcanic crust. Field data in this setting is sparse due to difficulties associated with accessing these remote locations, making geologically accurate modeling particularly valuable to assessing the nature of ridge-flank hydrothermal circulation. Each study in this thesis applies a combination of modeling and field observations to constrain the hydrogeologic properties and behaviors of ridge-flank hydrothermal systems, including: (1) deriving permeability estimates from flowing subsea boreholes, (2) investigating the sustainability of outcrop-to-outcrop hydrothermal flow, and (3) constraining the properties and behaviors on a well-studied outcrop-to-outcrop system. In the first study, thermal records from flowing boreholes in young oceanic crust are used to assess borehole and formation properties, including permeability, using analytic equations and a Markov chain Monte Carlo analysis to quantify uncertainty. We find the median bulk permeability at all sites to be between 0.4 to 1.5 x 10^{-11} m^2, with a standard deviation of 0.2 to 0.3 log-cycles at each borehole. These results are remarkably homogenous, given the much larger variability in permeability measurements in the oceanic crust. Results from the second study illuminate the controls on hydrogeologic sustainability, flow rate, and preferred flow direction in outcrop-to-outcrop hydrothermal systems. We find that sustained flow between outcrops over tens of kilometers depends on a contrast in transmittance (the product of outcrop permeability and the area of outcrop exposure) between recharging and discharging sites, and that discharge is favored through less transmissive outcrops. These systems require aquifer permeability values ranging from 10^{-12} to 10^{-11} m^2, consistent with field measurements and values inferred from the first chapter. In the third study, a suite of three-dimensional numerical simulations are used to characterize and constrain the permeability and thickness of the upper crustal aquifer, the permeability of outcrops, and the potential for multiple discharging outcrops and azimuthal permeability anisotropy to influence hydrothermal processes at a field site on the eastern flank of the Juan de Fuca Ridge.

ACKNOWLEDGEMENTS and DEDICATION

Many thanks to my adviser, Andrew Fisher, for his support and patience, and for the good times we shared working on fascinating problems. I would also like to acknowledge P. Stauffer, C. Gable, and G. Zyvoloski for their assistance with configuring, running, and interpreting models, and my committee members S.Tulaczyk, G. Glatzmaier, and H. Lee for improving this work with thoughtful and insightful feedback over the years.

In dedication to my grandparents, who made this all possible.

Lynda E. Martin and Robert L. Lessley

INTRODUCTION

This thesis explores ridge-flank hydrothermal circulation from three distinct perspectives. The first chapter applies Bayesian statistical methods to thermal logs taken in flowing subsea boreholes in order to estimate the permeability and other hydrologic properties of the ocean crust. This method improves on previous work by providing rigorous error estimates for properties and processes associated with these field experiments. In the second study, I use three-dimensional numerical simulations to characterize mechanisms and properties controlling outcrop-to-outcrop hydrothermal circulation in ridge-flank environments. In the third chapter, I apply similar numerical techniques to a well-studied outcrop-to-outcrop hydrothermal system on the eastern flank of the Juan de Fuca Ridge in order to identify the heat and fluid flow behavior, and constrain hydrologic property ranges, that are present at the site. Though each study is distinct in the approach used and problems addressed, all results contribute to our understanding of the hydrogeology of the ocean crust on ridge flanks. The conditions and properties inferred with these simulations comprise crucial controls on seafloor hydrothermal systems across the seafloor, and this work constitutes a significant step in the characterization of these systems globally.

Seafloor hydrothermal circulation influences processes throughout the global ocean, modifying ocean chemistry [*Elderfield and Schultz*, 1996; *Wheat and Mottl*, 2004], lithospheric heat flux budgets [*Stein and Stein*, 1992], the physical state and evolution of oceanic crust, as well as a diversity of biology both above and within the crust

[*Cowen et al.*, 2003; *Edwards et al.*, 2011]. This thesis focuses on studies of ridge-flank hydrothermal systems, found far from mid-ocean ridges and characterized by relatively cooler flows (5 – 100 ºC) than those found at seafloor spreading centers. Despite lower temperatures, ridge-flank systems cover significantly larger areas and involve considerably greater contributions to fluid, heat, and some geochemical fluxes. Volumetric fluxes of water through ridge-flank hydrothermal systems are commensurate with global riverine discharge, and contribute global geochemical fluxes comparable to or in excess of those from riverine fluxes for many elements [*Elderfield and Schultz*, 1996; *Wheat and Mottl*, 2000]. These flows also carry enough heat to account for 70% of the deficit in the global lithospheric heat budget, about 25% of the earth's total heat loss, as estimated from cooling plate models [*Stein and Stein*, 1992; *Fisher*, 2005].

Sediment cover on ridge-flanks is often thick and regionally extensive, and can restrict the exchange of hydrothermal fluids between the water column and underlying the crust. In such cases, seamounts and other areas of crustal exposure (outcrops) provide high-permeability conduits that allow flows to bypass relatively impermeable sediments [*Baker et al.*, 1991; *Fisher and Becker*, 2000; *Villinger et al.*, 2002; *Fisher et al.*, 2003b]. With two or more outcrops connecting the underlying volcanic crust to the overlying ocean, self-sustaining outcrop-to-outcrop flow systems can develop, driving significant heat, fluid, and solute fluxes over tens of kilometers between outcrops [*Fisher et al.*, 2003a, 2003b; *Hutnak et al.*, 2008; *Anderson et al.*, 2012]. Outcrop-to-outcrop flow is driven by escaping lithospheric heat and operates by means of a “hydrothermal siphon,” which is established when thermal differences between recharging and discharging fluids create a differential pressure large enough to generate flow through the intervening crust. The physics of outcrop-to-outcrop hydrothermal siphons, including the nature of heat and fluid flow patterns and crustal permeability structure, are the focus of the second and third chapters of this thesis.

Large scale, international and multidisciplinary studies of the deep biosphere, hydrogeology, geochemistry, tectonics, crustal composition and alteration are underway in hydrothermal systems around the world, including a site on the eastern flank of the Juan de Fuca Ridge that is featured in each chapter of this thesis. Field data collected for these systems is relatively sparse, due to the difficulty and cost associated with deep-sea research, making the application of statistically rigorous and geologically accurate models particularly important. Measurements and estimates of crustal properties in this area are limited, yet comprise much of the global dataset. The first chapter of my thesis adds to this dataset by linking analytical models with a rigorous statistical framework. These systems have not previously been modeled in three-dimensions using a coupled-flow code (fluid, heat), and idealizations used in earlier numerical and analytical work make it difficult to interpret the properties of a connected regional flow network within the crust. State of the art models are presented in Chapters 2 and 3 of my thesis. As work in all fields at these sites is dependent on a careful understanding of hydrothermal flows, developing the next generation of quantitative models is essential for understanding these integrated subsea biogeochemical systems.

Each chapter contributes to our understanding of ridge-flank hydrothermal systems by constraining the permeability structure in the ocean crust and identifying primary controls on heat and fluid flow in hydrothermal systems. These studies each address unique research questions, but are connected in terms of overarching research goals and similarities in the relevant physics, methods applied, and setting. In each case, the careful application of modeling techniques to sparse field data provided valuable insight into the properties and dynamics that characterize ridge-flank hydrothermal systems.

References

Anderson, B. W., L. A. Coogan, and K. M. Gillis (2012), The role of outcrop-to-outcrop fluid flow in off-axis oceanic hydrothermal systems under abyssal sedimentation conditions, *J. Geophys. Res.*, *117*(B5), doi:10.1029/2011JB009052.

Baker, P., P. Stout, M. Kastner, and H. Elderfield (1991), Large-scale lateral advection of seawater through oceanic-crust in the central equatorial pacific, *Earth Planet. Sci. Lett.*, *105*(4), 522–533, doi:10.1016/0012-821X(91)90189-O.

Cowen, J. P., S. J. Giovannoni, F. Kenig, H. P. Johnson, D. Butterfield, M. S. Rappe, M. Hutnak, and P. Lam (2003), Fluids from aging ocean crust that support microbial life, *Science*, *299*(5603), 120–123, doi:10.1126/science.1075653.

Edwards, K. J., C. G. Wheat, and J. B. Sylvan (2011), Under the sea: microbial life in volcanic oceanic crust, *Nat. Rev. Microbiol.*, *9*(10), 703–712.

Elderfield, H., and A. Schultz (1996), Mid-ocean ridge hydrothermal fluxes and the chemical composition of the ocean, *Annu. Rev. Earth Planet. Sci.*, *24*, 191–224.

Fisher, A. T. (2005), Marine hydrogeology: recent accomplishments and future opportunities, *Hydrogeol. J.*, *13*(1), 69–97, doi:10.1007/s10040-004-0400-y.

Fisher, A. T., and K. Becker (2000), Channelized fluid flow in oceanic crust reconciles heat-flow and permeability data, *Nature*, *403*(6765), 71–74, doi:10.1038/47463.

Fisher, A. T., C. A. Stein, R. N. Harris, K. Wang, E. A. Silver, M. Pfender, M. Hutnak, A. Cherkaoui, R. Bodzin, and H. Villinger (2003a), Abrupt thermal transition reveals hydrothermal boundary and role of seamounts within the Cocos Plate, *Geophys. Res. Lett.*, *30*(11), 1550, doi:10.1029/2002GL016766.

Fisher, A. T. et al. (2003b), Hydrothermal recharge and discharge across 50 km guided by seamounts on a young ridge flank, *Nature*, *421*(6923), 618–621, doi:10.1038/nature01352.

Hutnak, M., A. T. Fisher, R. Harris, C. Stein, K. Wang, G. Spinelli, M. Schindler, H. Villinger, and E. Silver (2008), Large heat and fluid fluxes driven through mid-plate outcrops on ocean crust, *Nat. Geosci.*, *1*(9), 611–614, doi:10.1038/ngeo264.

Stein, C., and S. Stein (1992), A model for the global variation in oceanic depth and heat-flow with lithospheric age, *Nature*, *359*(6391), 123–129, doi:10.1038/359123a0.

Villinger, H., I. Grevemeyer, N. Kaul, J. Hauschild, and M. Pfender (2002), Hydrothermal heat flux through aged oceanic crust: where does the heat escape?, *Earth Planet. Sci. Lett.*, *202*(1), 159–170, doi:10.1016/S0012-821X(02)00759-8.

Wheat, C. G., and M. J. Mottl (2000), Composition of pore and spring waters from Baby Bare: Global implications of geochemical fluxes from a ridge flank hydrothermal system, *Geochim. Cosmochim. Acta*, *64*(4), 629–642, doi:10.1016/S0016-7037(99)00347-6.

Wheat, C. G., and M. J. Mottl (2004), Geochemical fluxes through mid-ocean ridge flanks, in *Hydrogeology of the Oceanic Lithosphere*, edited by E. E. Davis and H. Elderfield, pp. 627–658, Cambridge University Press, Cambridge, UK.

Chapter One

CHARACTERIZING BOREHOLE FLUID FLOW AND FORMATION PERMEABILITY IN THE OCEAN CRUST USING LINKED ANALYTIC MODELS AND MARKOV CHAIN MONTE CARLO ANALYSIS

Published: Winslow, D. M., A. T. Fisher, and K. Becker (2013), Characterizing borehole fluid flow and formation permeability in the ocean crust using linked analytic models and Markov chain Monte Carlo analysis: Borehole Flow and Formation Permeability, *Geochemistry, Geophysics, Geosystems*, *14*(9), 3857–3874, doi:10.1002/ggge.20241.

Geochemistry Geophysics Geosystems G^3

Published by AGU and the Geochemical Society

Article
Volume 14, Number 9
23 September 2013
doi: 10.1002/ggge.20241
ISSN: 1525-2027

Characterizing borehole fluid flow and formation permeability in the ocean crust using linked analytic models and Markov chain Monte Carlo analysis

D. M. Winslow
Earth and Planetary Sciences Department, University of California, Santa Cruz, California, USA

A. T. Fisher
Earth and Planetary Sciences Department, University of California, Santa Cruz, California, USA

Institute for Geophysics and Planetary Physics, University of California, Santa Cruz, California, USA

K. Becker
Rosenstiel School of Marine and Atmospheric Science, University of Miami, Miami, Florida, USA

[1] Thermal records from boreholes in young oceanic crust, in which water is flowing up or down, are used to assess formation and borehole flow properties using three analytic equations that describe the transient thermal and barometric influence of downhole or uphole flow. We link these calculations with an iterative model and apply Markov chain Monte Carlo (MCMC) analysis to quantify ranges of possible values. The model is applied to two data sets interpreted in previous studies, from Deep Sea Drilling Project Hole 504B on the southern flank of the Costa Rica Rift and Ocean Drilling Program Hole 1026B on the eastern flank of the Juan de Fuca Ridge, and to two new records collected in Integrated Ocean Drilling Program Holes U1301A and U1301B, also on the eastern flank of the Juan de Fuca Ridge. Our calculations indicate that fluid flow rates when thermal logs were collected were $\sim$2 L/s in Holes 504B, 1026B, and U1301A, and >20 L/s in Hole U1301B. The median bulk permeabilities determined with MCMC analyses are 4 to 7×10^{-12} m^2 around the uppermost parts of Holes 504B, 1026B, and U1301A, and 1.5×10^{-11} m^2 around a deeper section of Hole U1301B, with a standard deviation of 0.2 to 0.3 log cycles at each borehole. The consistency of permeability values inferred from these four holes is surprising, given the range of values determined globally and the tendency for permeability to be highly variable in fractured crystalline rock formations such as the upper oceanic crust.

Components: 13,615 words, 8 figures, 3 tables.

Keywords: hydrothermal circulation; fluid flow; heat flow; Markov chain Monte Carlo; permeability; ocean crust.

Index Terms: 3017 Hydrothermal systems: Marine Geology and Geophysics; 3021 Marine hydrogeology: Marine Geology and Geophysics; 3036 Ocean drilling: Marine Geology and Geophysics; 0450 Hydrothermal systems: Biogeosciences; 1034 Hydrothermal systems: Geochemistry; 3616 Hydrothermal systems: Mineralogy and Petrology; 4832 Hydrothermal systems: Oceanography: Biological and Chemical; 8135 Hydrothermal systems: Tectonophysics; 8424 Hydrothermal systems: Volcanology; 1847 Modeling: Hydrology; 1873 Uncertainty assessment: Hydrology; 1952 Modeling: Informatics; 1990 Uncertainty: Informatics; 4316 Physical modeling: Natural Hazards; 3275 Uncertainty quantification: Mathematical Geophysics.

Received 15 May 2013; **Revised** 25 July 2013; **Accepted** 5 August 2013; **Published** 23 September 2013.

D. M. Winslow, A. T. Fisher, and K. Becker (2013), Characterizing borehole fluid flow and formation permeability in the ocean crust using linked analytic models and Markov chain Monte Carlo analysis, *Geochem. Geophys. Geosyst.*, *14*, 3857 3874, doi:10.1002/ggge.20241.

1. Introduction

1.1. Motivation and Project Goal

[2] Volumetric fluxes of water through ridge-flank hydrothermal systems are commensurate with global riverine discharge [*Mottl*, 2003], advecting enough heat to account for 70% of the deficit in the oceanic lithospheric heat budget [e.g., *Stein et al.*, 1995]. Seafloor hydrothermal circulation impacts processes throughout the global ocean, modifying ocean chemistry [*Edmond et al.*, 1979; *Elderfield and Schultz*, 1996], lithospheric heat budgets [e.g., *Davis and Lister*, 1977], the physical state and evolution of oceanic crust [*Jacobson*, 1992], and biology both above and within the crust [*Edwards et al.*, 2011; *Kelley et al.*, 2002]. Hydrothermal flows are controlled in large part by the permeability structure (magnitude and connectivity) of the crust, which has been tested directly at relatively few subseafloor locations [e.g., *Becker*, 1990].

[3] Direct measurements of permeability in the volcanic ocean crust are difficult and expensive to perform, requiring a borehole to be drilled through seafloor sediments and into the basement rocks below. Core recovery is often low in fractured crystalline rocks, and permeability analyses of core samples may not be characteristic of larger scales [*Civan*, 2001; *Clauser*, 1992]. Single-hole packer tests, the simplest form of in-situ test, involve actively pumping into a borehole while monitoring the pressure response in the same hole. The requirement that a ship be onsite throughout active pumping limits the duration of such tests during ocean drilling, typically restricting the radial extent to which the test is sensitive to the near-borehole environment [*Becker and Davis*, 2003; *Fisher*, 1998].

[4] Temperature records in flowing seafloor boreholes (i.e., those with fluid flowing downward from, or upward to, the seafloor) can also be used to infer crustal permeability [*Becker and Davis*, 2003; *Becker et al.*, 1983; *Fisher et al.*, 1997]. Thermal data can be collected months to years after a borehole is drilled, allowing assessment of permeability at a scale larger than that associated with single-hole packer tests. Thermal analyses can be used to assess additional physical characteristics in and near the borehole, such as the borehole radius, aquifer thickness, aquifer compressibility, and sediment thermal conductivity. Some prior knowledge of these parameters is required, but the thermal history can inform understanding of these terms through the use of statistically based inverse modeling techniques.

[5] We introduce two fundamental improvements to traditional analyses of borehole properties based on thermal logs from flowing crustal boreholes in the deep ocean. First, we connect three separate analytic heat and fluid flow models, directly linking the borehole thermal state, fluid properties, and flow to/from the surrounding formation to find simultaneous, self-consistent solutions. Second, we treat uncertain physical parameters as distributions, rather than single values, allowing development of the range of possible flow parameters and formation and borehole properties.

[6] In the next section of this paper, we describe the nature of boreholes drilled into the volcanic ocean crust, and introduce four borehole locations where the thermal data used in this study were acquired. We apply the linked analytic and statistical approach to data from these boreholes, and compare the results to earlier analyses of thermal data and other observations used to assess crustal conditions.

1.2. Experimental Operations and Settings

1.2.1. Borehole Configurations, Operations, and Thermal Data

[7] Subsea boreholes drilled into the upper volcanic crust, which is generally porous and permeable, are usually located below a conductive boundary layer of less permeable marine sediments. These sediments help to stabilize the drill string and can support a reentry cone at the seafloor that permits repeated bit changes, installation of casing, and other operations needed to achieve penetration below the upper tens of meters of volcanic rock. Surface seawater is pumped into the borehole as a drilling fluid to lubricate the bit and remove cuttings from the hole, and may also be pumped during coring, casing, and other

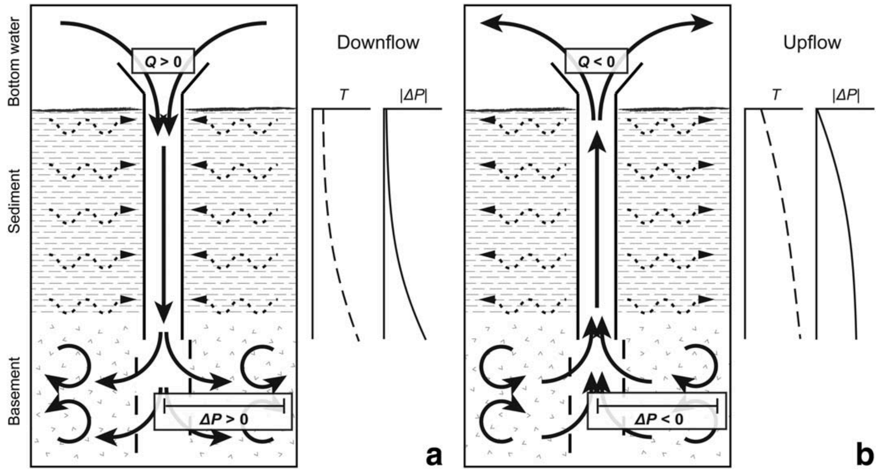

Figure 1. (a) Downhole flow into borehole driven by differential pressure between the borehole and formation, with example theoretical thermal profile resulting from conductive heating of borehole fluids by surrounding sediments. Solid arrows show fluid flow, and dashed arrows show heat flow. ΔP is the driving pressure forcing water into or out of the formation, calculated with equation (2), relative to the pressure of bottom water at the seafloor. (b) Upflow from naturally pressurized formation to seafloor, using the same symbols as in Figure 1a. Thermal profiles are inverted relative to the downhole case as warm formation fluids lose heat conductively as they ascend. In both examples, there is vigorous convection in basement rocks surrounding the borehole, but the most permeable part of the formation need not be the shallowest basaltic crust.

operations. The initially warm surface seawater used as drilling fluid cools considerably during descent to the seafloor (often 2–5 km), as the drill pipe is an efficient heat exchanger. As a result, fluids pumped into the seafloor generally have a lower temperature than formation fluids adjacent to the borehole, as is common during deep crustal drilling in general [e.g., *Becker et al.*, 1983; *Jaeger*, 1961; *Langseth*, 1990]. The imposition of a tall column of cold (dense) seawater in the borehole adjacent to warmer (less dense) formation fluid creates a positive differential pressure that can drive borehole fluid into the formation, even where the formation is naturally overpressured relative to ambient hydrostatic. In many boreholes, self-sustained downflow continues for days to years, until the borehole is plugged to prevent inflow of bottom seawater [e.g., *Becker et al.*, 2001; *Gable et al.*, 1992] (Figure 1).

[8] Prior to drilling, geothermal conditions in marine sediments above volcanic basement rocks tend to be conductive, with heat flowing from depth to the seafloor. Heat transport is usually conductive in marine sediments because sediment permeability and natural driving forces are generally too small to allow fluid flow at thermally significant rates, particularly where sediment thickness is greater than a few tens of meters [*Davis*, 1988; *Fisher*, 2004; *Spinelli et al.*, 2004]. In contrast, conditions in boreholes drilled and cased through sediments and into volcanic crust are often nonconductive because of fluid flow up or down the borehole. If this flow were extremely rapid, it could lead to isothermal conditions in the borehole. In practice, there is generally significant lateral exchange of heat between the borehole and the surrounding formation (Figure 1). The balance of vertical heat advection and lateral heat conduction generally results in a curved thermal profile with depth, the shape of which depends on several parameters: the predrilling geothermal gradient, thermal properties of the fluid and surrounding formation, size of the borehole and casing, and the direction, rate and duration of fluid flow (Figure 1) [*Becker et al.*, 1983; *Lesem et al.*, 1957].

[9] When fluid flow is downward, formation heat flows inward, warming the water as it descends. If a natural formation overpressure exceeds the differential pressure created during downflow, the flow direction can reverse [*Becker and Davis*, 2004; *Fisher et al.*, 1997; *Wheat et al.*, 2010]. Then warm borehole fluids rising from depth lose heat to the sediments surrounding casing during ascent toward the seafloor. The resulting borehole

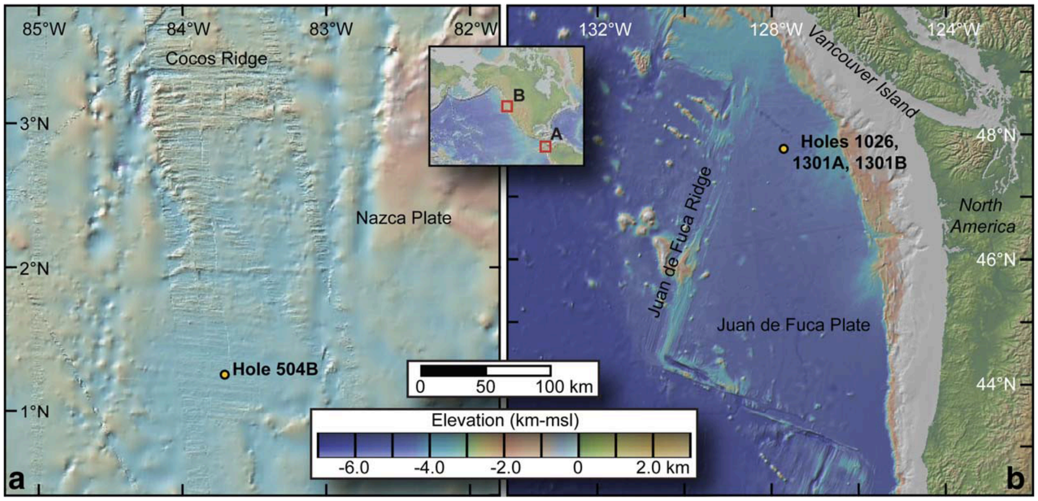

Figure 2. Regional maps showing (a) Hole 504B on the southern flank of the Costa Rica Rift in the eastern equatorial Pacific Ocean and (b) Sites 1026 and U1301 on the eastern flank of the Juan de Fuca Ridge in the northeastern Pacific Ocean.

thermal profile has opposite curvature to that caused by downward flow (Figure 1).

[10] The temperature records used in this study were recovered from Deep Sea Drilling Project (DSDP) Hole 504B, Ocean Drilling Project (ODP) Hole 1026B, and Integrated Ocean Drilling Project (IODP) Holes U1301A and U1301B (Figure 2 and Table 1), all of which have demonstrated clear evidence of sustained fluid flow when the holes were not sealed (Figure 3). Temperature data from Holes 504B and 1026B were analyzed in previous studies [e.g., *Becker et al.*, 1983, 2004, 1985; *Fisher et al.*, 1997; *Gable et al.*, 1989; *Guerin et al.*, 1996], but we revisit earlier interpretations to assess the impact of methods introduced in the present paper, and to compare results from multiple sites that share common characteristics. In addition, we present and interpret new borehole thermal data collected from Holes U1301A and U1301B using long-term, borehole observatories.

1.2.2. Hole 504B

[11] DSDP Site 504 is located in 5.9 Myr old crust on the southern flank of the medium-spreading-rate Costa Rica Rift, where sediment thickness is 274 m above volcanic basement (Figure 2 and Table 1). Hole 504B was drilled in 1979 on DSDP Leg 69 to assess the physical and chemical state of young oceanic crust, and has been revisited, deepened, sampled, and monitored for decades [e.g., *Anderson et al.*, 1982; *Becker et al.*, 2004, 1985; *Costa Rica Rift United Scientific Team*, 1982]. Hole 504B was drilled much deeper than other subsea boreholes that existed at the time, eventually penetrating 2111 m below the seafloor (mbsf) and 1836 m subbasement (msb); Hole 504B holds significant historical importance as one of the first well-sampled windows into the formation, structure, and alteration of the oceanic crust [e.g., *Alt et al.*, 1986; *Anderson et al.*, 1982; *Becker et al.*, 1989].

Table 1. Hole Locations and Specifications

	Hole 504B	Hole 1026B	Hole U1301A	Hole U1301B
Longitude	01°13.63′N	47°45.757′N	47°45.210′ N	47°45.228′N
Latitude	83°43.81′W	127°45.548′W	127°45.833′W	127°45.827′W
Seafloor depth [a] (mbsl)	3460	2658	2667	2668
Sediment thickness (m)	274.5	247	262	265
Total depth [a] (mbsf)	489	295[b]	370	582
Total depth [a] (msb)	214.5[b]	48[b]	108	318

[a] Abbreviations: mbsl, meters below sea level; mbsf, meters below seafloor; msb, meters subbasement.

[b] Total depth shown for Hole 504B is that from the time when the thermal log analyzed in this study was collected. The hole was deepened considerably during subsequent expeditions.

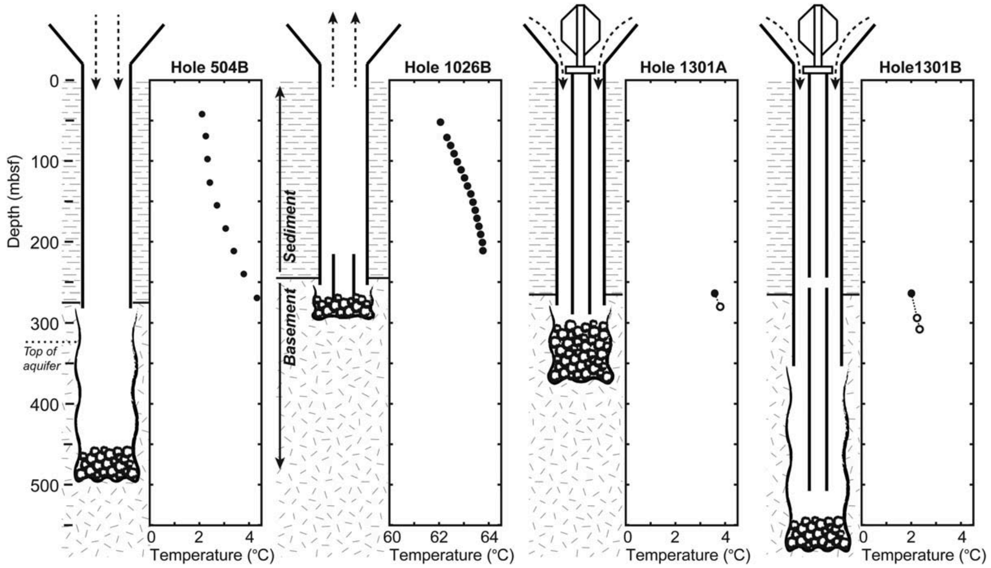

Figure 3. Schematic hole completion diagrams and thermal data used for modeling. Note that temperature scale for Hole1026B differs from those used for other holes. Rubble texture shows extent of backfill due to borehole collapse prior to thermal measurements. Temperature logs in Holes 504B and 1026B were recorded in open hole, whereas records from Holes U1301A and U1301B were obtained during deployments of autonomous temperature loggers within unsealed borehole observatories (open circles). As discussed in the text, a record from one probe was used for analysis of Hole 1301A, whereas records from two tools were used to assess conditions in Hole 1301B (Figure 4). Thermal data from these holes were extrapolated back to the sediment-basement interface to develop a constraint for modeling (closed circles), based on heat flow measured at the site during IODP Expedition 301 and regional surveys [*Davis et al.*, 1997a, 1992; *Fisher et al.*, 2005].

[12] The thermal state of Hole 504B has been measured repeatedly with downhole temperature tools. These logs show clear evidence for continued downflow of bottom water into basement rocks below casing, but changes in the thermal profile over time indicate a complex flow history. The initial thermal log from DSDP Leg 70, taken 2 months after Hole 504B was first drilled, indicated rapid downflow [*Becker et al.*, 1983], but borehole thermal logs from approximately 2, 3, and 7 years later (DSDP Legs 83 and 92 and ODP Leg 111) indicated progressively slower downflow with time [*Becker et al.*, 1985; *Gable et al.*, 1989]. A borehole temperature log taken twelve years after initial drilling (ODP Leg 137) indicated faster downflow than inferred from the previous two logs [*Gable et al.*, 1995], a transient behavior that remains enigmatic. In the present study, we interpret only the thermal record taken from DSDP Leg 70 (Figure 3), comprising 10 measurements made at 28 m intervals in the cased sedimentary section of the borehole, collected after the first 1–2 months of continuous downflow.

1.2.3. Hole 1026B

[13] ODP Site 1026 is located in 3.5 Myr old crust ~100 km east of the intermediate spreading-rate Endeavor segment of the Juan de Fuca Ridge (Figure 2 and Table 1). The area is characterized by thick sediments overlying relatively young crust, due to high sedimentation rates and the infilling of turbidites above abyssal hill topography. Hole 1026B was drilled in 1996 on ODP Leg 168 as part of an east-west crustal age transect [*Davis et al.*, 1997b]. Although the hole was initially drilled through 247 m of sediments and 52 m into volcanic rocks, upper basement was unstable. A “liner” of drillpipe was drilled into the rubble at the bottom of the hole to keep the hole from collapsing before installation of a long-term borehole observatory (CORK) [*Davis et al.*, 1997b]. A thermal log collected 13 days later using an autonomous temperature probe lowered by wireline showed that warm formation fluid was moving rapidly up the hole from depth, indicating that the natural formation overpressure had overcome the differential pressure induced by drilling and other

operations [*Fisher et al.*, 1997] (Figure 3). This log consists of 16 measurements made at 10 m intervals in the cased hole within the sedimentary section, and represents conditions after 1–3 weeks of upflow following the flow reversal by overpressured formation fluids. Because this hole was not monitored during the interim period, the time of reversal and the duration of upflow prior to the thermal log are uncertain.

1.2.4. Holes U1301A and U1301B

[14] Holes U1301A and U1301B were drilled in 2004 on IODP Expedition 301 into 3.5 Myr old crust on the eastern flank of the Juan de Fuca Ridge, ~1 km south of Hole 1026B, through 262–265 m of sediments (Figure 2 and Table 1). These holes were drilled just 36 m apart, with the intent of creating sealed borehole observatories that monitor distinct basement intervals. Following completion of drilling, casing, coring, and short-term experiments, the holes were fitted with CORKs to measure pressure and temperature, and to sample formation fluids and microbial materials at depth [*Fisher et al.*, 2005]. Unfortunately, the CORKs in Holes U1301A and U1301B were not sealed as planned, allowing cold bottom water to flow downhole through annular gaps in the casing for several years following CORK installation [*Fisher et al.*, 2008]. The flow down Hole U1301A reversed abruptly about 3 years after CORK installation, and the flow down Hole U1301B was stopped after 5 years when the gaps between casing strings around the CORK wellhead were cemented [*Fisher*, 2010; *Wheat et al.*, 2010].

[15] Instrument strings deployed in both CORKs included autonomous temperature probes, collecting thermal data at fixed depths during deployments of 4–5 years. These data, recovered in 2009 and 2010, show significant short-term variability in borehole temperatures resulting from tidal influences (Figure 4). However, the mean temperature was relatively consistent over the five-month period following deployment, allowing the records for each hole to be averaged and treated as a single measurement for purposes of modeling (Figure 3). In each case, we extrapolated the average of the measured borehole temperatures up to the sediment-basement interface based on the local heat flow and inferred properties in basement [*Davis et al.*, 1997a, 1992; *Fisher et al.*, 2005]. CORK thermal data from Hole U1301A were interpreted in studies of borehole chemistry and microbiology [*Orcutt et al.*, 2010; *Wheat et al.*, 2010], but have not been interpreted previously in terms of crustal hydrogeologic properties. Short-term packer experiments and the cross-hole response at nearby Hole 1027C have also provided information on hydrogeologic properties in the vicinity of these boreholes [e.g., *Becker and Fisher*, 2008; *Fisher et al.*, 2008].

2. Analytic Methods

2.1. Borehole Models

[16] We link three analytic solutions describing the physical response to flow in a borehole (diffusive thermal exchange, hydrostatic pressure within the borehole, and radial flow to/from the formation) to relate thermal profiles to physical and hydrologic properties of interest (formation permeability, porosity, sediment thermal conductivity, regional heat flow, aquifer thickness, aquifer compressibility, borehole radius in basement, flow rate, and flow duration (Table 2)).

[17] Thermal profiles are modeled using an analytic solution to a thermal diffusion equation for a cylindrical flowing well with constant throughflow [*Lesem et al.*, 1957], as a function of duration of flow (t) and depth into hole (z) (modified from *Becker et al.* [1983], variables defined in Notation section),

$$T(t,z) = Gz - \left[\frac{GQ(\rho c)_w}{\pi^2 r_s^2 \kappa_s}\right]\left[\frac{8\kappa_s^2}{\pi(\rho c)_w^2 \chi_s^2} I_1(t) - \frac{2\kappa_s}{(\rho c)_w \chi_s} I_2(t,z)\right] \tag{1}$$

where G is the geothermal gradient, Q is the volumetric flow rate, r_s is the borehole radius, $(\rho c)_w$ is the specific heat capacity of water, and κ_s and χ_s are the thermal conductivity and thermal diffusivity of sediment, respectively. Fluid properties are calculated through an empirically derived equation of state as a function of temperature and salinity [*Sharqawy et al.*, 2010]. Salinity is held at a constant bottom water value (35 g/kg) throughout the analysis. I_1 and I_2 are integrals that are solved numerically with adaptive Gauss-Kronrod quadrature [*Shampine*, 2008], which is computationally inexpensive but must be repeated many times for each hole. The solution is derived iteratively by solving equation (1) and updating borehole temperatures and associated fluid properties after each iteration.

[18] The modeled thermal profile is used to calculate fluid density with depth, $\rho(z)$, including dependence on temperature but neglecting the influence of changes in pressure or salinity. Fluid density profiles are calculated for thermal conditions in the borehole (equation (1)) and for

Table 2. MCMC Analysis Parameters, Prior Distributions, and Sources

				Reference/Value			
Parameter	Symbol	Units	Distribution	504B	1026B	1301A	1301B
Thermal conductivity (sediment)	κ_s	W/(m°C)	Gamma	a	b	c	c
Mean				1.10	1.40	1.30	1.30
Std. dev.				0.15	0.25	0.10	0.10
Basement porosity	ϕ		Gamma	d, e	f	f	f
Mean				0.10	0.10	0.10	0.10
Std. dev.				0.05	0.05	0.05	0.05
Aquifer compressibility	β	10^{-10} Pa^{-1}	Gamma	g	g	g	g
Min				5	5	5	5
Mean				8	8	8	8
Std. dev.				2	2	2	2
Heat flow (seafloor)	q	W/m^2	Gamma	h	b	c	c
Mean				0.20	0.345	0.280	0.280
Std. dev.				0.10	0.020	0.030	0.030
Aquifer thickness	H	M	Gamma	i	j	c	c
Min.				15	10	15	15
Mean				40	18	50	165
Std. dev.				10	8	25	10
Borehole radius (basement)	r_b	m	Exponential	i	j	c	c
Min.				0.127	0.127	0.187	0.160
Mean				0.197	0.197	0.287	0.260
Flow duration	t	days	Uniform	h	k	c	c
Min.				39	0	139	117
Max.				57	16	155	146
Basement temperature	T_b	°C	Gamma		k		
Mean					63.78		
Std. dev.					0.05		
log$_{10}$(permeability)	k	m^2	Uniform				
Min.				−15	−15	−15	−15
Max.				−8	−8	−8	−8

[a][*Wilkens et al.*, 1983]. Sediment samples, downhole logs.
[b][*Pribnow et al.*, 2000]. Sediment samples, downhole logs.
[c][*Expedition 301 Scientists*, 2005b]. Drilling records, sediment samples, downhole logs.
[d][*Becker et al.*, 1982]. Downhole electrical resistivity logs.
[e][*Newmark et al.*, 1985]. Downhole sonic logs.
[f][*Bartetzko and Fisher*, 2008]. Basement samples, downhole logs.
[g][*Fisher et al.*, 2008]. Cross-hole aquifer test.
[h][*Becker et al.*, 1983]. Drilling records, downhole logs.
[i]*Cann and Von Herzen*, 1983]. Drilling records, downhole logs.
[j][*Expedition 301 Scientists*, 2005a]. Drilling records, sediment samples, downhole logs.
[k][*Fisher et al.*, 1997]. Thermal measurements taken in basement, drilling records.

ambient formation fluid based on a constant geothermal gradient inferred from local measurements. We assume flow in the borehole is slow enough for pressure conditions to be essentially hydrostatic, and integrate downward from the seafloor to calculate pressures in the borehole and ambient formation (P_b and P_a, respectively):

$$P_b(z) = g\int_0^z \rho_b(z)\mathrm{d}z \qquad (2a)$$

$$P_a(z) = g\int_0^z \rho_a(z)\mathrm{d}z \qquad (2b)$$

where g is the acceleration due to gravity, and ρ_b(z) and ρ_a(z) are the borehole and ambient fluid density profiles, respectively. The integral is approximated as a finite difference problem, summing pressures piecewise over 5 m intervals.

[19] The difference between borehole and ambient pressures ($\Delta P = P_b - P_a$) is used to solve the pressure diffusion equations for volumetric flow rate into or out of basement (modified from *Becker et al.* [1983] and *Fisher et al.* [1997]; after *Jaeger* [1942, 1965] and *Matthews and Russell* [1967]):

$$Q = \frac{8kH\Delta P}{\pi\mu_w} I_3(\tau), \quad \tau = \frac{kt}{\phi\mu_w\beta r_b^2} \qquad (3)$$

[20] In equation (3), k is the formation permeability, H is the thickness of the permeable zone, r_b is the borehole radius in basement, μ_w is the dynamic viscosity of water, ϕ is the porosity, and τ is dimensionless time. The term β is the compressibility of the crustal aquifer system, comprising the sum of

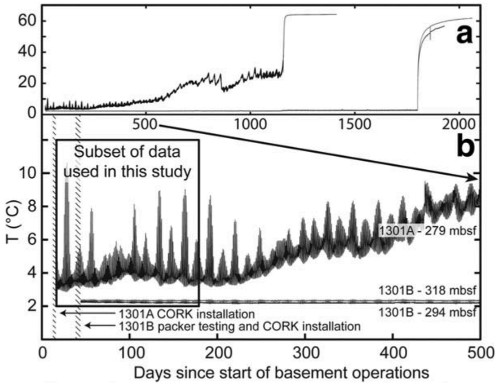

Figure 4. (a) Temperature records from autonomous temperature loggers deployed in Holes U1301A and U1301B [*Fisher et al.*, 2005]. (b) Detail plot of same data shown in Figure 4a, showing the first 500 days of the record and highlighting the 150 days of values averaged for use in the present study (box). There is much more tidal variability in borehole temperatures in Hole U1301A than in Hole U1301B, consistent with the greater flow rate down Hole U1301B inferred in the present study.

fluid and formation compressibility. We expect formation compressibility in rubbly and fractured upper oceanic crust to be considerably greater than fluid compressibility (4–5 × 10^{-10} Pa^{-1} [*Fine and Millero*, 1973]), and thus interpret β to represent primarily formation compressibility. The integral I_3 is tabulated in *Jaeger and Clarke* [1942], and can also be approximated and evaluated numerically [*Becker et al.*, 1983]. This equation yields the volumetric flow rate (Q) from the borehole into the permeable basement zone ($Q > 0$, downflow case) or out of the permeable basement zone into the borehole ($Q < 0$, upflow case).

[21] Flow into or out of the formation (Q) determined by equation (3) should equal the flow along the borehole used in equation (1). The result from equation (3) is therefore used as the flow rate for equation (1), and calculations are repeated iteratively until the two rates converge to ensure a self-consistent solution. Iteration in this case is very stable, and flow rates typically converge to within 1% in fewer than five iterations.

2.2. Markov Chain Monte Carlo Analysis

[22] The forward model described in the last section utilizes analytic equations representing coupled fluid and heat flow to generate borehole thermal profiles based on a set of known or assumed physical parameters. We wish to characterize these parameters based on downhole thermal measurements and other observations, essentially solving an inverse problem. We do this with a Markov chain Monte Carlo (MCMC) analysis [*Chib and Greenberg*, 1995; *Gallagher et al.*, 2009], which treats each of the model parameters as a statistical distribution of values, rather than a single value. This approach yields probabilistic distributions of model parameters as output.

[23] For MCMC analysis, a statistical distribution known as a "prior distribution" must be provided for each parameter, codifying knowledge that is not explicitly treated by the forward model. For example, the radius of the borehole wall within the open formation is often poorly known because the upper ocean crust is rubbly and unstable, frequently leading to borehole collapse, as indicated by caliper measurements showing borehole enlargement and geophysical logs (bulk density, porosity) that are of poor quality [e.g., *Anderson et al.*, 1985; *Bartetzko and Fisher*, 2008; *Moos*, 1990]. In general, it is likely that the smallest possible borehole radius is that of the drill bit, but the actual diameter is likely to be greater and may be variable with depth. MCMC analysis is not used to determine the borehole radius per se, but provides information on how the assumed borehole radius influences estimates of other parameters of interest (e.g., formation permeability, volumetric flow rate, duration of flow). In practice, several of the key physical parameters embedded in equations (1) and (3) are poorly known, although in many cases, these values can be bounded and/or expected to fall within particular distributions. The MCMC approach uses a random process to condition each prior distribution to both the data provided and the other parameters' prior distributions. This results in a series of random samples drawn from a final statistical distribution, known as a "posterior distribution," for each parameter (Figure 5). These are sets of values for each parameter that allow the borehole thermal observations to be fit within a range of error based on the uncertainty in the data and prior distributions. The posterior distributions are interpreted as estimates of the value of each parameter as conditioned by the full suite of available information [*Tierney*, 1994]. Because the MCMC approach allows all of the parameters of interest to vary simultaneously, this approach improves upon a more traditional "sensitivity analysis" based on varying one parameter at a time, which tends to underestimate their individual uncertainties.

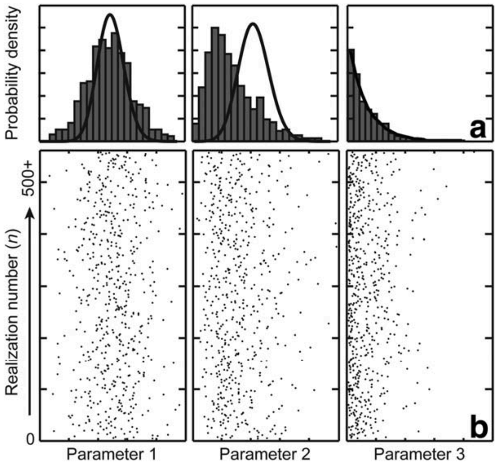

Figure 5. (a) Cartoons showing histograms of the posterior distributions for three parameters, with lines representing the initial prior distributions for each. Histograms comprise parameter values selected from MCMC models that allow a reasonable fit to an observational constraint. (b) Trace plots of random samples from posterior distributions generated by the MCMC analysis as a function of realization number. Analyses are run for hundreds or thousands of realizations, until the posterior distributions stabilize.

[24] Our MCMC analysis uses a random-walk chain, created with a Metropolis-Hastings algorithm [*Chib and Greenberg*, 1995] to draw samples from posterior distributions. To generate each MCMC realization, values to be used in a single run of the forward analytic model are proposed for each parameter, starting with arbitrary choices and with subsequent steps using proposals drawn randomly from the vicinity of values used in the previous step. The resultant thermal profile from the forward model is compared to observational data (borehole thermal records) to calculate a data likelihood function [$f\ (\boldsymbol{T}|\theta)$], which is a measure of how closely the observed and modeled profiles agree (Figure 6). In this study, we assume independent and identically distributed normal errors in the thermal data, which simplifies the joint data likelihood function for all m thermal measurements to

$$f(\boldsymbol{T}|\theta) = \prod_{i-1}^{m} \frac{1}{\sigma\sqrt{2\pi}} \exp\left[-\frac{1}{2}\left(\frac{T_{i,\mathrm{model}} - T_{i,obs}}{\sigma}\right)^2\right] \tag{4}$$

[25] This function is used to determine the acceptance probability (α_θ) for each proposed parameter value (θ^*) derived from each MCMC realization (n):

$$\alpha_{\theta,n} = \min\left[1, \frac{f(\boldsymbol{T}|\boldsymbol{\theta}^*)f(\theta^*)/p(\theta^*|\theta_n)}{f(\boldsymbol{T}|\boldsymbol{\theta}_n)f(\theta_n)/p(\theta_n|\theta^*)}\right] \tag{5}$$

[26] If a parameter value is accepted, $\theta_{n+1} = \theta^*$; otherwise, it is rejected and $\theta_{n+1} = \theta_n$. Once this is done for each model parameter, new random values are proposed, and the process is repeated until sufficient samples have been generated to create a set of relatively smooth posterior distributions. The first sequence of steps is often strongly influenced by the initial arbitrary selection of the chain's starting point, and is therefore discarded. The remaining random-walk steps are downsampled to ensure independence and interpreted as samples from the posterior distribution functions for each parameter [*Tierney*, 1994]. The MCMC analyses in this study were run to generate >500 independent samples of posterior probability distributions for all parameters in each hole, after which mean values for all distributions converged to within 1%. In several cases, this required running >100,000 realizations. The code to perform the complete analysis, and example input and output files, are available at http://pmc.ucsc.edu/~afisher/Research/Appen/BHT-MCMC.

2.3. Inferred Property Distributions

[27] We provided prior distributions for eight parameters for each downflow case (Holes 504B,

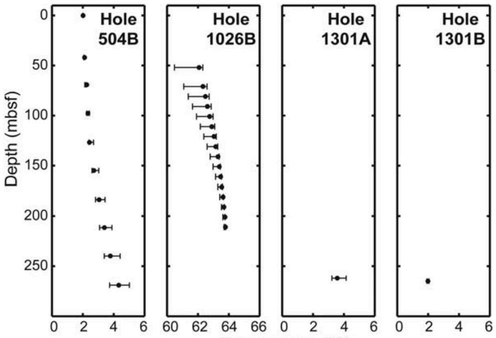

Figure 6. Thermal profiles generated by the MCMC analyses. Observational data are shown as solid circles, whereas the bars indicate the central 90% of temperature ensembles for each measurement depth. The MCMC analyses allowed acceptance of some parameter sets that deviate significantly from observed temperature values, although their probability is low. Including these relatively extreme deviations in predicted temperatures in the ensemble of accepted parameter sets provides a conservative range of posterior distributions for physical parameters.

U1301A, U1301B) and nine for the upflow case (Hole 1026B), as the upflow case requires basement temperature as an additional parameter (Table 2). The prior distributions for each parameter required careful selection, as the number of free parameters used in the full analysis is large relative to the number of observations used to constrain acceptable results (mainly temperature measurements). Most prior distributions assigned in this study are gamma distributions, which converge to normal distributions when the specified mean is much larger than the variance, as was the case for most parameters treated. The gamma distribution was chosen over the normal distribution because it converges to zero probability at its lower bound. This behavior is consistent with most parameters used in this study, which often have no meaning below some physical limitation (e.g., bit size for borehole radius). For both permeability and flow duration, where earlier studies or data were often ambiguous, bounded uniform prior distributions were used. We emphasize discussion of borehole flow rate and formation properties in this paper, but MCMC analyses were used to generate posterior distributions for all parameters, all of which are shown as figures in the supporting information.[1]

[28] Volumetric flow rate (*Q*) is solved for directly through iteration of the analytic forward model and is thus not treated explicitly as a parameter by the MCMC analysis. Without an explicitly defined prior distribution to condition to thermal data, a posterior distribution for *Q* must instead be determined after the MCMC analysis is completed. To do this, the forward model is rerun once for each realization, using values from the previously generated posterior distribution for each parameter. The resultant volumetric flow rates form a posterior distribution that is consistent with the ensemble of MCMC results.

2.4. Model Assumptions and Limitations

[29] Equations (1)–(3) are analytic solutions based on several assumptions and approximations. First, although the solution to the thermal response is transient, fluid flow up or down a borehole is assumed to occur at a constant rate and direction. Thus this analysis does not strictly apply to records with more complex flow histories (periods of active pumping; changing flow rates; flow reversals) [*Lesem et al.*, 1957]. The analysis assumes laminar flow, although solutions presented later have Reynolds numbers indicating transitional or mildly turbulent flow, the most significant effect of which is likely an overestimation of driving pressures from neglecting turbulent energy losses. This effect should be small in Holes 504B and 1026B, but could be more significant in Holes U1301A and U1301B where fluid flowed through small gaps in the casing hanger. Further, equations (1) and (3) use constants for some physical properties that vary over spatial scales relevant to the problem or are otherwise difficult to constrain. Examples include the geothermal gradient and sediment thermal conductivity, both of which are treated as constants by the model but are known to vary somewhat with depth. These uncertainties and idealizations are addressed, to a large extent, by the MCMC analysis, and we have taken a conservative approach in allowing acceptance of proposed parameters even when differences between modeled and observed thermal logs are relatively large.

3. Results

3.1. Summary of Model Results and Parameter Distributions

[30] Results from the linked models of formation properties and borehole flow and temperature, developed with MCMC analyses, are summarized in Figures 6–8, Table 3, and Figures S1 to S4 (supporting information). Figure 6 shows profiles of temperature versus depth, comparing model results to observations. The range of model results shown is wide relative to the accuracy of individual temperature measurements, because the MCMC method permits the acceptance (with low probability) of parameter sets that deviate significantly from observations. Rather than truncating these posterior distributions, we show 90% of the range of resulting temperature ensembles as a conservative indication of model confidence. Table 3 lists posterior median borehole flow rates (*Q*) and formation bulk permeability values (*k*) with their standard deviations (in log cycles), and compares these values to those published previously. Figures in the supporting information comprise comprehensive plots of all posterior parameter distributions. Results are described site by site in the rest of this section, after which we discuss their implications.

3.2. Hole 504B

[31] MCMC analysis using the linked analytic models generated a good fit to borehole thermal

---

[1] Additional supporting information may be found in the online version of this article.

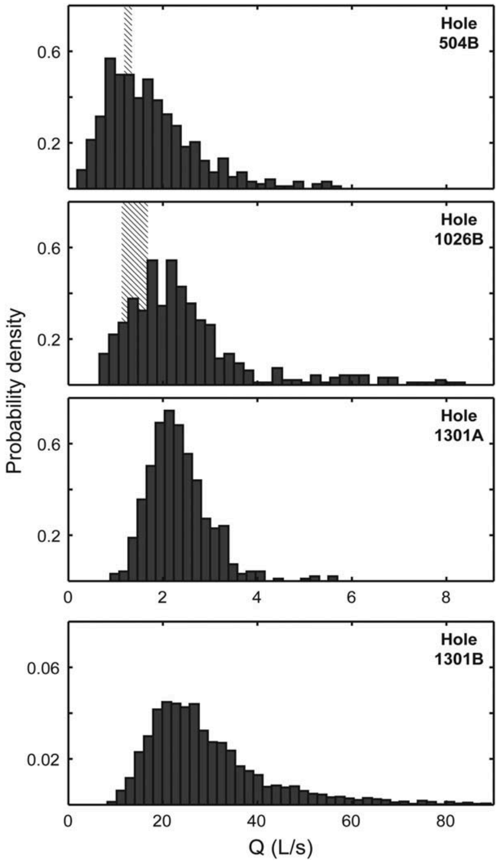

Figure 7. Posterior probability distribution functions for volumetric flow rate (Q) in each hole. Vertical bands depict values from previous thermal studies [*Becker et al.*, 1983; *Fisher et al.*, 1997]. Summary statistics for each distribution are presented in Table 3. Note that range of posterior flow values shown is similar for Holes 504B, 1026B, and 1301A, but a larger range (and higher median value) resulted for Hole 1301B.

data (Figure 6a). The shallowest temperatures are effectively "pinned" by the temperature of bottom water at the seafloor, whereas borehole temperatures at the base of the cased interval are more sensitive to the downhole flow rate. The posterior distribution of volumetric flow rates (Q) down Hole 504B was strongly asymmetric, having relatively high probability at lower values ($\geq$0.2 L/s), and a long declining tail of higher values ($\leq$60 L/s) (Figure 7a). The distribution has a median of $Q = 1.6$ L/s (Table 3), with 90% of the total probability between 0.5 and 3.5 L/s.

[32] Results for the posterior permeability distribution (k) were roughly log-normally distributed (Figure 8a). The median k value was 4.7×10^{-12} m^2 (Table 3), with 90% of the probability between 1.7×10^{-12} m^2 and 1.4×10^{-11} m^2. The posterior distribution for flow duration showed little sensitivity across the allowed range (39–57 days) (Figure S1G; supporting information). The remaining parameters had posterior distributions with shapes that were similar to those of their prior distributions (Figure S1; v), with deviations of only 1–5% from the prior probability density for each parameter. That many of the posterior distributions closely resemble the specified prior distributions suggests that the parameter ranges chosen allow

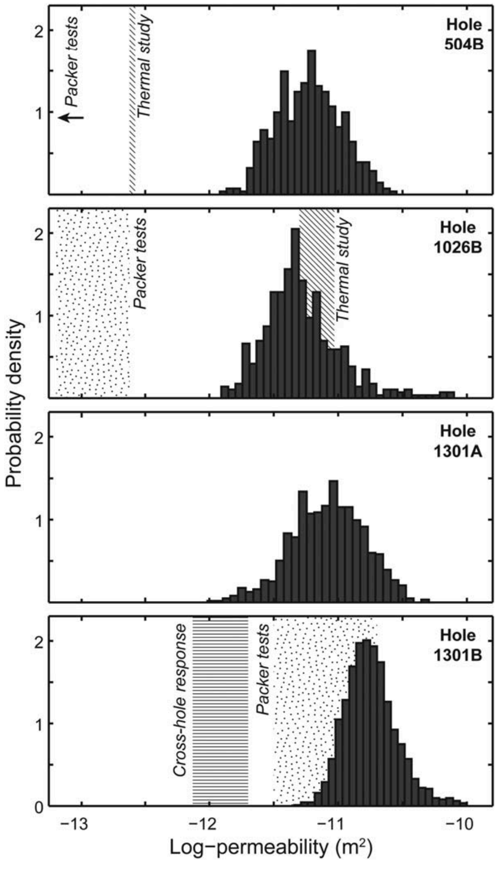

Figure 8. Posterior probability distribution functions for permeability (k) at each hole. Vertical bands depict values from previous studies. Packer results were determined through single-hole experiments [*Anderson and Zoback*, 1982; *Becker and Fisher*, 2000, 2008], whereas cross-hole response of downflow into Hole U1301B was measured 2.4 km away at Hole 1027C [*Fisher et al.*, 2008]. Previous thermal study results [*Becker et al.*, 1983; *Fisher et al.*, 1997] were derived without linked models or MCMC analyses. Summary statistics for each distribution are presented in Table 3.

Table 3. Median MCMC Analysis Flow Velocity and Permeability Results, With Comparison to Results of Previous Studies

Hole	Q [a] (L/s)	σ_Q [b]	k [a] (m^2)	σ_k [b]	Q [c] (L/s) (Previous Study)	k (m^2)(Previous Study)
504B	1.6	0.25	4.7×10^{-12}	0.27	1.3[d]	2×10^{-13}[d], 4×10^{-14}[e]
1026B	2.3	0.28	3.7×10^{-12}	0.32	1.4[f]	7×10^{-12}[f], 1×10^{-13}[g]
1301A	2.3	0.15	6.6×10^{-12}	0.23		
1301B	27	0.24	1.5×10^{-11}	0.26		2×10^{-11}[h], 2×10^{-12}[i]

[a] Median values for each posterior distribution from MCMC analyses.

[b] Standard deviation in log cycles for each posterior distribution.

[c] Converted from linear flow rate (v) to volumetric flow rate (Q) by $Q = v \pi r_s^2$, where r_s is the cased borehole radius within the sediment section.

[d] [*Becker et al.*, 1983]. Estimate assumed higher pressures than used in this study.

[e] [*Anderson and Zoback*, 1982]. Packer test performed in Hole 504B.

[f] [Fisher et al., 1997].

[g] [*Becker and Fisher*, 2000]. Packer test performed in Hole 1026B.

[h] [*Becker and Fisher*, 2008]. Packer test performed in Hole U1301B, 36m from Hole U1301A.

[i] [*Fisher et al.*, 2008]. Cross-hole response between Hole U1301B and Hole 1027C, 2.4 km east.

reasonable fits to the thermal observations, though this does not strictly comprise a test of distribution accuracy.

3.3. Hole 1026B

[33] The fit of MCMC results to borehole thermal data from Hole 1026B, an upflow case, is inverted relative to that from 504B, with less sensitivity to flow rate closer to the zone of discharge from basement (Figure 6b). Posterior distributions for both Q and k in Hole 1026B were also asymmetrically distributed, with probability density skewed toward lower values (Figures 7b and 8b). The median of the distribution for Q was 2.3 L/s (90% between 0.9 and 7.2 L/s), and the median of k was 3.7×10^{-12} m^2 (90% between 1.4×10^{-12} m^2 and 1.6×10^{-11} m^2) (Table 3).

[34] The posterior distribution for the duration of flow at Hole 1026B shows a consistent deviation from its uniform prior distribution (Figure S2G; supporting information). Most of the allowed range of flow duration appears flat, but the probability density shows a marked drop during the time period of 0–3 days, indicating that the borehole thermal data were poorly modeled by short-duration flows. As an upflow case, the model for Hole 1026B required the specification of a distribution of basement temperatures. The posterior distribution for basement temperature has a higher mean and lower variance than did the prior distribution (Figure S2H; supporting information). The warmer basement temperatures generate modeled thermal profiles that better match the data, illustrating how posterior distributions can differ significantly from their prior distributions when the data require it. The posterior distributions of remaining parameters are similar to those selected for prior distributions (Figure S2; supporting information).

3.4. Holes U1301A and U1301B

[35] Observational data from Holes U1301A and U1301B, which suggest downward flow of fluid from the seafloor during the first 5 months post drilling, provide less constraint on borehole and formation properties than data from Holes 504B and 1026B, because the analysis is based on temperatures from a single depth in each hole (Figures 6c and 6d).

[36] The distributions of downward flow rates in Holes U1301A and U1301B are asymmetric, skewed toward lower values than true log-normal distributions (Figures 7c and 7d). The median value for Q at Hole U1301A was 2.3 L/s (90% probability between 1.4 and 4.4 L/s), whereas the median value for Q at Hole U1301B was an order of magnitude greater, 27 L/s (90% probability between 15 and 67 L/s). Posterior distributions for k in both holes are close to log-normally distributed (Figures 8c and 8d), with a median of 6.6×10^{-12} m^2 in Hole U1301A (90% probability between 3.0×10^{-12} m^2 and 1.7×10^{-11} m^2), and a median of 1.5×10^{-11} m^2 in Hole U1301B (90% probability between 7.5 $\times 10^{-12}$ m^2 and 4.1×10^{-11} m^2.) (Figures 8c and 8d). The posterior distributions of the remaining parameters are similar to prior distributions for both holes (Figures S3 and S4; supporting information).

4. Discussion

4.1. Hole 504B

[37] Our median results for volumetric flow rate (Q) at Hole 504B are approximately 20% higher than the previously published estimate [*Becker et al.*, 1983], but the difference is within the estimated uncertainty generated from the MCMC analysis (Table 3 and Figure 7). The forward model used in

the earlier study was essentially the same as that applied in this paper, but without an assessment of uncertainties in the sedimentary thermal gradient, thermal properties, or the duration of flow, and no iterative analysis to assure a consistent result between the three analytic models.

[38] The difference in inferred bulk permeability of upper basement is considerably greater, with the median value from new analyses being 20 times larger than calculated previously based on the same thermal data (Table 3 and Figure 8). Most of this difference can be attributed to the use of a higher apparent formation underpressure, inferred from packer testing [*Anderson and Zoback*, 1982; *Becker et al.*, 1983], in lieu of the borehole hydrostatic condition used in this study (equation (2)). At the time of initial packer tests in Hole 504B, there had been no direct measurements of natural pressures in upper basement rocks on ridge flanks through use of sealed borehole observatories, and a differential pressure of ~1 MPa was not considered to be unreasonable. Since that time, natural differential pressures on the order of a few tens of kilopascals have been measured in upper basement using borehole observatories at several ridge-flank locations, including the eastern flank of the Juan de Fuca Ridge [e.g., *Davis and Becker*, 2002] and Hole 504B [*Becker et al.*, 2004]. Similarly small differential pressures have also been inferred from transient numerical models of coupled fluid and heat flow on ridge flanks [e.g., *Hutnak et al.*, 2006; *Spinelli and Fisher*, 2004; *Stein and Fisher*, 2003].

[39] Basement permeability inferred in the present study is more than 100 times greater than that inferred from packer testing of upper basement [*Anderson et al.*, 1982], but this ratio is reduced to 30 after accounting for the difference in assumed basement aquifer thickness (172 m versus 40 m). This apparent difference in permeability with test type is consistent with the scaling of permeability in heterogeneous rocks, such as the upper oceanic crust, with higher values typically resulting from tests run at greater length scales [*Becker and Davis*, 2003; *Clauser*, 1992; *Fisher*, 1998]. Short-term, single-hole packer tests tend to produce results representative of a radial distance of a few meters, whereas flow tests lasting weeks to months are representative of a kilometer scale.

4.2. Hole 1026B

[40] The median volumetric flow rate up Hole 1026B determined in the present study was ~60% greater than that estimated previously from the same thermal data (Table 3 and Figure 7), whereas median bulk permeability in upper basement was lower by 50% (Table 3 and Figure 8) [*Fisher et al.*, 1997]. In both cases, previous estimates fall within the range indicated by 90% of the MCMC results. The differences in median flow rate and bulk permeability resulted from the iterative approach and MCMC analysis used in the present study.

[41] The bulk permeability estimated in the present study is 20–40 times greater than that calculated from packer testing in the same hole [*Becker and Fisher*, 2000], similar to the ratio between values derived from thermal data and packer testing in Hole 504B. Pumping rates used during packer testing were similar to flow rates inferred during free flow discharge from Hole 1026B, so there should have been a comparable influence of turbulent energy losses. As with Hole 504B, the difference in permeability estimated by the two methods is likely the result of scale effects.

[42] The drop in the probability density in the posterior distribution for flow duration appears to be significant, indicating that short flow durations (0–3 days) are less likely to produce the observed thermal profile. These results suggest that it is more likely that the upward flow in Hole 1026B began relatively early during borehole operations, rather than in the few days immediately before the thermal log was run.

4.3. Holes U1301A and U1301B

4.3.1. Comparison With Results of Earlier Studies

[43] Thermal data from Holes U1301A and U1301B have not been interpreted previously, but we compare new results to basement permeability calculations from packer testing [*Becker and Fisher*, 2008] and from the cross-hole response to downflow in Hole U1301B detected in Hole 1027C, 2.4 km to the east [*Fisher et al.*, 2008]. Packer tests were attempted in both Holes U1301A and U1301B on IODP Expedition 301, but were unsuccessful in Hole U1301A due to the lack of a casing seal or cement between casing and the formation. Results from packer testing in Hole U1301B indicated bulk permeability of 3×10^{-12} m^2 for a crustal interval 166 m thick (the lower half of the basement hole), and 2×10^{-11} m^2 for a 30 m thick interval between two packer-setting depths. This permeability range overlaps with the distribution of bulk permeability values inferred in the present study (Table 3 and Figure 8), but may

not be directly comparable, because each analysis sampled different depth intervals within the upper crust. Packer testing focused on the interval 152–318 msb, whereas we have interpreted long-term downhole flow to enter the crust around Hole U1301B above the shallowest casing packer installed with the borehole observatory, located at 166 msb.

[44] The cross-hole response seen in Hole 1027C, resulting from 13 months of downward flow into Hole U1301B, suggested bulk permeability in the same shallow crustal interval that is an order of magnitude lower than inferred in the present study, 7×10^{-13} m^2 to 2×10^{-12} m^2 (Figure 8) [*Fisher et al.*, 2008]. The use of a second borehole and the long duration of the cross-hole response would tend to sample a larger volume than a single-hole flow test based on thermal data. The larger-scale cross-hole test could have yielded a lower bulk permeability because of azimuthal anisotropy in permeability, with the orientation having the highest permeability being oblique to the direction between Holes U1301B and 1027C. This is consistent with the preferred fluid flow direction suggested by studies in the same region [e.g., *Fisher et al.*, 2008; *Hutnak et al.*, 2006; *Wheat et al.*, 2000], and would not be resolved by a single-hole analysis using thermal records.

4.3.2. Comparison of Results in Holes U1301A and U1301B

[45] The calculated rate of downward flow into Hole U1301B is an order of magnitude greater than that down Hole U1301A (Table 3 and Figure 7). This is consistent with the nature of the tidal response in the two holes (Figure 4), which is much greater in Hole U1301A, the lower borehole temperatures in Hole U1301B, and the subsequent reversal of flow direction in Hole 1301A [*Wheat et al.*, 2010]. The more rapid flow rate in Hole U1301B is likely the result of the difference in the total depth of these holes (370 mbsf in Hole U1301A, 582 mbsf in Hole U1301B). The depth of Hole U1301B provides greater thermal perturbation and a taller cold hydrostatic column, resulting in commensurately higher differential pressure, driving fluid into the formation surrounding the borehole at a greater rate.

[46] The median bulk permeability calculated from the temperature data in Hole U1301B is twice that calculated from similar data in Hole U1301A (Table 3), suggesting that the deeper crustal section around Hole U1301B is more permeable than the shallower section around Hole U1301A. This interpretation is consistent with the nature of the cross-hole pressure response in Hole 1027C [*Fisher et al.*, 2008]: drilling, casing, and other operations in Hole U1301A had little influence on crustal pressure conditions monitored in Hole 1027C, whereas similar operations in Hole U1301B caused rapid, measurable pressure responses in Hole 1027C. A difference in permeability between the holes could result from lateral or vertical variability in crustal properties. However, given the overlap in the distributions of permeability values determined by MCMC analyses (Figure 8) the apparent difference in permeability between Holes U1301A and U1301B may not be statistically significant.

4.4. Comparison of Results From All Boreholes

[47] Median bulk permeability values for the four boreholes evaluated in this study vary by a factor of 4 (3.7×10^{-12} to 1.5×10^{-11} m^2), despite differences in setting, seafloor age, and hole completion parameters. Given the wide range of ocean crustal permeability values seen globally [e.g., *Fisher et al.*, 2008] and the extent of local variability in crustal properties commonly found in individual holes [e.g., *Bartetzko and Fisher*, 2008; *Broglia and Moos*, 1988; *Jarrard et al.*, 2003], the observed consistency in hydrogeologic properties is surprising. Determining whether the consistency of permeability in these four boreholes is coincidence, or indicative of properties more broadly, will require the application of similar methods to additional boreholes.

[48] The median flow rates inferred down Holes 504B and U1301A and up Hole 1026B were also similar, but median flow rate down Hole U1301B is an order of magnitude greater (Table 3 and Figure 7). The greater flow rate down Hole U1301B relative to Hole U1301A helps to explain why Hole U1301A reversed after ~3 years of continuous downflow [e.g., *Wheat et al.*, 2010], whereas flow down Hole U1301B ended only when the reentry cone surrounding the wellhead was cemented [*Fisher*, 2010]. Hole 1026B, which had even less penetration into basement than Hole U1301A, reversed flow (down to up) within 14 days after the end of drilling and casing operations [*Fisher et al.*, 1997] (Figure A-2G). Flow down Hole 504B slowed gradually to very low values over 22 years [*Becker et al.*, 2004], aside from the enigmatic but brief renewal of downflow at 12 years suggested by the temperature log of *Gable et*

al. [1995]. In contrast, in Hole 896A, located <1 km to the south of Hole 504B, initial downflow reversed quickly following drilling operations [*Becker et al.*, 2004]. In addition to depending on total borehole depth and depth into basement, the occurrence and timing of a reversal in flow direction in ocean crustal holes that initially experience down flow may depend on basement topographic patterns beneath ridge-flank sediments [*Bani-Hassan et al.*, 2012; *Fisher et al.*, 1990; *Hartline and Lister*, 1981; *Wang et al.*, 1997]. Holes 896A, 1026B, and U1301A/B were all drilled into sediment-covered basement highs, which tend to be naturally overpressured relative to ambient hydrostatic conditions, whereas Holes 504B and 1027C were associated with sediment-covered basement lows, which tend to be underpressured [*Davis and Becker*, 2002, 2004].

5. Summary and Conclusions

[49] We have presented a model of the thermal state of flowing seafloor boreholes that links analytic solutions to three distinct physical processes (diffusive thermal exchange, development of hydrostatic pressure within the borehole, and radial flow to/from the formation at depth). The model is run as part of a MCMC analysis to assess uncertainty in flow properties (rate, duration) and in borehole and formation physical properties (basement permeability, borehole radius, aquifer thickness, etc.). Results were presented for two thermal records that have been interpreted previously (Holes 504B and 1026B) and for two records recently recovered from long-term borehole observatories (Holes U1301A and U1301B). All of these holes were drilled into relatively young, upper oceanic crust below thick overlying sediments.

[50] New models suggest that the bulk permeability of upper oceanic crust around Holes 504B, 1026B, and U1301A is 4–7 × 10^{-12} m^2. Calculated median permeability around the upper part of Hole 504B is 20 times greater than estimated previously [*Becker et al.*, 1983], mainly because an improved estimate of the differential pressure that drives flow into the formation, and ~50% less than estimated previously for upper crust around Hole 1026B [*Fisher et al.*, 1997]. The median permeability of the upper ocean crust around Hole U1301B is ~1.5 × 10^{-11} m^2, somewhat greater than that calculated for Hole U1301A located just 36 m away. Apparent differences in bulk permeability of the ocean crust around these boreholes are relatively small when compared to the wide range of values measured globally, and the MCMC analyses generated overlapping distributions of properties for these boreholes. Given the uncertainties in borehole and formation parameters revealed through the MCMC analyses, results from the present study suggest relatively consistent bulk permeability values for the uppermost volcanic ocean crust.

[51] Permeability estimates in Holes 504B and 1026B based on thermal logs are 20–40 times greater than those from packer testing, which may result from the larger scale of measurement associated with longer-term thermal studies. Results from packer testing in Hole U1301B yielded permeability estimates consistent with those from this study [*Becker and Fisher*, 2000], but packer and thermal analyses from Hole U1301B tested different crustal depths, and so may not be directly comparable. Bulk permeability calculated from analysis of the thermal record from Hole U1301B is 10 times greater than that determined from the observed cross-hole response between Holes U1301B and 1027C, which could result from azimuthal anisotropy in permeability [*Fisher et al.*, 2008].

Notation

$f(\boldsymbol{T}\|\boldsymbol{\theta})$	data likelihood of forward model.
$f(\theta)$	prior likelihood.
g	gravitational acceleration, m/s^2.
G	geothermal gradient, °C/m.
H	thickness of permeable zone, m.
$I_1(t)$, $I_2(t,z)$	integrals required for solution to thermal diffusion equation, based on cylindrical borehole geometry, detailed in [*Becker et al.*, 1983].
$I_3(\tau)$	integral required for solution to pressure diffusion equation, tabulated in [*Jaeger and Clarke*, 1942].
k	permeability of basement rocks, m^2.
m	number of thermal measurements.
n	MCMC realization number.
$p(\theta^*/\theta_n)$	probability of proposing θ^*, given the previously accepted value θ_n.
P_a	pressure in ambient formation, Pa.
P_b	pressure in the borehole fluid column, Pa.
Q	volumetric flow rate up or down borehole, m^3/s.
r_b	borehole radius in basement, m.
r_s	borehole radius in sediments, m.

T_{obs}	observed borehole temperature, °C.
T_{model}	modeled borehole temperature, °C.
z	depth below seafloor, m.
α	acceptance probability for proposed parameter in MCMC realization.
β	fluid compressibility, $\mathrm{Pa}^{-1.}$
θ	generic MCMC parameter.
κ_s	thermal conductivity of sediment, W/(m°C).
μ_w	dynamic viscosity of water, Pa·s.
$(\rho c)_w$	specific heat capacity of water, J/(kg°C).
σ	estimated uncertainty in thermal data, °C.
τ	dimensionless time, used as argument of I_3.
ϕ	porosity.
χ_s	thermal diffusivity of sediments, m^2/s.

Acknowledgments

[52] This research was based on data and samples provided by the Integrated Ocean Drilling Program, the Ocean Drilling Program, and the Deep Sea Drilling Project. We thank the crews, technicians, and officers of the drilling ships and of numerous oceanographic and deep submergence platforms whose skill and hard work made these studies possible. This research was supported by Consortium for Ocean Leadership (COL) projects T327A7 and T327B7 (A.T.F.) and project T327B8 (K.B.), and NSF grants OCE-0939564 and 1031808 (A.T.F.) and OCE-1030350 (K.B.). This is C-DEBI contribution 173.

References

Alt, J. C., J. Honnorez, C. Laverne, and R. Emmermann (1986), Hydrothermal alteration of a 1-km section through the upper oceanic-crust, deep-sea drilling project Hole 504b Mineralogy, chemistry, and evolution of seawater-basalt interactions, *J. Geophys. Res.*, *91*(B10), 309 335, doi:10.1029/JB091iB10p10309.

Anderson, R. N., and M. D. Zoback (1982), Permeability, underpressures, and convection in the oceanic-crust near the Costa-Rica Rift, eastern equatorial pacific, *J. Geophys. Res.*, *87*(NB4), 2860 2868, doi:10.1029/JB087iB04p02860.

Anderson, R. N., et al. (1982), DSDP Hole-504b, the 1st reference section over 1km through layer-2 of the oceanic-crust, *Nature*, *300*(5893), 589 594, doi:10.1038/300589a0.

Anderson, R. N., H. Omalley, and R. L. Newmark (1985), Use of geophysical logs for quantitative-determination of fracturing, alteration, and lithostratigraphy in the upper oceanic-crust, Deep-Sea Drilling Project, Hole-504b and Hole-556, *Init. Rep. Deep Sea Drill. Proj.*, *83*(Apr), 443 478, doi:10.2973/dsdp.proc.83.126.1985.

Bani-Hassan, N., K. Iyer, L. H. Ruepke, and A. Borgia (2012), Controls of bathymetric relief on hydrothermal fluid flow at mid-ocean ridges, *Geochem. Geophys. Geosyst.*, *13*(5), Q05002, doi:10.1029/2012GC004041.

Bartetzko, A., and A. T. Fisher (2008), Physical properties of young (3.5 Ma) oceanic crust from the eastern flank of the Juan de Fuca Ridge: Comparison of wireline and core measurements with global data, *J. Geophys. Res.*, *113*, B05105, doi:10.1029/2007JB005268.

Becker, K. (1990), Measurements of the permeability of the upper oceanic crust at Hole 395A, ODP Leg 109, in *Proc. Ocean Drill. Program, Sci. Results*, edited by R. Detrick et al., pp. 213 222, Ocean Drill. Program, College Station, Tex.

Becker, K., and E. E. Davis (2003), New evidence for age variation and scale effects of permeabilities of young oceanic crust from borehole thermal and pressure measurements, *Earth Planet. Sci. Lett.*, *210*(3-4), 499 508, doi:10.1016/s0012-821x(03)00160-2.

Becker, K., and E. Davis (2004), In situ determinations of the permeability of the igneous oceanic crust, in *Hydrogeology of the Oceanic Lithosphere*, edited by E. E. Davis and H. Elderfield, pp. 189 224, Cambridge Univ. Press, Cambridge, U. K.

Becker, K., and A. T. Fisher (2000), Permeability of upper oceanic basement on the eastern flank of the Juan de Fuca Ridge determined with drill-string packer experiments, *J. Geophys. Res.*, *105*(B1), 897 912, doi:10.1029/1999JB900250.

Becker, K., and A. T. Fisher (2008), Borehole packer tests at multiple depths resolve distinct hydrologic intervals in 3.5-Ma upper oceanic crust on the eastern flank of Juan de Fuca Ridge, *J. Geophys. Res.*, *113*, B07105, doi:10.1029/2007JB005446.

Becker, K., et al. (1982), Insitu electrical-resistivity and bulk porosity of the oceanic-crust Costa-Rica Rift, *Nature*, *300*(5893), 594 598, doi:10.1038/300594a0.

Becker, K., M. G. Langseth, R. P. Vonherzen, and R. N. Anderson (1983), Deep crustal geothermal measurements, Hole-504b, Costa-Rica Rift, *J. Geophys. Res.*, *88*(NB4), 3447 3457, doi:10.1029/JB088iB04p03447.

Becker, K., M. G. Langseth, R. P. Vonherzen, R. N. Anderson, and M. A. Hobart (1985), Deep crustal geothermal measurements, Hole-504b, Deep-Sea Drilling Project Legs 69, 70, 83, and 92, *Init. Rep. Deep Sea Drill. Proj.*, *83*(Apr), 405 418, doi:10.2973/dsdp.proc.83.123.1985.

Becker, K., et al. (1989), Drilling deep into young oceanic-crust, Hole-504b, Costa-Rica Rift, *Rev. Geophys.*, *27*(1), 79 102, doi:10.1029/RG027i001p00079.

Becker, K., A. Bartetzko, and E. E. Davis (2001), Leg 174B synopsis: Revisiting Hole 395A for logging and longterm monitoring of off-axis hydrothermal processes in young oceanic crust, in *Proc. Ocean Drill. Program Sci. Results* 174B, edited by K. Becker and M. J. Malone, pp. 1 13, Ocean Drill. Program, College Station, Tex.

Becker, K., E. E. Davis, F. N. Spiess, and C. P. deMoustier (2004), Temperature and video logs from the upper oceanic crust, Holes 504B and 896A, Costa Rica Rift flank: Implications for the permeability of upper oceanic crust, *Earth Planet. Sci. Lett.*, *222*(3-4), 881 896, doi:10.1016/j.epsl.2004.03.033.

Broglia, C., and D. Moos (1988), In-situ structure and properties of 110-ma crust from geophysical logs in DSDP Hole 418A, in *Proc. Ocean Drill. Program Sci. Results*, edited by M. H. Salisbury, pp. 29 47, Ocean Drilling Program, College Station, Tex.

Cann, J. R., and R. P. VonHerzen (1983), Downhole logging at Deep Sea Drilling Project sites 501, 504, and 505, near the Costa Rica Rift, *Init. Rep. Deep Sea Drill. Proj.*, *69*, 281 299, doi:10.2973/dsdp.proc.69.110.1983.

Chib, S., and E. Greenberg (1995), Understanding the Metropolis-Hastings algorithm, *Am. Stat.*, *49*(4), 327 335, doi:10.2307/2684568.

Civan, F. (2001), Scale effect on porosity and permeability: Kinetics, model, and correlation, *AIChE J.*, *47*(2), 271 287, doi:10.1002/aic.690470206.

Clauser, C. (1992), Permeability of crystalline rocks, *Trans. AGU*, *73*(233), 237 238, doi:10.1029/91EO00190.

Costa Rica Rift United Scientific Team (1982), Geothermal regimes of the Costa Rica Rift, East Pacific, investigated by drilling, DSDP-IPOD legs 68, 69, and 70, Geological Society of America Bulletin, September, 1982, v. 93, no. 9, p. 862-875, doi:10.1130/0016-7606(1982)93<862:GROTCR>2.0.CO;2.

Davis, E. E. (1988), Oceanic heat-flow density, in *Handbook of Terrestrial Heat-Flow Density Determination*, edited by R. Haenel, L. Rybach and L. Stegena, pp. 223 260, Springer, Kluwer, Amsterdam.

Davis, E. E., and C. R. B. Lister (1977), Heat flow measured over the Juan de Fuca Ridge: Evidence for widespread hydrothermal circulation in a highly heat transportive crust, *J. Geophys. Res.*, *82*, 4845 4860, doi:10.1029/0JGREA000082000B30004845000001.

Davis, E. E., and K. Becker (2002), Observations of natural-state fluid pressures and temperatures in young oceanic crust and inferences regarding hydrothermal circulation, *Earth Planet. Sci. Lett.*, *204*(1-2), 231 248, doi:10.1016/s0012-821x(02)00982-2.

Davis, E. E., and K. Becker (2004), Observations of temperature and pressure: Constraints on ocean crustal hydrologic state, properties, and flow, in *Hydrogeology of the Oceanic Lithosphere*, edited by E. E. Davis and H. Elderfield, pp. 225 271, Cambridge Univ. Press, Cambridge, U. K.

Davis, E. E., et al. (1992), FlankFlux An experiment to study the nature of hydrothermal circulation in young oceanic-crust, *Can. J. Earth Sci.*, *29*(5), 925 952.

Davis, E. E., D. S. Chapman, H. Villinger, S. Robinson, J. Grigel, A. Rosenberger, and D. Pribnow (1997a), *Seafloor heat flow on the eastern flank of the Juan de Fuca Ridge: Data from 1FlankFlux1 studies through 1995*, edited by E. E. Davis, A. T. Fisher and J. V. Firth, pp. 23 33, Ocean Drill. Program, College Station, Tex.

Davis, E. E., et al. (1997b), Hydrothermal circulation in the oceanic crust; eastern flank of the Juan de Fuca Ridge, *Proc. Ocean Drill. Program Init. Rep.*, *168*, 470, doi:10.2973/odp.proc.ir.168.1997.

Edmond, J. M., C. Measures, R. E. McDuff, L. H. Chan, R. Collier, B. Grant, L. I. Gordon, and J. B. Corliss (1979), Ridge crest hydrothermal activity and the balances of the major and minor elements in the ocean: The Galapagos data, *Earth Planet. Sci. Lett.*, *46*, 1 18.

Edwards, K. J., C. G. Wheat, and J. B. Sylvan (2011), Under the sea: microbial life in volcanic oceanic crust, *Nat. Rev. Microbiol.*, *9*(10), 703 712, doi:10.1038/nrmicro2647.

Elderfield, H., and A. Schultz (1996), Mid-ocean ridge hydrothermal fluxes and the chemical composition of the ocean, *Annu. Rev. Earth Planet. Sci.*, *24*, 191 224, doi:10.1146/annurev.earth.24.1.191.

Expedition 301 Scientists (2005a), Site 1026, *Proc. Integrated Ocean Drill. Program, Exped. Rep. 301*, 396 409, doi:10.2204/iodp.proc.301.107.2005.

Expedition 301 Scientists (2005b), Site U1301, *Proc. Integrated Ocean Drill. Program, Exped. Rep. 301*, 215 395, doi:10.2204/iodp.proc.301.106.2005.

Fine, R. A., and F. J. Millero (1973), Compressibility of water as a function of temperature and pressure, *J. Chem. Phys.*, *59*(10), 5529 5536, doi:10.1063/1.1679903.

Fisher, A. T. (1998), Permeability within basaltic oceanic crust, *Rev. Geophys.*, *36*(2), 143 182, doi:10.1029/97RG02916.

Fisher, A. T. (2004), Rates and patterns of fluid circulation, in *Hydrogeology of the Oceanic Lithosphere*, edited by E. E. Davis and H. Elderfield, pp. 339 377, Cambridge Univ. Press, Cambridge, U. K.

Fisher, A. T. (2010), IODP Expedition 321T; cementing operations at Holes U1301A and U1301B, eastern flank of the Juan de Fuca Ridge, *Prel. Rept. Integrated Ocean Drill. Program*, 321T, 9, 16 19, doi:10.2204/iodp.sd.9.02.2010.

Fisher, A. T., K. Becker, T. N. Narasimhan, M. G. Langseth, and M. J. Mottl (1990), Passive, off-axis convection through the southern flank of the Costa-Rica Rift, *J. Geophys. Res.*, *95*(B6), 9343 9370, doi:10.1029/JB095iB06p09343.

Fisher, A. T., K. Becker, and E. E. Davis (1997), The permeability of young oceanic crust east of Juan de Fuca Ridge determined using borehole thermal measurements, *Geophys. Res. Lett.*, *24*(11), 1311 1314, doi:10.1029/97GL01286.

Fisher, A. T., et al. (2005), Scientific and technical design and deployment of long-term subseafloor observatories for hydrogeologic and related experiments, IODP Expedition 301, eastern flank of Juan de Fuca Ridge, in *Proc. Integrated Ocean Drill. Program*, edited by A. T. Fisher, T. Urabe and A. Klaus, p. 39, Integrated Ocean Drilling Program, College Station, Tex.

Fisher, A. T., E. E. Davis, and K. Becker (2008), Borehole-to-borehole hydrologic response across 2.4 km in the upper oceanic crust: Implications for crustal-scale properties, *J. Geophys. Res.*, *113*, B07106, doi:10.1029/2007JB005447.

Gable, R., R. H. Morin, and K. Becker (1989), Geothermal state of Hole 504B, ODP Leg 111 overview, *Proc. Ocean Drill. Program*, *111*, 87 96, doi:10.2973/odp.proc.sr.111.135.1989.

Gable, R., R. H. Morin, and K. Becker (1992), Geothermal state of DSDP Hole-395A and Hole-534A Results from the Dianaut Program, *Geophys. Res. Lett.*, *19*(5), 505 508, doi:10.1029/92GL00333.

Gable, R., R. H. Morin, K. Becker, and P. Pezard (1995), Heat flow in the upper part of the oceanic crust; synthesis of in-situ temperature measurements in Hole 504B, *Proc. Ocean Drill. Program*, *137/140*, 321 324, doi:10.2973/odp.proc.sr.137140.036.1995.

Gallagher, K., K. Charvin, S. Nielsen, M. Sambridge, and J. Stephenson (2009), Markov chain Monte Carlo (MCMC) sampling methods to determine optimal models, model resolution and model choice for Earth Science problems, *Mar. Pet. Geol.*, *26*(4), 525 535, doi:10.1016/j.marpetgeo.2009.01.003.

Guerin, G., K. Becker, R. Gable, and P. A. Pezard (1996), Temperature measurements and heat-flow analysis in Hole 504B, *Proc. Ocean Drill. Program*, *148*, 291 296, doi:10.2973/odp.proc.sr.148.141.1996.

Hartline, B. K., and C. R. B. Lister (1981), Topographic forcing of supercritical convection in a porous-medium such as the oceanic-crust, *Earth Planet. Sci. Lett.*, *55*(1), 75 86, doi:10.1016/0012 821x(81)90088-1.

Hutnak, M., A. T. Fisher, L. Zuhlsdorff, V. Spiess, P. H. Stauffer, and C. W. Gable (2006), Hydrothermal recharge and discharge guided by basement outcrops on 0.7-3.6 Ma seafloor east of the Juan de Fuca Ridge: Observations and numerical models, *Geochem. Geophys. Geosyst.*, *7*, Q07O02, doi:10.1029/2006GC001242.

Jacobson, R. S. (1992), Impact of crustal evolution on changes in the seismic properties of the uppermost oceanic crust, *Rev. Geophys.*, *30*, 23 42.

Jaeger, J. C. (1942), Heat flow in the region bounded internally by a circular cylinder, *Proc. R. Soc. Edinburgh A*, *61*(3), 223 228, doi:10.1017/S0080454100006233.

Jaeger, J. C. (1961), Effect of drilling fluid on temperatures measured in bore holes, *J. Geophys. Res.*, *66*(2), 563 569, doi:10.1029/JZ066i002p00563.

Jaeger, J. C. (1965), Application of the theory of heat conduction to geothermal measurements, in *Terrestrial Heat Flow, Geophys. Monogr. Ser.*, vol. 8, edited by W. H. K. Lee, pp. 7 23, AGU, Washington, D. C., doi:10.1029/GM008p0007.

Jaeger, J. C., and M. Clarke (1942), A short table of I(O, I; x), *Proc. R. Soc. Edinburgh A*, *61*, 229 230, doi:10.1017/S0080454100006245.

Jarrard, R. D., L. J. Abrams, R. Pockalny, R. L. Larson, and T. Hirono (2003), Physical properties of upper oceanic crust: Ocean drilling program Hole 801C and the waning of hydrothermal circulation, *J. Geophys. Res.*, *108*(D7), 2188, doi:10.1029/2001JB001727.

Kelley, D. S., J. A. Baross, and J. R. Delaney (2002), Volcanoes, fluids, and life at mid-ocean ridge spreading centers, *Annu. Rev. Earth Planet. Sci.*, *30*, 385 491, doi:10.1146/annurev.earth.30.091201.141331.

Langseth, M. G. (1990), Cooling of deep sea boreholes by circulation and implications for logging techniques in high temperature holes, *Sci. Drill.*, *1*, 231 237.

Lesem, L. B., F. Greytok, F. Marotta, and J. J. McKetta (1957), A method of calculating the distribution of temperature in flowing gas wells, *Trans. Am. Inst. Min. Metall. Eng.*, *210*(6), 169 176.

Matthews, C. S., and D. G. Russell (1967), Pressure Buildup and Flow Tests in Wells, Soc. of Pet. Eng., New York, NY.

Moos, D. (1990), Petrophysical results from logging in DSDP Hole 395A, *Proc. Ocean Drill. Program*, *106/109*, 237 253, doi:10.2973/odp.proc.sr.106109.150.1990.

Mottl, M. (2003), Partitioning of energy and mass fluxes between mid-ocean ridge axes and flanks at high and low temperature, in *Energy and Mass Transfer in Submarine Hydrothermal Systems*, edited by P. Halbach, V. Tunnicliffe and J. Hein, pp. 271 286, Dahlem Univ. Press, Berlin, Germany.

Newmark, R. L., R. N. Anderson, D. Moos, and M. D. Zoback (1985), Sonic and ultrasonic logging of Hole-504b and its implications for the structure, porosity, and stress regime of the upper 1 km of the oceanic-crust, *Init. Rep. Deep Sea Drill. Proj.*, *83*(Apr), 479 510, doi:10.2973/dsdp.proc.83.127.1985.

Orcutt, B. N., W. Bach, K. Becker, A. T. Fisher, M. Hentscher, B. M. Toner, C. G. Wheat, and K. J. Edwards (2010), Life in young ocean crust: Insights from subsurface microbial observatories, *Geochim. Cosmochim. Acta*, *74*(12), A778 A778, doi:10.1038/ismej.2010.157.

Pribnow, D. F. C., E. E. Davis, and A. T. Fisher (2000), Borehole heat flow along the eastern flank of the Juan de Fuca Ridge, including effects of anisotropy and temperature dependence of sediment thermal conductivity, *J. Geophys. Res.*, *105*(B6), 13,449 13,456, doi:10.1029/2000JB900005.

Shampine, L. F. (2008), Vectorized adaptive quadrature in MATLAB, *J. Comput. Appl. Math.*, *211*(2), 131 140, doi:10.1016/j.cam.2006.11.021.

Sharqawy, M. H., J. H. Lienhard, and S. M. Zubair (2010), Thermophysical properties of seawater: A review of existing correlations and data, *Desalin. Water Treat.*, *16*(1-3), 354 380, doi:10.5004/dwt.2010.1079.

Spinelli, G. A., and A. T. Fisher (2004), Hydrothermal circulation within topographically rough basaltic basement on the Juan de Fuca Ridge flank, *Geochem. Geophys. Geosyst.*, *5*, Q02001, doi:10.1029/2003GC000616.

Spinelli, G. A., E. G. Giambalvo, and A. T. Fisher (2004), Sediment permeability, distribution, and influence on fluxes in oceanic basement, in *Hydrogeology of the Oceanic Lithosphere*, edited by E. E. Davis and H. Elderfield, Cambridge Univ. Press, Cambridge, U. K.

Stein, C. A., S. Stein, and A. M. Pelayo (1995), Heat flow and hydrothermal circulation, in *Seafloor Hydrothermal Systems: Physical, Chemical, Biological and Geological Interactions*, edited by S. E. Humphris et al., pp. 425 445, AGU, Washington, D. C.

Stein, J. S., and A. T. Fisher (2003), Observations and models of lateral hydrothermal circulation on a young ridge flank: Numerical evaluation of thermal and chemical constraints, *Geochem. Geophys. Geosyst.*, *4*(3), 1026, doi:10.1029/2002GC000415.

Tierney, L. (1994), Markov-chains for exploring posterior distributions, *Ann. Stat.*, *22*(4), 1701 1728, doi:10.1214/aos/1176325750.

Wang, K. L., J. H. He, and E. E. Davis (1997), Influence of basement topography on hydrothermal circulation in sediment-buried igneous oceanic crust, *Earth Planet. Sci. Lett.*, *146*(1-2), 151 164, doi:10.1016/s0012 821x(96)00213-0.

Wheat, C. G., H. Elderfield, M. J. Mottl, and C. Monnin (2000), Chemical composition of basement fluids within an oceanic ridge flank: Implications for along-strike and across-strike hydrothermal circulation, *J. Geophys. Res.*, *105*(B6), 13,437 13,447, doi:10.1029/2000JB900070.

Wheat, C. G., H. W. Jannasch, A. T. Fisher, K. Becker, J. Sharkey, and S. Hulme (2010), Subseafloor seawater-basalt-microbe reactions: Continuous sampling of borehole fluids in a ridge flank environment, *Geochem. Geophys. Geosyst.*, *11*, Q07011, doi:10.1029/2010GC003057.

Wilkens, R. H., M. G. Langseth, J. R. Cann, and R. P. VonHerzen (1983), Physical properties of sediments of the Costa Rica Rift, Deep Sea Drilling Project sites 504 and 505, *Init. Rep. Deep Sea Drill. Proj.*, *69*, 659 673, doi:10.2973/dsdp.proc.69.140.1983.

Chapter Two

SUSTAINABILITY AND DYNAMICS OF OUTCROP-TO-OUTCROP HYDROTHERMAL CIRCULATION

Submitted: Winslow, D. M., and A. T. Fisher (2015), Sustainability and dynamics of outcrop-to-outcrop hydrothermal circulation, *Nature Communications*, **In Review.**

Abstract

Most seafloor hydrothermal circulation occurs far from the magmatic influence of mid-ocean ridges, driving large flows of water, heat and solutes through volcanic rock outcrops on ridge flanks. We create three-dimensional simulations of ridge-flank hydrothermal circulation, flowing between and through seamounts, to determine what controls hydrogeologic sustainability, flow rate, and the preferred flow direction in these systems. We find that sustaining flow between outcrops that penetrate less permeable sediment depends on a contrast in transmittance (the product of outcrop permeability and the area of outcrop exposure) between recharging and discharging sites, with discharge favored through less transmissive outcrops. Many simulations include local discharge through outcrops at the recharge end of an outcrop-to-outcrop system, as observed at field sites. In addition, smaller discharging outcrops sustain higher flow rates than do larger outcrops, which may help to explain how so much lithospheric heat is extracted on a global basis by this process.

2.1 Introduction

Ridge-flank hydrothermal circulation through the volcanic ocean crust is responsible for the majority of the seafloor heat flux deficit[*Stein and Stein*, 1992], drives solute fluxes between the crust and the ocean[*de Villiers and Nelson*, 1999; *Wheat and Mottl*, 2004] and supports a vast and diverse crustal biosphere[*Cowen et al.*, 2003;

Edwards et al., 2005]. Basement outcrops allow massive hydrothermal flows to bypass marine sediments that generally have much lower permeability than the underlying volcanic rocks[*Baker et al.*, 1991; *Fisher and Becker*, 2000; *Villinger et al.*, 2002; *Fisher et al.*, 2003b]. Although bare volcanic rock is common close to seafloor spreading centers, where the crust is young, widely spaced rock outcrops provide the primary pathways for hydrothermal exchange of fluid, heat and solutes between crust and the ocean on older and more heavily sedimented ridge flanks[*Fisher et al.*, 2003a, 2003b; *Hutnak et al.*, 2008; *Anderson et al.*, 2012]. Flow between rock outcrops, which can be separated laterally by tens of kilometers, is driven by a hydrothermal siphon, where the primary impelling force is generated by the difference in density between recharging (cool) and discharging (warm) columns of crustal fluid[*Fisher et al.*, 2003b; *Hutnak et al.*, 2006; *Fisher and Wheat*, 2010]. However, factors controlling flow sustainability, rate, and direction in these hydrothermal siphon systems have not previously been explained.

We use three-dimensional, transient simulations of ridge-flank hydrothermal siphons to determine what physical parameters allow these systems to function, and how system properties influence fluid and heat transport, at a well-studied field site. In comparison to earlier one and two-dimensional models of similar systems[*Fisher et al.*, 2003b; *Hutnak et al.*, 2006; *Anderson et al.*, 2012], three-dimensional simulations provide a more accurate representation of crustal geometry and dynamic flow behaviors (regional mixed convection, asymmetric flow patterns, lateral heat extraction adjacent to three-dimensional fluid flow paths). The outcrop geometry and the range of sediment and basement properties simulated are guided by conditions observed 100 km east of the Juan de Fuca Ridge[*Davis et al.*, 1992], northeastern Pacific Ocean, where thermal, geochemical and hydrogeologic field observations show that a hydrothermal siphon is presently active[*Wheat et al.*, 2000; *Fisher et al.*, 2003b]. Using the geometry and properties of this field site as a guide, we investigate the mechanisms controlling regional-scale flow behavior that supports a self-sustaining hydrothermal siphon. Simulations are assessed in terms of their ability to reproduce key observational constraints on the character of regional flow: a hydrothermal siphon operates between the two outcrops 50 km apart, discharging ~5–20 kg s^{-1} of fluid and 1-3 MW of heat[*Thomson et al.*, 1995; *Mottl et al.*, 1998; *Wheat et al.*, 2004], and does not result in regional heat-flux suppression at the seafloor[*Hutnak et al.*, 2006]. Additional characteristics of this field area are described in Methods.

We simulated fluid and heat transport with FEHM, a fully coupled and transient model that employs a finite volume method to solve flow equations[*Zyvoloski et al.*, 2011]. Simulation domains are 130 km long, 80 km wide, and 4 km thick, with no-flow side boundaries, lithospheric heating from below (varying with position according to crustal age), constant (bottom-water) temperature at the top (seafloor), and seafloor pressure varying with water depth (Fig. 2-1). Two volcanic rock outcrops are separated by 50 km, penetrating upward from a flat crustal aquifer and extending 65 to 500 m above an otherwise-continuous sediment layer. Simulations presented in the main text of this study were started with a pre-existing hydrothermal siphon running between the two outcrops, to distinguish the investigation of siphon sustainability from issues associated with initial siphon formation, although similar behaviors were observed in simulations started from a hydrostatic initial condition. Each simulation was run until a dynamic steady state was achieved, wherein transient behaviors persisted (e.g. mixed convection, unstable secondary convection, local circulation) and recharge and discharge rates through outcrops stabilized to ± 0.1% per kyr of simulation time.

Here we present the first transient, three-dimensional simulations of outcrop-to-outcrop hydrothermal siphons on the seafloor, and explore the parameter space under which a siphon is sustained. We identify key controls on system behavior (outcrop size, permeability) and provide a mechanistic explanation as to why some systems sustain hydrothermal siphons whereas others do not. Model results indicate that, for the geometry and range of properties tested, a significant contrast in outcrop properties is required for a hydrothermal siphon to be sustained, and that discharge is favored through the outcrop which is more restrictive to flow. This helps to explain field observations indicating that small outcrops tend to be sites of hydrothermal discharge[*Fisher et al.*, 2003b; *Davis and Becker*, 2004; *Hutnak et al.*, 2008], and suggests that small outcrops may play an especially important role in extracting lithospheric heat from the oceanic crust.

2.2 Results

For simulations that sustain a hydrothermal siphon, net lateral fluid transport in the upper crustal aquifer occurs from the recharge site toward the discharge site, although one or both outcrops may recharge and discharge fluids simultaneously (Fig. 2-2). Typical flow behaviors in simulations consistent with field observations include a temperature difference at the base of recharging and discharging fluid columns of ~60°C, mixed convection within the crustal aquifer between outcrops, and insufficient fluid flow through seafloor sediments to cause measurable thermal or chemical perturbations (Fig. 2-2). Typical pressure differences in the crustal aquifer between the base of recharge and discharge sites are 20-100 kPa, consistent with differential pressures measured with subseafloor observatories on the eastern flank of the Juan de Fuca Ridge[*Davis and Becker*, 2002].

The mass rate of siphon flow (Q_S) is calculated by subtracting simulated recharge from discharge at the discharge site; the fraction of total outcrop discharge passing through the siphon (F_S) is ≤ 0.75, and generally scales with Q_S. An upper crustal aquifer permeability (k_{aq}) of ~10^{-12} m^2 is necessary to sustain the hydrothermal siphon and match typical flow characteristics at the field site (Fig. 2-2). Higher k_{aq} generally results in higher Q_S than observed, accompanied by excessive lowering of temperatures at the sediment-basement interface, and leading to excessive regional heat extraction, whereas lower k_{aq} results in lower Q_S or fails to sustain a hydrothermal siphon between outcrops.

We define transmittance (T, m^4) as the outcrop permeability times the area of outcrop exposure at the seafloor (k x A), a measure of the capacity of a rock outcrop to transmit fluid as part of a hydrothermal siphon. Two sets of simulations illustrate how outcrop properties affect siphon behavior. In the first set, we modify T at the discharge site (variable T_D) by changing both outcrop size and permeability (Table 2-1), while holding outcrop properties fixed at the recharge site (constant T_R) (Fig. 2-3). Hydrothermal siphons in these simulations transmit $Q_S \leq 60$ kg s^{-1}, with Q_S generally increasing with T_D until the siphon fails. In the second set of simulations, with two outcrops of equal size, we vary T by modifying outcrop permeability only. These simulations generate similar behaviors but lower siphon discharge rates ($Q_S \leq 18$ kg s^{-1}) (Fig. 2-4). For both sets of simulations, hydrothermal siphons are sustained only when $T_D/T_R < 0.1$, with Q_S tending to be greatest at somewhat lower T_D/T_R values (Fig. 2-4). In addition, every simulation that sustained a hydrothermal siphon did so with the lower-T outcrop becoming the primary site of siphon discharge, even when siphon flow was initiated in the opposite direction.

2.3 Discussion

These simulations demonstrate that, given sufficiently high permeability in the crustal aquifer, the variability of volcanic outcrop transmittance determines both (a) whether or not a hydrothermal siphon can be sustained, and (b) the dominant siphon flow direction. A flow restriction at a ridge-flank discharge site (low T_D) slows the overall rate of siphon transport, allowing the fluid to be warmed by lithospheric heat, which increases the impelling force for the siphon. At the same time, relatively high permeability in the crustal aquifer allows the pressure difference between recharging and discharging ends of the siphon to drive lateral flow with minimal energy loss. In cases where the difference in outcrop properties is smaller ($T_D/T_R > 0.1$), the pressure difference between the crust below the outcrops may be insufficient to overcome viscous losses in the intervening aquifer, rendering the siphon unsustainable. The abrupt transition in behavior between systems that sustain siphons and those that do not (Fig. 2-3) indicates that the transmittance ratio exerts a fundamental control on siphon sustainability in systems of this kind. The transition occurs at $T_D/T_R \sim 0.1$ for the geometry and properties assigned in this study, but this transition will likely shift in systems having different outcrop spacing, aquifer thickness, and/or permeability.

The finding that hydrothermal siphons tend to discharge through outcrops with lower T is consistent with field observations suggesting that discharge is favored through smaller outcrops[*Fisher et al.*, 2003b; *Davis and Becker*, 2004; *Hutnak et al.*, 2008]. In addition, it has been proposed that higher temperature ("black smoker") hydrothermal vents on mid-ocean ridges tend to discharge at sites where there is a flow restriction[*Strens and Cann*, 1982, 1986; *Germanovich and Lowell*, 1992; *Lowell et al.*, 1993]. Although mid-ocean ridge hydrothermal systems include many characteristics that are not found on volcanically inactive ridge flanks (e.g., phase separation of flowing fluids, development of a cracking front, faster rates of reaction), the consistency of this trend could indicate a fundamental behavior of subseafloor hydrogeologic systems driven by lithospheric heat.

Although outcrop transmittance comprises the primary control on siphon behavior in our simulations, outcrop size has an additional influence. Simulations having smaller outcrops as discharge sites yield higher Q_S and F_S than those with larger outcrops having equivalent T_D (Fig. 2-3). This may occur because, given a particular flow rate (limited mainly by system geometry, aquifer permeability, and available heating from below), higher temperatures in ascending crustal fluids are thermodynamically easier to maintain in small outcrops than in large outcrops. A warmer column of discharging fluid creates a larger difference in fluid pressure between the base of recharging and discharging outcrops, generating larger lateral driving forces and flow rates within the underlying crust. Small outcrops also tend to be dominated by the thermal influence of one direction of fluid flow, as less space is available for flow paths to develop in both directions. Thus, once a small outcrop is established as a discharge site, local recharge (and associated crustal cooling) is inhibited, boosting F_S. These results suggest that outcrops smaller than ~2 km in diameter, which are thought to be abundant globally but are generally undetectable with satellite gravimetric data[*Kim and Wessel*, 2011], may have a disproportionate influence on lithospheric heat extraction. This may explain why so few sites of ridge-flank hydrothermal discharge, a global process responsible for 25% of Earth's geothermal heat loss, have been identified to date: the vast majority of sites where this process occurs remain unmapped and unexplored.

In simulations that sustain a hydrothermal siphon through two larger outcrops (differences in T result entirely from differences in k), F_S is generally low enough to allow significant outcrop-local circulation (Fig. 2-4). Both outcrops generate local recharge and discharge in these simulations, even in those sustaining a hydrothermal siphon. Simultaneous recharge and discharge through large outcrops that are thought to be sites of hydrothermal siphon recharge has been observed at field sites[*Hutnak et al.*, 2006, 2008; *Wheat et al.*, 2013]. That the hydrothermal siphon fails when $T_D/T_R >$ 0.1 demonstrates the additional possibility that local (single-outcrop) hydrothermal circulation systems can develop within proximal outcrops between which there is no siphon flow, even if there is a permeable aquifer connecting them.

The minimum aquifer permeability required to sustain an outcrop-to-outcrop hydrothermal siphon in this study, $k_{aq} = 10^{-12}$ m^2, is well represented by the global dataset of *in-situ* permeability measurements in the upper ocean crust (Fig. 2-5). This permeability value is at the lower end of values estimated with one-dimensional analytical calculations[*Fisher and Becker*, 2000; *Fisher et al.*, 2003b], and lower than inferred from two-dimensional simulations based on an equivalent geometry[*Hutnak et al.*, 2006]. Three-dimensional numerical simulations may result in more fluid flow and heat extraction than do one- and two-dimensional simulations with equivalent permeability because the three-dimensional simulations result in advective heat extraction focused within a comparatively small area. This allows recharging and discharging fluid columns in the crust to be relatively isothermal, maximizing the driving force for siphon flow. In contrast, two-dimensional simulations treat volcanic outcrops as "ridges" that extend to infinity in and out of the plane of the simulation, so a smaller fraction of crustal heat is advected per area of two-dimensional outcrop, and higher aquifer k_{aq} is required for the siphon to be sustained.

The simulations presented in this study were developed for an end-member of ridge-flank hydrothermal systems, based on a field site where there is considerable understanding of system geometry, crustal properties, and flow fluid rates[*Davis et al.*, 1992; *Mottl et al.*, 1998; *Fisher et al.*, 2003b; *Wheat et al.*, 2004; *Hutnak et al.*, 2006]. This field site sustains an outcrop-to-outcrop hydrothermal siphon that operates at a relatively low flow rate (tens of kg s^{-1}) at present, but likely operated much more vigorously in the past when sediment cover was thinner and less extensive, and there was a larger network of exposed basement outcrops[*Hutnak and Fisher*, 2007]. On a global basis, outcrop-to-outcrop circulation systems are generally more efficient at extracting lithospheric heat than is the system operating presently at this field site[*Stein and Stein*, 1992; *Fisher and Becker*, 2000; *Villinger et al.*, 2002; *Anderson et al.*, 2012]. Based on trends from simulations presented herein (Figs. 3, 4), higher fluid flow rates between outcrops cannot be generated by larger differences between T_R and T_D alone (holding other parameters with ranges simulated). Instead, achieving greater basement cooling and a larger reduction in seafloor heat flux likely requires higher aquifer permeability and/or an outcrop geometry that allows faster fluid flow rates through the upper crust. We hypothesize that one or both of these conditions help to explain the global heat flux anomaly on ridge flanks, and may account for even more extreme cases of highly efficient heat extraction from these systems[*Davis et al.*, 1992; *Villinger et al.*, 2002; *Hutnak et al.*, 2008].

2.4 Methods

2.4.1 Computational methods

The numerical model used in this study, Finite Element Heat and Mass (FEHM), was developed at Los Alamos National Laboratory for analyzing complex hydrogeologic systems[*Zyvoloski et al.*, 2011]. FEHM is node-centered and was run with a Delaunay mesh of tetrahedral elements, incorporating a finite volume approach to representing properties and flows between nodes. Darcy's law governs fluid flow in these simulations, and flow rates calculated in the present study are consistent with this approximation (e.g., laminar flow). FEHM is fully coupled and transient, with flow potential and fluid properties (and thus the vector components defining the three-dimensional flow field) being updated with each time step. For this study, we applied FEHM with a solver that is fully implicit with upstream weighting.

All simulations in this study were run for $\geq 10^5$ years of simulation time (1,000 – 2,000 time steps), sufficient to reach a dynamic steady state such that recharge and discharge rates from outcrops stabilized to ± 0.1% per kyr of simulation time, requiring runtimes of 1 to 10 days on a desktop (Linux) workstation. Whole grid mass and energy conservation were confirmed for simulations at dynamic steady state, finding the apparent "imbalance" between input and output to be <3% at late times. These apparent imbalances arise mainly because of very low rates of fluid transport (at rates too small to be detected in the field, <0.1 mm/yr) across a large seafloor area. These very slow flows become a percentage of flow through outcrops only because outcrop flows are relatively small for the field setting used as the basis for simulations presented in this study. Apparent imbalances also occur because flows through the whole crustal system ($>4 \times 10^4$ km^3) continue to be irregular and oscillatory, with water moving into and out of storage at all times. Internal mass balance errors, calculated by FEHM during solution iteration, are <<1%.

2.4.2 Grid development and resolution

Grid geometries for simulations shown in this study comprise of $\sim 4 \times 10^5$ nodes and $\sim 2.2 \times 10^6$ elements. Initial simulations were performed using coarser grids, which yielded somewhat different local convection patterns, but siphon flow and sustainability were otherwise robust to differences in grid resolution. Grid resolution is highest within the aquifer and outcrops, with typical node spacing of 50-225 m, consistent with grid spacing used in earlier, two-dimensional models of ridge-flank hydrothermal systems[*Davis et al.*, 1997; *Wang et al.*, 1997; *Stein and Fisher*, 2003; *Spinelli and Fisher*, 2004; *Hutnak et al.*, 2006]. Cells are coarser within the sediment (200-500 m node spacing) and the low-permeabilty basalt layer underlying the aquifer (150-2000 m spacing), both of which experience no measurable flow based on thermal and/or geochemical measurements (≤0.1 mm/yr). Areas of the domain located ≥10 km horizontally from a volcanic rock outcrops also have larger node spacing to improve computational efficiency. The relatively thick section of low-permeability volcanic rock below the crustal aquifer allows the redistribution of lithospheric heat rising conductively from depth, which is important for capturing the full coupling between hydrothermal circulation, patterns of advective heat extraction, and conductive seafloor heat flux.

2.4.3 Initial conditions

All simulations presented above were started with the initial temperature and pressure conditions of an active outcrop-to-outcrop hydrothermal siphon. Generating this state requires a series of steps, starting with a conduction only (no fluid flow) simulation that yields a thermal state consistent with the simulated geometry and physical properties. We use these results to calculate hydrostatic pressures consistent with conductive thermal conditions at each node as a function of depth, including differences in fluid density (“conductive-hydrostatic”). These initial conditions are used to start a fully coupled simulation that can spontaneously form an outcrop-to-outcrop hydrothermal siphon, given appropriate aquifer and outcrop permeabilities.

We use the fluid and formation pressure and temperature conditions that result from this flowing hydrothermal siphon as a consistent starting condition for all subsequent simulations of the same crustal geometry.

We performed a suite of simulations, across the same range of system geometries and aquifer and outcrop permeabilities discussed in the main text, in which the initial condition was "conductive-hydrostatic," rather than being based on an active outcrop-to-outcrop siphon. In almost every case, the simulated behaviors and $Q_{S,}$ at dynamic steady state when starting from "conductive-hydrostatic," were identical to those based on starting with an active siphon (Fig. 2-6). The exception was for a single simulation with different-sized outcrops and $T_D/T_R \sim 0.1$, in which an initial siphon can self-sustain under conditions where it would not develop spontaneously from "conductive-hydrostatic." We also ran subset of the simulations presented in Figs. 3 and 4 beginning from an active siphon that flows in the opposite direction. In all of these cases, the siphon either failed or spontaneously switched direction to yield identical results at dynamic steady state to those started from "conductive-hydrostatic." We focus in this study on sustaining a hydrothermal siphon, rather than developing it from "conductive-hydrostatic," to avoid convolving the influence of system properties and initial conditions on siphon behavior. Real outcrop-to-outcrop hydrothermal siphons develop through a complex history of volcanism, lithospheric cooling, sedimentation, consolidation, lithification, alteration, and tectonic processes, all of which are highly variable and details of which are poorly known at individual field sites.

2.4.4 Physical properties and outcrop geometry

The physical properties assigned to parts of each grid are summarized in Table 2-2. Individual model cells are intended to comprise representative elemental volumes, in which bulk properties apply to solid material and pore space surrounding a single node. We use homogenous and isotropic bulk properties for the volcanic (basaltic) crust, with a single value assigned to each section (the crustal aquifer, the low permeability crustal layer beneath, and two outcrop regions). Preliminary testing indicates that a more complex treatment of the crustal aquifer (anisotropy, heterogeneity) produces the same trends in regional-scale flow behavior that are described in this study, but these dependencies remain to be explored and quantified.

Sediment porosity, thermal conductivity, and permeability vary with depth to account for compaction. We used data from the field area to create representative depth-dependent functions for each property. Each function was discretized and values were assigned to nodes so that the cumulative effects of the sediment layer were accurately represented. Although there is some uncertainty in the estimates of bulk sediment properties, we find that the results of this study are robust to realistic deviations in the hydrologic and thermal properties assigned.

The values chosen for basement permeability and thickness of the crustal aquifer were based on consideration of the global borehole dataset of *in-situ* permeability measurements (Fig. 2-5), and simulations that resulted in either no sustained hydrothermal siphon ($k_{aq} \leq 10^{-13}$ m^2) or siphon flow rates and cooling within the upper crustal aquifer exceeding observations at the field site ($k_{aq} \geq 10^{-11}$ m^2). In-situ bulk permeability determinations made in basaltic ocean crust, using an inflatable packer or a temperature log in an unsealed hole, indicate permeability in the upper 300 m below the sediment-basement interface having a range of 10^{-14} to 10^{-10} m^2 (Fig. 2-5). There are few crustal permeability measurements that extend below the upper 300 m of basement, but these suggest somewhat lower values. Simulation results shown in the present study are based on crustal aquifer thickness of 300 m, which is consistent with the global permeability data set. Additional simulations show that results are comparable for thicker or thinner crustal aquifers, if the k_{aq} is proportionately adjusted such that the product of aquifer thickness and permeability remains the same.

Overall outcrop geometries are patterned after those observed on 3.5 M.y. old seafloor on the eastern flank of the Juan de Fuca Ridge[*Davis et al.*, 1992; *Fisher et al.*, 2003b], and simulated as ziggurats (flat-topped pyramids). The smallest outcrops represented in our simulations have a geometry similar to that of Baby Bare outcrop[*Mottl et al.*, 1998; *Wheat et al.*, 2004], which rises 65 m above the surrounding sediments but is the tip of a much larger volcanic edifice that is mostly buried by regionally thick and continuous turbidites and hemipelagic mud. The largest outcrops in our simulations have a geometry similar to Grizzly Bare outcrop[*Hutnak et al.*, 2006; *Wheat et al.*, 2013], rising ~500 m above the surrounding seafloor. The ratio of outcrop areas for the large and small outcrops in our simulations is ~100, and the medium-sized outcrops simulated in this study have an area and elevation that is intermediate to that of the large and small outcrops (Table 2-2).

Acknowledgments

This research was supported by National Science Foundation grants OIA-0939564, OCE-1031808 and OCE-1260408, and Consortium for Ocean Leadership Projects T327A7 and T327B7. P. Stauffer, C. Gable, and G. Zyvoloski (LANL) provided important gridding and modeling advice. E. Brodsky and G. Glatzmaier provided helpful comments on an earlier version of this study.

References

Anderson, B. W., L. A. Coogan, and K. M. Gillis (2012), The role of outcrop-to-outcrop fluid flow in off-axis oceanic hydrothermal systems under abyssal sedimentation conditions, *J. Geophys. Res.*, *117*(B5), doi:10.1029/2011JB009052.

Baker, P., P. Stout, M. Kastner, and H. Elderfield (1991), Large-scale lateral advection of seawater through oceanic-crust in the central equatorial pacific, *Earth Planet. Sci. Lett.*, *105*(4), 522–533, doi:10.1016/0012-821X(91)90189-O.

Becker, K., A. T. Fisher, and T. Tsuji (2013), New packer experiments and borehole logs in upper oceanic crust: Evidence for ridge-parallel consistency in crustal hydrogeological properties, *Geochem. Geophys. Geosystems*, *14*(8), 2900–2915, doi:10.1002/ggge.20201.

Cowen, J. P., S. J. Giovannoni, F. Kenig, H. P. Johnson, D. Butterfield, M. S. Rappe, M. Hutnak, and P. Lam (2003), Fluids from aging ocean crust that support microbial life, *Science*, *299*(5603), 120–123, doi:10.1126/science.1075653.

Davis, E. et al. (1992), Flankflux: an experiment to study the nature of hydrothermal circulation in young oceanic-crust, *Can. J. Earth Sci.*, *29*(5), 925–952, doi:10.1139/e92-078.

Davis, E. E., and K. Becker (2002), Observations of natural-state fluid pressures and temperatures in young oceanic crust and inferences regarding hydrothermal circulation, *Earth Planet. Sci. Lett.*, *204*(1), 231–248.

Davis, E. E., and K. Becker (2004), Observations of temperature and pressure: constraints on ocean crustal hydrologic state, properties, and flow, in *Hydrogeology of the Oceanic Lithosphere*, edited by E. E. Davis and H. Elderfield, pp. 225–271, Cambridge University Press, Cambridge, UK.

Davis, E. E., K. L. Wang, J. H. He, D. S. Chapman, H. Villinger, and A. Rosenberger (1997), An unequivocal case for high Nusselt number hydrothermal convection in sediment-buried igneous oceanic crust, *Earth Planet. Sci. Lett.*, *146*(1-2), 137–150, doi:10.1016/S0012-821X(96)00212-9.

Edwards, K. J., W. Bach, and T. M. McCollom (2005), Geomicrobiology in oceanography: microbe-mineral interactions at and below the seafloor, *Trends Microbiol.*, *13*(9), 449–456, doi:10.1016/j.tim.2005.07.005.

Fisher, A. T., and K. Becker (2000), Channelized fluid flow in oceanic crust reconciles heat-flow and permeability data, *Nature*, *403*(6765), 71–74, doi:10.1038/47463.

Fisher, A. T., and C. G. Wheat (2010), Seamounts as conduits for massive fluid, heat, and solute fluxes on ridge flanks, *Oceanography*, *23*(1), 74–87.

Fisher, A. T., C. A. Stein, R. N. Harris, K. Wang, E. A. Silver, M. Pfender, M. Hutnak, A. Cherkaoui, R. Bodzin, and H. Villinger (2003a), Abrupt thermal transition reveals hydrothermal boundary and role of seamounts within the Cocos Plate, *Geophys. Res. Lett.*, *30*(11), 1550, doi:10.1029/2002GL016766.

Fisher, A. T. et al. (2003b), Hydrothermal recharge and discharge across 50 km guided by seamounts on a young ridge flank, *Nature*, *421*(6923), 618–621, doi:10.1038/nature01352.

Fisher, A. T., E. E. Davis, and K. Becker (2008), Borehole-to-borehole hydrologic response across 2.4 km in the upper oceanic crust: Implications for crustal-scale properties, *J. Geophys. Res.*, *113*(B7), doi:10.1029/2007JB005447.

Fisher, A. T., J. C. Alt, and W. Bach (2014), Hydrogeologic properties, processes and alteration in the igneous ocean crust, in *Earth and Life Processes Discovered from the Subseafloor Environment - A Decade of Science Achieved by the Integrated Ocean Drilling Program (IODP)*, edited by R. Stein, D. Blackman, F. Inagaki, and H. C. Larsen, pp. 507–551, Elsevier, Amsterdam/New York.

Germanovich, L., and R. Lowell (1992), Percolation theory, thermoelasticity, and discrete hydrothermal venting, *Science*, *255*(5051), 1564–1567, doi:10.1126/science.255.5051.1564.

Hutnak, M., and A. T. Fisher (2007), Influence of sedimentation, local and regional hydrothermal circulation, and thermal rebound on measurements of seafloor heat flux, *J. Geophys. Res.*, *112*(B12), doi:10.1029/2007JB005022.

Hutnak, M., A. T. Fisher, L. Zuhlsdorff, V. Spiess, P. H. Stauffer, and C. W. Gable (2006), Hydrothermal recharge and discharge guided by basement outcrops on 0.7-3.6 Ma seafloor east of the Juan de Fuca Ridge: Observations and numerical models, *Geochem. Geophys. Geosystems*, *7*, Q07O02, doi:10.1029/2006GC001242.

Hutnak, M., A. T. Fisher, R. Harris, C. Stein, K. Wang, G. Spinelli, M. Schindler, H. Villinger, and E. Silver (2008), Large heat and fluid fluxes driven through mid-plate outcrops on ocean crust, *Nat. Geosci.*, *1*(9), 611–614, doi:10.1038/ngeo264.

Kim, S.-S., and P. Wessel (2011), New global seamount census from altimetry-derived gravity data: New global seamount census, *Geophys. J. Int.*, *186*(2), 615–631, doi:10.1111/j.1365-246X.2011.05076.x.

Lowell, R., P. Van Cappellen, and L. Germanovich (1993), Silica precipitation in fractures and the evolution of permeability in hydrothermal upflow zones, *Science*, *260*(5105), 192–194, doi:10.1126/science.260.5105.192.

Mottl, M. J. et al. (1998), Warm springs discovered on 3.5 Ma oceanic crust, eastern flank of the Juan de Fuca Ridge, *Geology*, *26*(1), 51–54, doi:10.1130/0091-7613(1998)026<0051:WSDOMO>2.3.CO;2.

Spinelli, G. A., and A. T. Fisher (2004), Hydrothermal circulation within topographically rough basaltic basement on the Juan de Fuca Ridge flank, *Geochem. Geophys. Geosystems*, *5*, Q02001, doi:10.1029/2003GC000616.

Stein, C., and S. Stein (1992), A model for the global variation in oceanic depth and heat-flow with lithospheric age, *Nature*, *359*(6391), 123–129, doi:10.1038/359123a0.

Stein, J. S., and A. T. Fisher (2003), Observations and models of lateral hydrothermal circulation on a young ridge flank: Numerical evaluation of thermal and chemical constraints, *Geochem. Geophys. Geosystems*, *4*, 1026, doi:10.1029/2002GC000415.

Strens, M., and J. Cann (1982), A model of hydrothermal circulation in fault zones at mid-ocean ridge crests, *Geophys. J. R. Astron. Soc.*, *71*(1), 225–240, doi:10.1111/j.1365-246X.1982.tb04995.x.

Strens, M., and J. Cann (1986), A fracture-loop thermal balance model of black smoker circulation, *Tectonophysics*, *122*(3-4), 307–324, doi:10.1016/0040-1951(86)90149-6.

Thomson, R. E., E. E. Davis, and B. J. Burd (1995), Hydrothermal venting and geothermal heating in Cascadia Basin, *J. Geophys. Res.-Solid Earth*, *100*(B4), 6121–6141, doi:10.1029/95JB00030.

De Villiers, S., and B. K. Nelson (1999), Detection of low-temperature hydrothermal fluxes by seawater Mg and Ca anomalies, *Science*, *285*(5428), 721–723, doi:10.1126/science.285.5428.721.

Villinger, H., I. Grevemeyer, N. Kaul, J. Hauschild, and M. Pfender (2002), Hydrothermal heat flux through aged oceanic crust: where does the heat escape?, *Earth Planet. Sci. Lett.*, *202*(1), 159–170, doi:10.1016/S0012-821X(02)00759-8.

Wang, K. L., J. H. He, and E. E. Davis (1997), Influence of basement topography on hydrothermal circulation in sediment-buried igneous oceanic crust, *Earth Planet. Sci. Lett.*, *146*(1-2), 151–164, doi:10.1016/S0012-821X(96)00213-0.

Wheat, C. G., and M. J. Mottl (2004), Geochemical fluxes through mid-ocean ridge flanks, in *Hydrogeology of the Oceanic Lithosphere*, edited by E. E. Davis and H. Elderfield, pp. 627–658, Cambridge University Press, Cambridge, UK.

Wheat, C. G., H. Elderfield, M. J. Mottl, and C. Monnins (2000), Chemical composition of basement fluids within an oceanic ridge flank: Implications for along-strike and across-strike hydrothermal circulation, *J. Geophys. Res.-Solid Earth*, *105*(B6), 13437–13447, doi:10.1029/2000JB900070.

Wheat, C. G., M. J. Mottl, A. T. Fisher, D. Kadko, E. E. Davis, and E. Baker (2004), Heat flow through a basaltic outcrop on a sedimented young ridge flank, *Geochem. Geophys. Geosystems*, *5*, Q12006, doi:10.1029/2004GC000700.

Wheat, C. G., S. M. Hulme, A. T. Fisher, B. N. Orcutt, and K. Becker (2013), Seawater recharge into oceanic crust: IODP Exp 327 Site U1363 Grizzly Bare Outcrop: seawater recharge into basaltic crust, *Geochem. Geophys. Geosystems*, *14*(6), 1957–1972, doi:10.1002/ggge.20131.

Winslow, D. M., A. T. Fisher, and K. Becker (2013), Characterizing borehole fluid flow and formation permeability in the ocean crust using linked analytic models and Markov chain Monte Carlo analysis: Borehole Flow and Formation Permeability, *Geochem. Geophys. Geosystems*, *14*(9), 3857–3874, doi:10.1002/ggge.20241.

Zyvoloski, G. A., B. A. Robinson, Z. V. Dash, S. Kelkar, H. S. Viswanathan, R. J. Pawar, and P. H. Stauffer (2011), Software Users Manual (UM) for the FEHM Application Version 3.1, *Los Alamos Natl. Lab.*, 265.

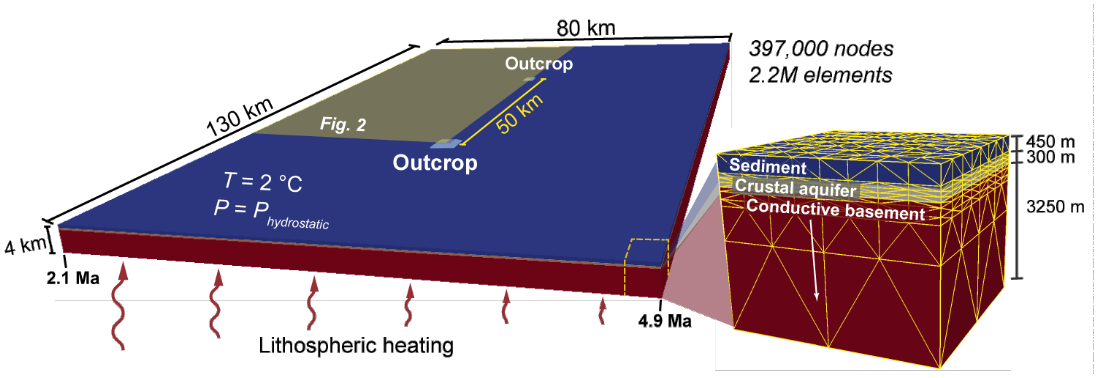

Fig. 2-1. Geometry and configuration of three-dimensional domains. Domains represent a section of upper ocean crust, oriented with the long-axis parallel to the spreading ridge, consistent with conditions at a field site on the eastern flank of the Juan de Fuca Ridge[*Wheat et al.*, 2000; *Fisher et al.*, 2003b; *Hutnak et al.*, 2006]. A conductive volcanic rock section (red, lower permeability) is overlain by a crustal aquifer (orange, higher permeability) and marine sediments (blue, lower permeability), and two volcanic rock outcrops penetrate through the sediment (light blue). Heat is applied to the base, following a lithospheric cooling trend (*1*). The sides and base are no-fluid flow boundaries, and the top is free flow (fluid and heat) with pressure varying as a function of seafloor depth. System properties are summarized in the Methods. Simulation results within the volume delineated with the yellow rectangle are shown in Fig. 2-2.

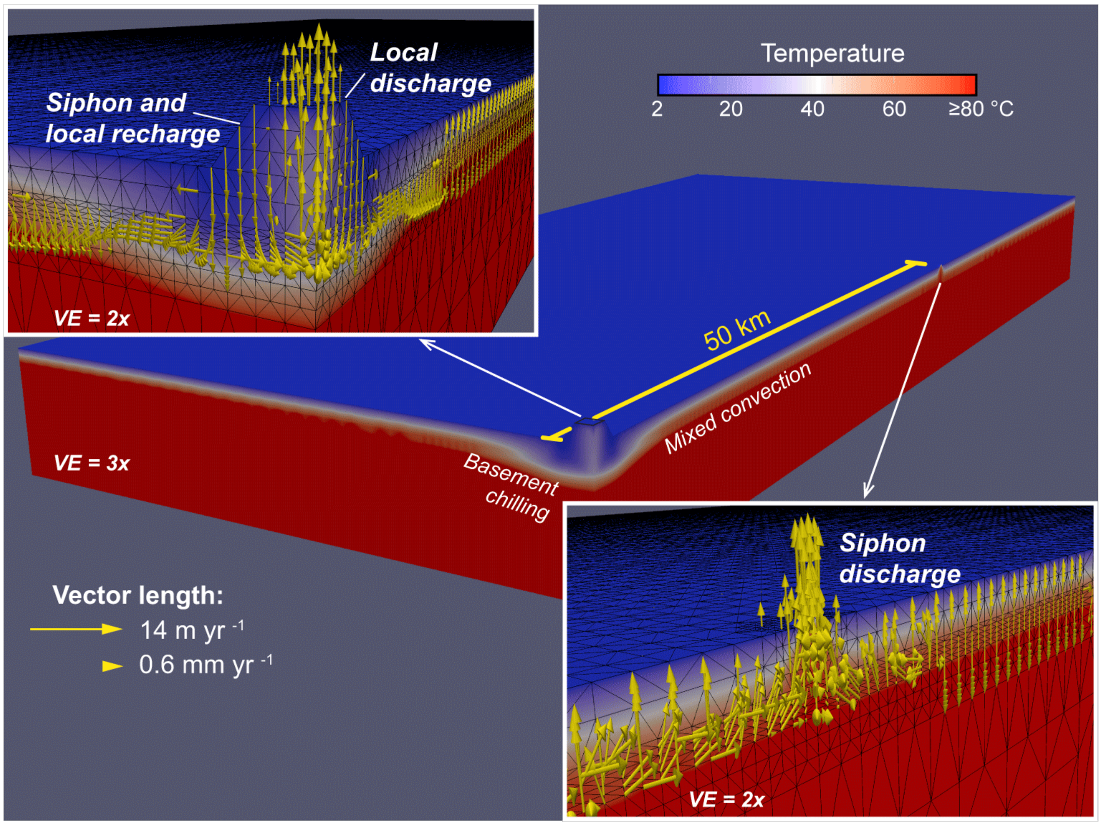

Fig. 2-2. Simulation results at dynamic steady state. This simulation, showing one quarter of the domain illustrated in Fig. 2-1, has one large outcrop and one small outcrop (characteristics defined in Table 2-1). Domain colors show domain temperatures, including influence of rolling/mixed convection in basement aquifer and thermal influence of recharging/discharging outcrops. Inset diagrams show fluid flow vectors within and around outcrops (length indicates flow rate), with vectors plotted on a natural-log scale, the longest vector (exiting the top of the discharging outcrop) corresponding to a flow rate of ~4.5 x 10^{-7} m s^{-1} (14 m yr^{-1}). Fluid flow through the sediment is so slow that it would generate no detectable thermal or geochemical anomalies. Vertical exaggeration (VE) of main image is 3x; VE of inset images is 2x.

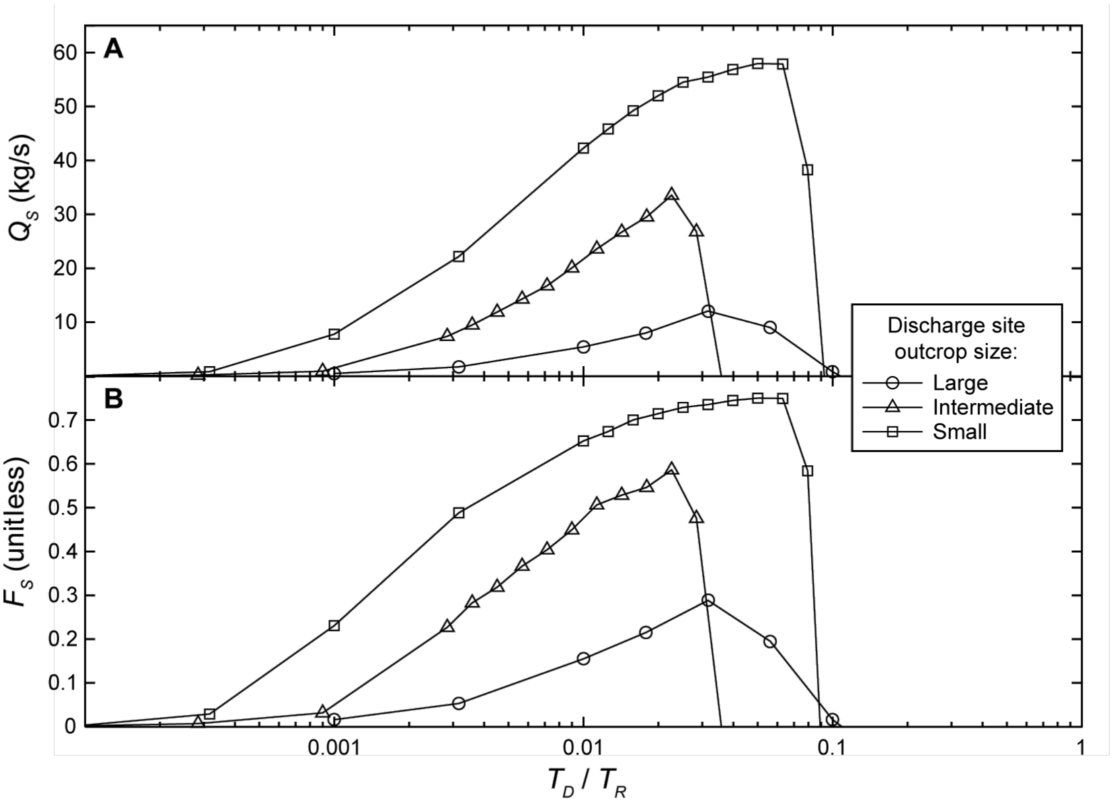

Fig. 2-3. Outcrop-to-outcrop siphon behavior for simulations having different outcrop sizes. (**A**) Siphon flow rate, Q_S. (**B**) Siphon fraction, F_S. Outcrop geometries defined in Table 2-1. Each point represents a simulation run to dynamic steady state. Crustal aquifer permeability is $k_{aq}=10^{-12}$ m^2 , and a large siphon-recharge outcrop (A=14.1 km^2) has permeability k_{oc} = 10^{-12} m^2, for all results shown. Permeabilities in the siphon-discharge outcrop differ for each simulation, as shown by the ratio of outcrop transmittance (T_D/T_R). Each geometry results in peaks for F_S and Q_S when $0.02 < T_D/T_R < 0.07$, and siphons fail to sustain when $T_D/T_R > 0.1$.

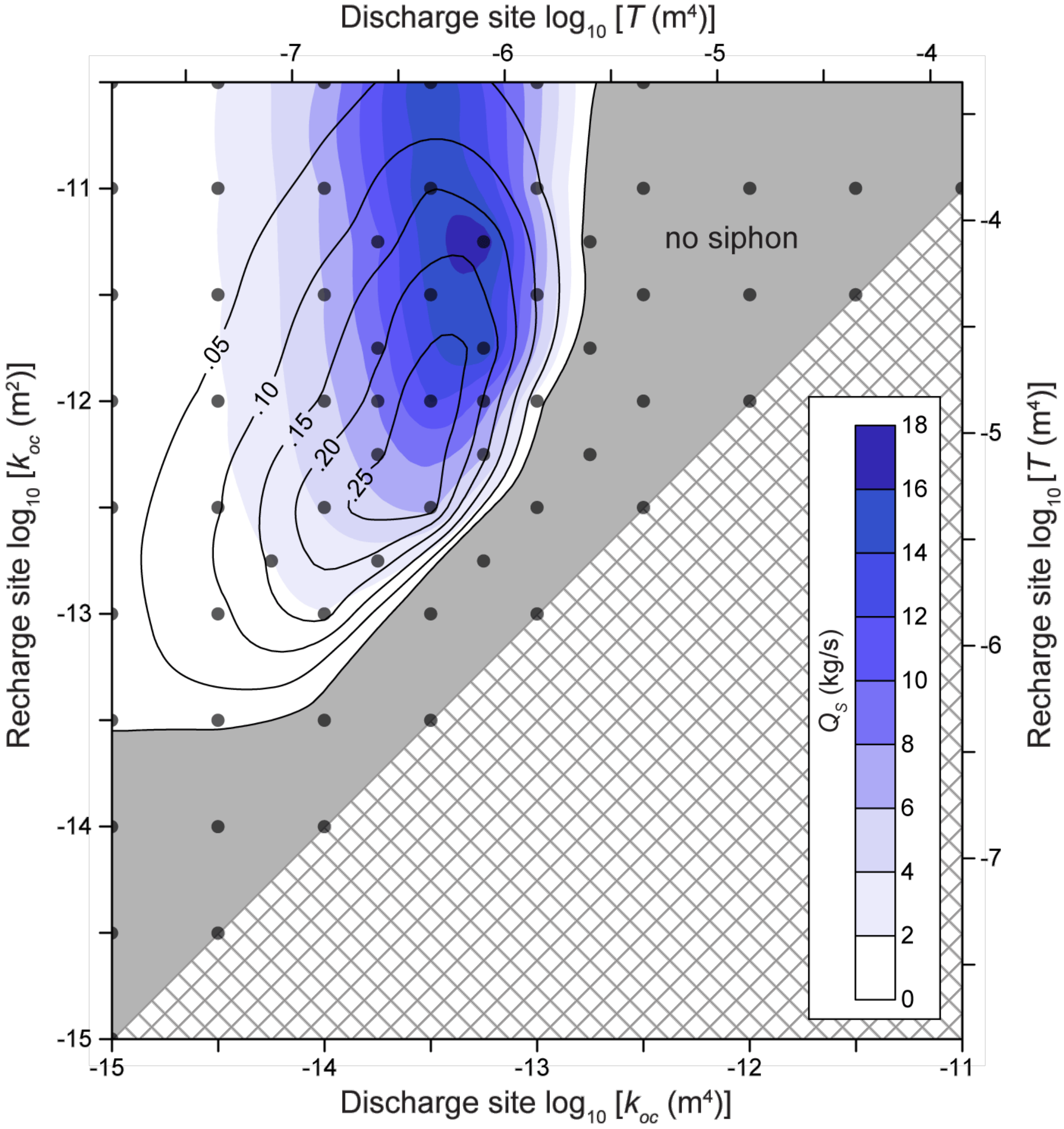

Fig. 2-4. Outcrop-to-outcrop siphon behavior for simulations with two large outcrops. Outcrop geometries are defined in Table 2-1. Bottom and left axes indicate outcrop permeability, whereas top and right axes show equivalent transmittance (permeability x outcrop area). Each circle represents results of a single simulation, run to dynamic steady state, delineating the permeability of recharge and discharge ends of the hydrothermal siphon. Color contours illustrate Q_S (siphon flow rate), whereas solid contour lines and labels delineate F_S (siphon fraction). Note offset between peak values of Q_S and F_S. Simulations within the grey zone did not sustain a hydrothermal siphon.

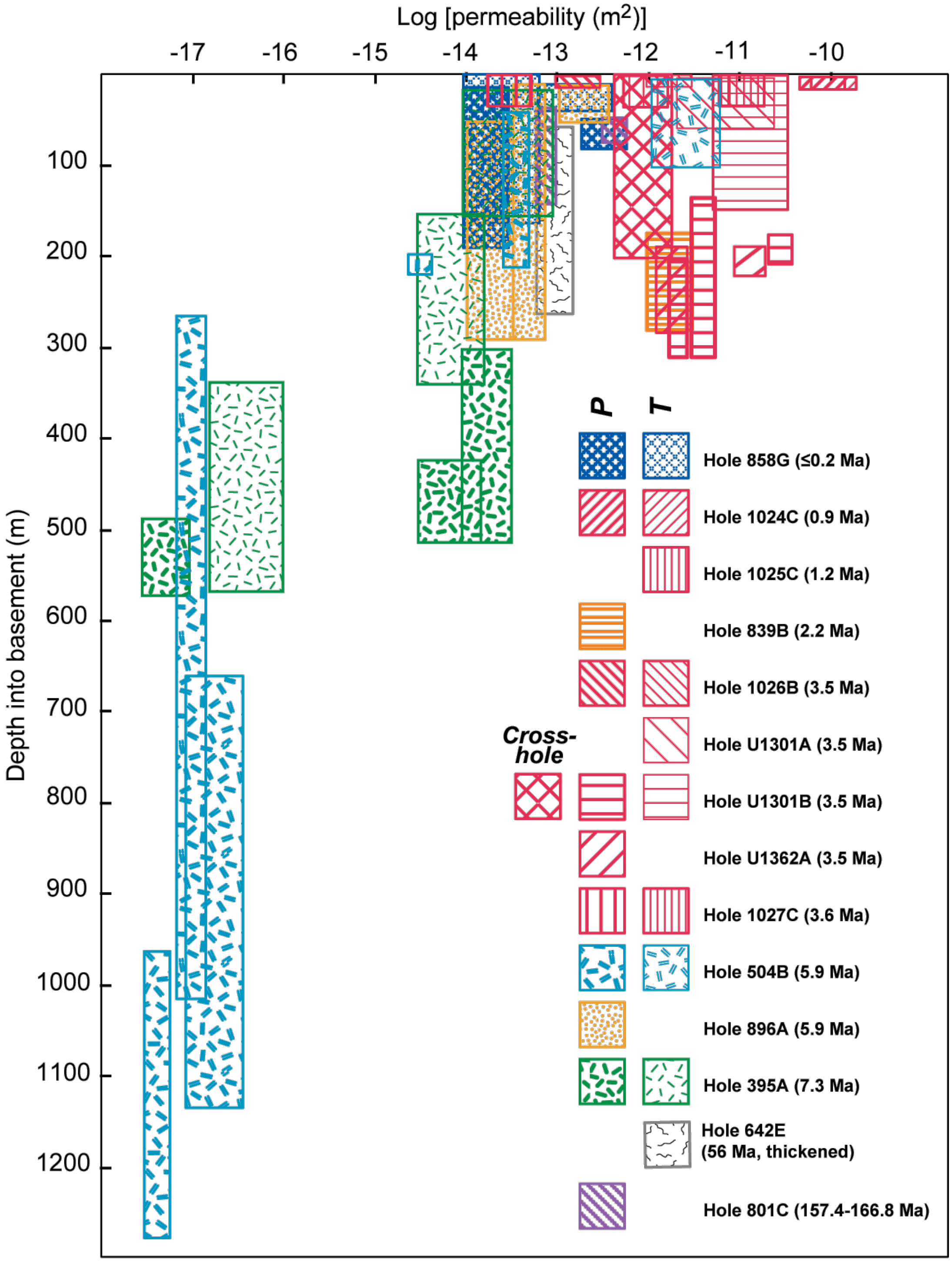

Fig. 2-5. Compilation of borehole measurements of permeability in the basaltic (volcanic) ocean crust. Figure modified from ref ([*Fisher et al.*, 2014]). Data in this compilation are from packer experiments[*Becker et al.*, 2013] (*P*), modeling of borehole thermal logs[*Winslow et al.*, 2013] (*T*), and a single cross-hole response experiment[*Fisher et al.*, 2008], as labeled.

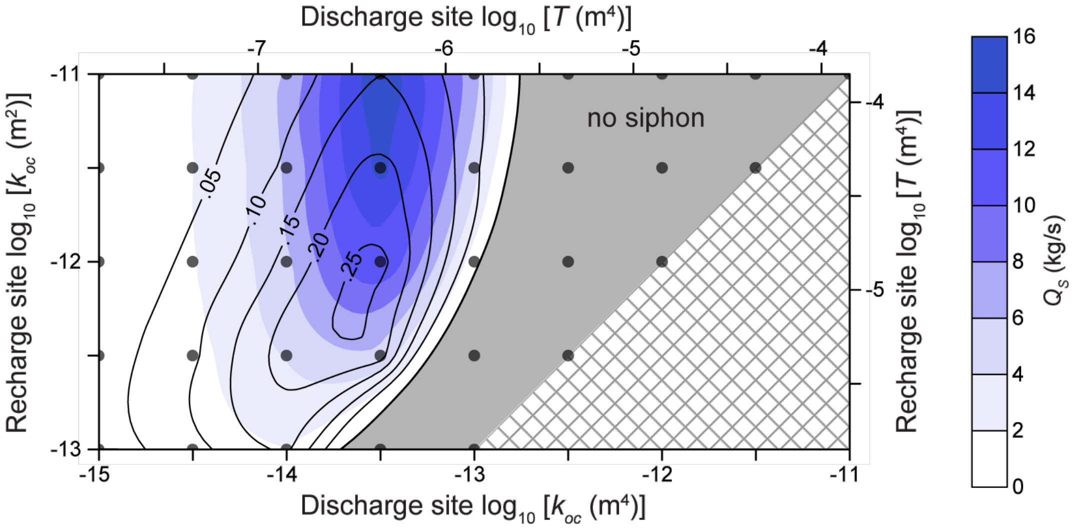

Fig. 2-6. Outcrop-to-outcrop siphon behavior for "conductive hydrostatic" simulations with two large outcrops. Simulations are as shown in Fig. 2-4, but started from a "conductive-hydrostatic" initial conditions rather than a running siphon. Each circle represents results of a single simulation, run to dynamic steady state, delineating the permeability of recharge and discharge ends of the hydrothermal siphon. Solid contour lines and labels delineate F_S; filled color contours illustrate Q_S.

Table 2-1. Volcanic rock outcrop characteristics used in coupled-flow simulations.

	Exposure area [a] A (km^2)	Height [b] (m)	Top width [c] (km)	Base width [c] (km)
Small	0.141	65	0.25	1.0
Intermediate	1.27	200	0.50	2.0
Large	14.1	500	2.0	4.5

[a] Map-view cross-sectional area of outcrop exposed at the seafloor.

[b] Outcrop height above the seafloor.

[c] Top and base widths are measured side to side, with base width measured at the sediment-basement interface. Outcrop edifices are simulated as ziggurats (flat-topped pyramids).

Table 2-2. Formation properties used in coupled-flow simulations.

	Porosity, n (unitless)	Thermal conductivity, λ (W/m·K)	Permeability, k (m^2)
Sediment [a]	0.39 to 0.52	1.36 to 1.51	1.1×10^{-17} to 2.2×10^{-17}
Outcrop [b,c]	0.1	1.82	1×10^{-15} to 3.2×10^{-11}
Aquifer [b]	0.1	1.82	10^{-12}
Deep crust [b]	0.05	1.93	10^{-18}

[a] Values vary with depth, are consistent through all simulations. The relatively narrow range of sediment permeabilities applies to the full sediment column, representing a range at a smaller scale of several orders of magnitude.

[b] Values assigned homogeneously throughout each region.

[c] Each outcrop is assigned a single value in a given simulation. Range refers to values assigned across all simulations.

Chapter Three

THREE-DIMENSIONAL MODELING OF OUTCROP-TO-OUTCROP HYDROTHERMAL CIRCULATION ON THE EASTERN FLANK OF THE JUAN DE FUCA RIDGE

Abstract

We present results of three-dimensional coupled simulations (fluid, heat) simulations of ridge-flank hydrothermal circulation on the eastern flank of the Juan de Fuca Ridge, where field studies have demonstrated fluid flow between two seamounts separated by ~50 km. Constraints from field observations include a range of possible flow rates between the outcrops, secondary convection adjacent to the recharging outcrop, determinations of crustal permeability from borehole measurements, and the lack of a regional seafloor heat flux anomaly as a consequence of outcrop-to-outcrop circulation. New simulations include an assessment of crustal permeability and thickness, outcrop permeability, permeability anisotropy in the crust, the potential impact of additional discharging outcrops, and a comparison with results from two-dimensional simulations. Three-dimensional simulations are most consistent with field observations with crustal permeability of 3×10^{-13} to 2×10^{-12} m^2, within a crustal aquifer that is ≤300 m thick, values consistent with borehole observations. In addition, we find fluid flow rates and crustal cooling efficiencies that are an order of magnitude greater in three-dimensional simulations than inferred from two-dimensional simulations using equivalent properties.

3.1 Introduction

3.1.1 Background and motivation

Ridge-flank hydrothermal systems drive substantial flows through the oceanic crust on a global basis. These systems, which operate at lower temperatures and in older ocean crust than that found near ridges, extend over a large fraction of the seafloor. In global aggregate, ridge flank systems are responsible for ≥70% of advective heat extraction from the oceanic crust [*Stein and Stein*, 1992, 1994], and mediate significant solute fluxes between the crust and the ocean [*de Villiers and Nelson*, 1999; *Wheat and Mottl*, 2004; *Fisher and Wheat*, 2010]. These flows also influence the structure and development of the crust, and support a vast and diverse biosphere within the sediments and upper ocean crust [*Cowen et al.*, 2003; *Edwards et al.*, 2005].

Coverage of thick and relatively impermeable sediment is pervasive across much of the ridge-flank environment. Seamounts and volcanic edifices (outcrops) exposed at the seafloor can allow fluids to bypass sediments, providing relatively high permeability conduits for fluid exchange between the ocean and underlying crustal aquifer [*Fisher and Becker*, 2000; *Villinger et al.*, 2002; *Fisher et al.*, 2003b]. Systems that develop sustained subsurface flow between sets of outcrops are referred to as outcrop-to-outcrop hydrothermal siphons, and are capable of driving flows through the ocean crust that significantly impact lithospheric heat extraction [*Fisher et al.*, 2003a; *Hutnak et al.*, 2008; *Anderson et al.*, 2012]. This type of flow is driven by differences in pressure between cool (recharging) and warm (discharging) columns of water within each outcrop [*Fisher and Becker*, 2000; *Fisher et al.*, 2003b; *Winslow and Fisher*, 2015]. With sufficiently high permeability in the outcrops and intervening aquifer, these differential pressures can drive significant fluid, heat, and solute fluxes through the ocean crust.

Seamounts and volcanic edifices (outcrops) are ubiquitous throughout the seafloor [*Kim and Wessel*, 2011], as are fracture zones, transform faults, and other regions of basement exposure, allowing flows capable of extracting significant lithospheric heat on a global basis. Given the number of seamounts globally, pairs of outcrops have a typical spacing that should allow for a large number of hydrothermal siphons to operate [*Anderson et al.*, 2012]. These systems may also be more significant to the lithospheric heat budget than previously estimated since small outcrops, which are underrepresented in gravity studies [*Kim and Wessel*, 2011], tend to be sites of discharge [*Fisher et al.*, 2003b; *Davis and Becker*, 2004; *Hutnak et al.*, 2008] and may play a more important role in regional heat extraction than their larger counterparts [*Winslow and Fisher*, 2015].

We focus on a well-studied outcrop-to-outcrop hydrothermal siphon operating on the eastern flank of the Juan de Fuca Ridge. We present a series of parametric studies, each comprising of a number of three-dimensional coupled-flow simulations designed to elucidate the nature of heat and fluid flow within the system, and to constrain system hydrologic properties in the context of field observations. A subset of simulations contrasts two-dimensional modeling, which has been applied to systems of this kind in the past [*Hutnak et al.*, 2006], with three-dimensional modeling to examine the importance of dimensionality in accurately representing system properties and behavior. We also assess the potential influence of additional factors (discharge through additional outcrops, azimuthal permeability anisotropy) on the patterns of heat and fluid flow, and on our estimates of hydrologic properties.

3.1.2 Field site and observations

3.1.2.1 Characterization of field site

Our field site is located 100 km east of the Juan de Fuca Ridge, an intermediate-rate spreading center. Despite being relatively young (3.5-3.6 Ma) crust, a thick layer of sediment (~450 m) has accumulated due to high sedimentation rates (30-50 cm/ky) and the trapping of turbidites by abyssal hill topography [*Underwood et al.*, 2005]. The field site is located over a basement topographic high, where a number of volcanic outcrops breach the sediments [*Davis et al.*, 1992]. Two outcrops, Baby Bare and Grizzly Bare, support an active hydrothermal siphon that drives fluids through the 50 km of crust between them [*Fisher et al.*, 2003b; *Hutnak et al.*, 2006; *Winslow and Fisher*, 2015]. These outcrops were most likely formed through off-axis volcanism through processes distinct from those governing the initial formation of the crust [*Karsten et al.*, 1998; *Becker et al.*, 2000], implying that hydrologic properties in each outcrop may differ from those of the nearby crust. The Baby Bare and Grizzly Bare outcrops are relatively isolated from the others in the region (Fig. 3-1), and the hydrothermal siphon between them flows from south to north [*Wheat et al.*, 2000].

Additional outcrops, Mama Bare and Papa Bare, are located 16 and 20 km to the north of Baby Bare, respectively.

The high-permeability crustal aquifer is one or more layers of extrusive basalt that may extend hundreds of meters beneath the sediments, though this thickness (and associated depth extent of circulation) is not well known. In-situ bulk permeability measurements at the study site, completed with borehole (packer) testing [*Becker et al.*, 2013] and from modeling of thermal logs in flowing boreholes [*Fisher*, 1998; *Winslow et al.*, 2013], indicate bulk permeability in the upper 300 m of basaltic crust of 10^{-12} to 10^{-11} m^2. Although no boreholes deeper than 300 m have been drilled near this site, deeper holes drilled elsewhere in the ocean crust show a significant decrease in permeability in ocean crust deeper than 600 m [*Anderson and Zoback*, 1982; *Becker et al.*, 1983], which provides an upper bound on the possible range of aquifer thickness.

Hydrothermal circulation in this system may have been more vigorous in the past, but rapid sedimentation has diminished hydrothermal activity by thickening sediment cover and burying many former outcrops. A number of heat-flow surveys have been performed throughout the region (Fig. 3-1), and show heat flow that is somewhat lower than predicted by lithospheric cooling models [*Stein and Stein*, 1992], indicating a regional deficit of ~15%. This deficit can be fully accounted for by thermal rebound in the crust [*Hutnak and Fisher*, 2007], a process by which the crust returns to equilibrium over up to millions of years following to the rapid burial of a site. This effect is distinct from that of current hydrothermal circulation, discussed at length in this study, which has no measurable influence on regional heat-flux at the seafloor [*Hutnak et al.*, 2006]. There are local seafloor heat flux anomalies on and near the two outcrops forming the recharge and discharge sites for the hydrothermal siphon, but these are restricted to within a few kilometers of the edge of basement exposure.

3.1.2.2 Siphon observations

The existence of the hydrothermal siphon operating between Grizzly Bare and Baby Bare outcrops has been established through multiple lines of evidence. Heat flow surveys local to Grizzly Bare show reduced heat-flow and cool upper-aquifer temperatures: 80 to 100 mW/m^2 and ~5 °C, compared to background values of 175 to 185 mW/m^2 and 60 to 65 °C at >1 km from the outcrop edge [*Hutnak et al.*, 2006]. This indicates the recharge of cool bottom-water fluids through the outcrop. Similarly, heat-flow measured near Baby Bare is elevated (> 800 mW), consistent with the discharge of warm crustal fluids [*Becker et al.*, 2000; *Wheat et al.*, 2004; *Hutnak et al.*, 2006]. Fluid chemistry from water column samples and sediment cores near and between the outcrops establishes hydrologic connectivity between the outcrops, as fluids show a clear pattern of increasing alteration along a south-to-north transect between the outcrops [*Wheat and Mottl*, 2000; *Wheat et al.*, 2000]. Finally, fluid chemistry in pore and spring waters from Baby Bare is distinct from that of bottom-water samples, and consistent with increased alteration and water age [*Mottl et al.*, 1998; *Wheat and Mottl*, 2000], and with the composition of fluid samples collected from nearby boreholes (e.g., *Wheat et al.*, 2003, 2010). An analysis of water age based on ^{14}C in upper-basement fluids indicate a travel time of 4 to 10 ky [*Elderfield et al.*, 1999; *Walker et al.*, 2007], though dispersive corrections could significantly reduce this estimate (corrections by a factor of 10 to 100 are common in fractured rock systems) [*Fisher et al.*, 2003b; *Stein and Fisher*, 2003].

Thermal studies of the warm plume above the Baby Bare outcrop provide estimates of the discharge rate (5-20 L/s) [*Thomson et al.*, 1995; *Mottl et al.*, 1998; *Wheat et al.*, 2004]. Fluid flow rates may be somewhat higher than this, considering the difficulties in estimating heat and fluid fluxes from the water column, and that extrapolating diffuse flow over the outcrop would tend to bias estimates towards lower rates if sites of focused flow were missed. Given the relative impermeability of regional sediments and that heat-flow surveys show no indication of recharge through either the sediment column or at Baby Bare, the fluids discharged from Baby Bare must be recharged at Grizzly Bare. While Baby Bare appears to act strictly as a site of discharge, subseafloor thermal measurements show evidence for outcrop-local discharge at Grizzly Bare in addition to recharge [*Wheat et al.*, 2013], which suggests a complex and three-dimensional character to fluid flow within the outcrop, in addition to flow associated with the hydrothermal siphon. Heat-flow observations around Grizzly Bare seamount show no evidence for localized heat-flow suppression beyond the 2-3 km from the edge of basement exposure [*Hutnak et al.*, 2006], which indicates minimal regional heat loss due to current hydrothermal circulation.

In context of the global average for heat-flow suppression, this site represents a low-flow end-member. Outcrop-to-outcrop hydrothermal circulation in general must be more efficient at extracting lithospheric heat [*Fisher and Becker*, 2000; *Villinger et al.*, 2002; *Anderson et al.*, 2012], in keeping with observed suppression of seafloor heat flow [*Stein and Stein*, 1992, 1994]. These observations characterize the system as operating within a narrow range of conditions: driving forces and fluid flow are capable of sustaining an outcrop-to-outcrop hydrothermal siphon across 50 km of crust, yet are insufficient to affect regional heat-flow. These conditions place particularly strong constraints on system hydrologic properties related to fundamental crustal construction and evolution.

3.2 Methods

3.2.1 Model and configuration

All simulations for this study were performed with Finite Element Heat and Mass (FEHM). FEHM is a node-centered hydrocode, developed at Los Alamos National Laboratory [*Zyvoloski et al.*, 2011], which uses a finite-volume approach to represent properties and solve for coupled and transient heat and fluid flow. The model domain in each simulation is represented by a Delaunay mesh of tetrahedral elements. For this study, we used a fully implicit solver with upstream weighting.

The region surrounding individual nodes, referred to as model cells, comprise representative elemental volumes in which the application of bulk properties characterizes both solid material and pore space. Physical properties are assigned homogenously as a single value within each section of basaltic crust (the crustal aquifer, low permeability deep crust, and each outcrop region). Unless otherwise specified, crustal properties are also assigned isotropically. Properties for the sediment layer (porosity, thermal conductivity, and permeability) vary with depth to account for compaction. Representative depth-dependent functions are created for each property, then discretized and assigned to nodes such that the cumulative effects of the sediment layer are consistent with field data. A summary of physical property assignments for all simulations is presented in Table 3-1.

Simulations were run for 10^5 to 10^6 years of simulation time (1,000 to 2000 time steps) over runtimes of 1 to 10 days on a desktop (Linux) workstation. This was sufficient in each case to achieve a dynamic steady state, wherein transient behaviors persisted (e.g. mixed convection, unstable secondary convection, local circulation) while recharge and discharge rates through outcrops stabilized to ± 0.1% per kyr of simulation time. Internal mass balance errors reported by FEHM and calculated during solution iteration are <<1%. Mass and energy conservation were confirmed for three dimensional models on the basis of bulk flows, finding apparent imbalances for single time steps to be <3% for simulations at dynamic steady state. These levels are expected, as flows continue to be irregular and oscillatory and significant fluid moves into and out of storage throughout the crustal system (>4 x 10^4 km^3).

All simulations presented begin with the initial temperature and pressure conditions for an active outcrop-to-outcrop hydrothermal siphon, consistent with field observations. This initial state is obtained by first running a heat-flow only simulation that generates a state (temperature and pressure) consistent with the geometry and physical properties of the domain. This state is used to initialize a fully coupled simulation with aquifer and outcrop properties chosen to allow the spontaneous formation of an outcrop-to-outcrop hydrothermal siphon. The resulting state, characterized by a flowing hydrothermal siphon, is used as a consistent starting condition for all subsequent simulations of the same crustal geometry. Though a number of alternate initial conditions are possible, results from three-dimensional simulations of systems with similar properties and geometry to those found at our field site have been shown to be relatively insensitive to initial conditions [*Winslow and Fisher*, 2015].

3.2.2 Model domain

Model grids are designed to represent the geometry, scale, and properties relevant to the outcrop-to-outcrop hydrothermal siphon system at the Juan de Fuca field site (Fig. 3-2). This includes the Grizzly Bare and Baby Bare outcrops, spaced 50 km apart, and an outer section of the crust that places domain boundaries 40 km from each outcrop center. The total model domain represents a 4 km thick section of the ocean crust, 130 km x 80 km in spatial extent, and is aligned with the long-edge parallel to the ridge axis. We refer to the alignment of Grizzly Bare and Baby Bare in this study as "south-north" and the perpendicular direction as "east-west" as a shorthand, though Baby Bare is in fact oriented N 20° E from Grizzly Bare.

The size of the domain was chosen to provide a large gap between the outcrops and the boundaries of the model domain. This approach is intended to minimize the influence of the side-boundaries on the shape and character of the flow field between the Grizzly Bare and Baby Bare outcrops, without intending to explicitly represent features of the field site that fall within this outer region. The vertical structure of the crust is represented by a series of flat tabular layers, excepting the sediment and crustal sections associated with outcrop slopes. The sediment layer (450 m) sits atop a permeable crustal aquifer (100-600 m, varies by simulation), with a relatively impermeable underlying crustal layer (3 km). This lower layer supports little fluid flow but is important to the energy balance near outcrops, whose thermal influence can conductively propagate deep into the crust, bending isotherms well below the active aquifer. Models run with a thinner conductive layer can bias the result by limiting redistribution of lithospheric heat associated with vigorous fluid circulation.

The sides and bottom of the domain are closed to fluid flow, with time-constant and depth-dependent hydrostatic pressure applied at the top. The side boundaries are also no-flow and adiabatic, and a constant-temperature boundary consistent with bottom-water temperatures (2 °C) [*Davis et al.*, 1992; *Fisher et al.*, 2003b; *Hutnak et al.*, 2006] is applied to the top of the model domain. Basal heat input is specified as a function of crustal age, calculated based on a lithospheric cooling curve [*Stein and Stein*, 1992], and has significant variability due to the regional scale of the model domain. Heat input across the model is corrected to account for the 15% reduction in heat-flow associated with thermal rebound in the region [*Hutnak and Fisher*, 2007], a process that is not explicitly modeled as part of this study.

3.2.3 Metrics and observational constraints

Field observations provide insight into the operation of the outcrop-to-outcrop hydrothermal siphon at the study site, and allow us to construct criteria to distinguish the simulations that emulate observed behaviors from those that do not. Specifically, for a simulation to be considered consistent with observational constraints, it must (1) sustain a hydrothermal siphon operating south-to-north, with siphon-discharge at Baby Bare in the north and siphon-recharge at Grizzly Bare in the south, (2) support siphon-flow rates of 5-20 kg/s, and (3) have no significant local or regional flow suppression outside the immediate influence of the outcrops. Later in this study, we discuss the implications of relaxing these constraints, particularly the second one, as the total flow rate supported by the siphon might be underestimated. Simulations should also feature outcrop-local discharge in the southern outcrop in addition to the recharge associated with siphon flow, as inferred from subseafloor thermal measurements at Grizzly Bare [*Wheat et al.*, 2013].

Siphon flow (Q_S) for each simulation is calculated by subtracting simulated recharge from discharge at Baby Bare, though recharge through this feature is typically very small (< 1 kg/s). As recharge in each simulation occurs primarily through the outcrops, any discharge in excess of outcrop-local recharge must be recharged at the Grizzly Bare outcrop. A tiny fraction of outcrop discharge could originate as slow infiltration through overlying sediments, but this process must occur at a rate that is undetectable with geochemical and thermal analyses (e.g., <0.1 mm/y). The siphon fraction (F_S), defined as the ratio of Q_S to the total simulated discharge from outcrops, is used to quantify the relative significance of the hydrothermal siphon versus discharge supported by outcrop-local circulation. When $F_S < 1$, outcrop-local circulation is present in one or both outcrops, in addition to recharge and discharge associated with the hydrothermal siphon.

The heat-suppression fraction (F_H) is used to quantify the extent to which regional seafloor heat flux is reduced below the lithospheric input at the base of the simulation domain. We define F_H as the area-fraction of the model domain that has >10 mW of heat-flow suppression when compared against a comparable simulation with no fluid flow. This threshold, equivalent to ~5% of lithospheric heat input at the base of the domain, represents a significant and measurable deviation. The conductive heat flux is assessed through sediment surrounding volcanic outcrops, but not through the outcrops themselves, because (1) field observations are restricted to locations where there is sediment cover, and (2) resolving conductive heat flux through outcrops would require fine grid spacing and very small time steps to accommodate rapid rates of fluid transport. In addition, the heat-flow anomaly extending out to 2 km from the edge of each outcrop was excluded when assessing the regional seafloor heat flux deficit, because areas closer to outcrops are subject to local conductive anomalies [*Hutnak et al.*, 2006]. We generally consider simulations with $F_H > 0.05$ to be inconsistent with observations, as the extensive heat flux studies at the field site (Fig. 3-1) would have resolved anomalies associated with hydrothermal circulation over a significant fraction of the region.

3.2.4 Parametric studies

The next three sections report results from a series of parametric tests. In each parametric set, one or more properties are varied over multiple simulations in order to explore the parameter-space that produces simulations consistent with observational constraints. A number of properties that are not well determined on the basis of field observations (e.g., upper crustal aquifer thickness, permeability of basaltic crust in either outcrop) appear to significantly influence the operation of simulated hydrothermal siphons. This allows the values of each property to be assessed on the basis of simulated siphon behavior.

Each simulation in this study is assigned a single set of time-constant properties. A series of such simulations, each with distinct values for the properties in question, constitutes a parametric set used to investigate the influence of these properties on system behavior. A summary of each parametric set, and the associated property ranges tested in each, is presented in Table 3-2. The first sets (AQTEST, OCTEST) deal with the geometry and permeability within crustal rocks, and aim to constrain estimates for these properties on the basis of model output and observational data. Later parametric sets investigate additional influences beyond bulk property assignment, including the possibility of additional fluid discharge to the north of the modeled domain (through other outcrops, ADDQTEST), azimuthal anisotropy in permeability (ANITEST), and the influence of running simulations in two or three dimensions (2DTEST), including comparison with separate modeling studies [*Hutnak et al.*, 2006; *Anderson et al.*, 2012]. In each case, a subset of properties from ranges established in earlier sections is used, rather than testing the full range of possible properties, in order to focus on specific parameters of interest.

3.3 Modeling constraints on crustal properties and flow geometry

3.3.1 Flow patterns in coupled-flow simulations

For all simulations presented with active hydrothermal siphons, fluid recharges at Grizzly Bare and flows northward through the upper crustal aquifer until discharging at Baby Bare (Fig. 3-3). The direction of flow between outcrops is controlled by the size and permeability of the outcrops [*Winslow and Fisher*, 2015] and is strongly favored from Grizzly Bare to Baby Bare at this field site, with all simulations with active siphons also featuring flow in this direction. Even simulations that were started with flow in the other directions spontaneously flipped such that siphon recharge occurred through Grizzly Bare and discharge occurred through Baby Bare.

Mixed convection is also typically present within the aquifer between the outcrops and similar secondary flow can occur within the outcrops; most simulations include significant outcrop-local discharge at Grizzly Bare. Simulations typically include a temperature difference of ~60 °C between recharging fluids at Grizzly Bare and discharging fluids at Baby Bare, with differential pressure in the crustal aquifer between the two outcrops of 20-100 kPa. These conditions typically generate lateral linear flow rates (specific discharge) of 0.2 to 0.9 m/y within the aquifer, indicating an outcrop-to-outcrop travel time of 5 to 25 ky assuming a 10% effective porosity, or 0.5 to 2.5 ky assuming a 1% effective porosity. Specific discharge from the outcrops (including vertical flow) is somewhat higher (6 to 10 m/y), and low enough in the sediments (<0.1 mm/y) to be undetectable by thermal or geochemical methods. The highest flow rates in each simulation are associated with discharge at Baby Bare, even when k_B is significantly lower than permeability elsewhere in the model (as in OCTEST).

Overall lateral flow within the hydrothermal siphon is generally consistent with that of a dipole, causing recharging fluid at Grizzly Bare to travel along both direct and indirect paths to Baby Bare. The lateral flow pattern within the aquifer and outcrops in a typical simulation is shown in Fig. 3-4. While the largest flows follow relatively direct paths between the outcrops, a fraction of fluid travels on sweeping paths around and behind the outcrops. The character of the thermal pattern and velocity field within each outcrop reflects this, with active hydrothermal circulation occurring throughout both outcrops. The distribution and relative importance of specific flow-paths will ultimately depend on the nature of the permeability network present in the field, and is highly idealized in these simulations, but the possibility for fluids to take both direct and indirect paths appears to be a significant feature of these systems.

3.3.2 Siphon dependence on aquifer and outcrop properties

One parametric set of simulations (AQTEST) is designed to estimate the permeability and thickness of the upper crustal aquifer (k_A and b, respectively). In order to study the combined affects of both properties on the behavior of the hydrothermal siphon, we prepared four separate model grids with different aquifer thicknesses (100 to 600 m, Table 3-2) and completed simulations with each over a range of permeability values. Outcrop permeability was assigned a moderate value of 10^{-12} m^2 for all simulations; the impact of outcrop permeability is investigated later with OCTEST simulations. Hydrothermal siphon behavior for each simulation is summarized in Fig. 3-5 in terms of three metrics defined earlier: siphon discharge (Q_S), the fraction of regional heat flow suppression (F_H), and the fraction of outcrop discharge that is associated with the siphon (F_S).

All AQTEST simulations that sustain a hydrothermal siphon do so with Q_S at or above observed flow rates (5 to 20 kg/s). While most simulations produce flow rates of 25 to 150 kg/s, results for a small number of simulations with $b \leq 300$ m have flow rates within the range constrained by observations (15 to 20 kg/s). All simulations run with $b \leq 300$ m also showed minimal regional heat-flow suppression ($F_H < 0.05$), while all simulations with $b = 600$ m exceeded this threshold. These higher values of F_H result from a thicker aquifer generating a larger temperature difference between the upward and downward limbs of local convection cells when $k_A = 10^{-13}$ to 10^{-12} m^2. With this range of properties, the convective pattern influences seafloor heat flow in ways inconsistent with field observations. The shape of response for Q_S as a function of k_A is similar for each aquifer geometry, but the curves are shifted laterally (Fig. 3-5A). It is notable that the change in k_A required to sustain a siphon is not proportional to the difference in b, as would be expected if transmissivity (aquifer hydraulic conductivity times layer thickness) were the only control: a 100 m aquifer is 1/6 as thick as a 600 m aquifer, yet requires a tenfold increase in k_A to produce similar Q_S. This suggests that aquifer thickness influences the efficiency of heat extraction in two ways, affecting both transmissivity and the depth of circulation.

The next parametric set (OCTEST) focuses on the influence of permeability within the Grizzly Bare outcrop (k_G) and the Baby Bare outcrop (k_B). We use a 300 m aquifer in all simulations, and vary the properties of each outcrop separately (keeping

k_G fixed at 10^{-12} m^2 while varying k_B, and vice versa). Three values of k_A are tested to assess the sensitivity of results to aquifer properties. Results for simulations testing the influence of k_G and k_B are summarized in Fig. 3-6.

All OCTEST simulations have Q_S within or above siphon flow rates estimated from field observations (5-20 kg/s), with a small number of simulations with low k_B (1-3 × 10^{-13} m^2) falling within this range. All simulations except two also have $F_H < 0.05$, with those above being the most extreme examples in terms of Q_S, k_A, and k_B (Fig. 3-6B). Within the ranges tested, an increase in permeability results in monotonic increases in both Q_S and F_H, with fluid flow rate being more sensitive to k_B than to k_A or k_G. Higher k_B also leads to higher F_S, while k_G has the inverse effect on F_S (Fig. 3-6C). This difference is largely due to the size contrast between Grizzly Bare and Baby Bare; Grizzly Bare is better able to support secondary convection and simultaneous recharge and discharge, whereas the small surface area of Baby Bare restricts the outcrop to discharge only in these simulations. Changes in k_B only affect discharge, with Baby Bare acting solely as a discharge site in all OCTEST simulations, but increases in k_G amplify both recharge and discharge at the outcrop and act to increase outcrop-local circulation more than Q_S (driving down F_S).

3.3.3 Discussion of permeability and aquifer thickness

AQTEST simulation results show distinct behavior that varies with aquifer thickness (b), but the shape and magnitude of both Q_S and F_S as a function of k_A are similar for each value of aquifer thickness (Fig. 3-5A, C). While variations in b shift these curves by up to an order of magnitude in k_A, the similarity of the $Q_S(b)$ response makes it difficult to constrain the aquifer's thickness on the basis of these results alone. Borehole logs and results from packer testing show evidence for high permeability to a depth of 300 m into the crust, but also suggest that the upper extrusive ocean crust may comprise a series of thin, highly permeable units [*Becker et al.*, 2013]. While we did not explicitly model separate zones within a single aquifer, the fact that a number of simulations involving thin aquifers (100 m, 200 m) resulted in active hydrothermal siphons and were consistent with the field constraints demonstrates that thin zones are capable of supporting significant flows without violating field constraints. Results from the ensemble of AQTEST simulations suggest that the best match for aquifer thickness in this setting is $b < 600$ m, considering how well simulations with thin aquifers match constraints, and that all simulations with $b = 600$ m had seafloor heat-flux suppression well in excess of what is observed regionally (Fig. 3-5B).

AQTEST simulations that result in active hydrothermal siphons (including those with large Q_S and/or F_H) span three orders of magnitude in k_A (10^{-13} to 10^{-10} m^2). The span of permeability for simulations within observational constraints (Q_S from 5 to 20 kg/s, $F_H < 0.05$) is significantly narrower (<1 order of magnitude), with k_A ranging from $3{\times}10^{-13}$ to 2×10^{-12} m^2. Both ranges are consistent with estimates of permeability from packer testing and borehole thermal logs from boreholes in the region [*Becker et al.*, 2013; *Winslow et al.*, 2013], and bracket the value derived from a single cross-hole test [*Fisher et al.*, 2008]. These calculations result in lower values of permeability than those inferred from earlier two-dimensional modeling of the same system [*Hutnak et al.*, 2006]; a more extensive comparison between two- and three-dimensional modeling results is presented later.

The hydraulic properties of basaltic rock outcrops on the seafloor are not well constrained by field data and, given complexities of drilling in bare rock settings, the rarity of field constraints on outcrop properties is likely to persist into the near future. However, modeling results, particularly those from OCTEST simulations, provide insight into permeability at the recharging and discharging end of this hydrothermal siphon (k_G and k_B). Simulations that have both high k_A and high outcrop permeability ($\geq 10^{-12}$ m^2) result in significantly greater Q_S than have been inferred independently from field observations. This suggests that, while permeability $\geq 10^{-12}$ m^2 is physically possible in a hydrothermal siphon running at the scale of this system, elevated permeability both within the crust and within outcrops makes it more difficult to meet field constraints.

That both Q_S and F_H are more sensitive to changes in k_B than in k_G appears to be significant, and suggests that siphon behavior has greater dependence on properties near the site of discharge. The "discharge-dominated" nature of this system results from temperature being a primary control on driving forces that sustain the siphon. Since recharging fluids enter at a fixed temperature (that of bottom water, ~2 °C in this region), the temperature of fluids in the discharging column ultimately sets the pressure difference (driving forces) between the outcrops.

Thus driving forces inversely dependent on flow rates, a negative feedback that establishes a functional relationship between permeability and the rate of siphon flow. For example, a decrease in k_B slows fluid flow and increases the temperature of the fluid column at the discharge site, which in turn increases the differential pressure across the siphon and thereby increases flow rates. This process could diminish or even dominate the direct impact of reducing permeability. The significance of discharge-domination in this system may additionally relate the fact that the system is barely operating as a hydrothermal siphon, or could result from the difference in size between the recharging and discharging features, as is the case for discharge-dominated systems in high-temperature hydrothermal systems [*Strens and Cann*, 1982, 1986; *Germanovich and Lowell*, 1992].

3.4 Comparison between two-dimensional and three-dimensional simulations

3.4.1 Siphon response to dimensionality

Here we present a parametric set of simulations performed in a two-dimensional geometry (2DTEST), which treats variations on both b and k_A in a similar fashion to AQTEST simulations. Volumetric flow, used elsewhere in this study to describe the magnitude of siphon flow, is not strictly defined for two-dimensional problems because volumes are inherently three-dimensional. Results in this section are instead presented in terms of mean specific discharge ($\overline{q}$), volume rate per cross-sectional area, evaluated at the surface of the Baby Bare outcrop. This metric has the benefit of being calculable for both two- and three- dimensional geometries, making it possible to compare results from similar simulations in each regime. In addition, we constrain realistic siphon behavior in two dimensions based on the system having an active hydrothermal siphon and negligible regional heat-flow suppression, as applied for three-dimensional simulations.

Results for 2DTEST simulations are presented in Fig. 3-7, along with a subset of AQTEST simulations with an equivalent (three-dimensional) geometry. A number of two-dimensional simulations sustain hydrothermal siphons, and do so with the highest flow rates associated with discharge through Baby Bare and similar values for temperature and differential pressures to those found in three-dimensional simulations. However, many flow behaviors found in three dimensions, including dipole flow and complex circulation within the Grizzly Bare outcrop (Fig. 3-4), are not possible in two dimensions. Simulations in two dimensions have significantly lower values of $\overline{q}$ (0.2 to 9.5 m/d) than those for simulations in three dimensions with commensurate properties (25 to 86 m/d). All two-dimensional simulations also produce significantly higher F_H (0.05 to 0.5) than their three-dimensional counterparts, extending well beyond observational constraints. 2DTEST simulations are also incapable of supporting hydrothermal siphons with lower values of k_A (10^{-13} to 10^{-12} m^2). That two-dimensional simulations require somewhat higher values of k_A

to support hydrothermal siphons is consistent with higher property estimates found in previous two-dimensional modeling of this system [*Hutnak et al.*, 2006].

3.4.2 Discussion of dimensionality in simulations

Two- and three-dimensional simulations generate results that are quantitatively distinct. Explicitly representing the three-dimensional system geometry significantly influences the magnitude and behavior of siphon flow, produces separate trends in response to b and k_A, and alters the range of properties under which the hydrothermal siphon can operate. Given that simulations in three dimensions strictly improve on physical and geometric accuracy, these differences in behavior alone make a strong case for the necessity of three-dimensional modeling for inferring crustal properties and other characteristics when evaluating ridge-flank hydrothermal systems.

Representing outcrop-to-outcrop systems in two dimensions restricts possible flow patterns to those within the planar model domain, removing the possibility of dipole-like flow that is typical of simulations in three dimensions (Fig. 3-4) and altering the character of local recharge and discharge within individual outcrops. This distinction results in large differences in both $\overline{q}$ and F_H due to the lack of flow paths outside of the primary flow-plane. Forcing all siphon flow to travel through a planar feature results in hydrothermal cooling being focused into relatively small region, resulting in excessive heat-flow suppression between the outcrops. This flow restriction also results in lower $\overline{q}$ since driving forces are similar in both two- and three-dimensional simulations, set by thermally derived pressure differences between the outcrops in both cases. These factors ultimately lead to higher inferred values of k_A (by 1 to 2 orders of magnitude) being required to sustain an outcrop-to-outcrop hydrothermal siphon in two dimensions.

A significant distinction between the geometries treated in two- and three-dimensional systems is that the ratio of exposure areas of the two outcrops (A_B/A_G) is different in each case, even for an otherwise identical geometry. This ratio is approximately 1/100 for Baby Bare and Grizzly Bare in three dimensions, but reducing the problem to two dimensions increases the ratio to 1/10. This ratio has been shown in earlier work to influence both siphon behavior and the property ranges capable of supporting an outcrop-to-outcrop hydrothermal siphon [*Winslow and Fisher*, 2015]. Though restricting the geometry to two dimensions affects a number of factors that may be important to overall siphon behavior (e.g., convection, dipole flow), the shift in A_B/A_G alone can account for the fact that many systems that support hydrothermal siphons when simulated in three dimensions are unable to do so in two-dimensions.

Two-dimensional simulations have a number of additional drawbacks, specifically that they cannot be used to assess fluid mass flow rates or mapped seafloor heat-flux patterns. As both of these constitute important constraints on system behavior, three-dimensional simulations are better suited for comparing model results to observational data of this kind. A two-dimensional geometry is also insufficient to represent azimuthal anisotropy (examples in three dimensions shown in the next section), and less suitable for incorporating realistic heterogeneity, bathymetry and property boundaries. Ultimately the geometry and processes intrinsic to outcrop-to-outcrop hydrothermal siphons, even those only involving two outcrops, are unequivocally three-dimensional in nature (Figs. 3-3 and 3-4). As two-dimensional models appear inappropriate to treat many aspects of this problem, and produce broadly different flow behaviors and property estimates, their use in investigating the mechanisms or behaviors associated with outcrop-to-outcrop hydrothermal siphon systems should be carefully considered.

3.5 Additional complexity in hydrothermal siphon characteristics

3.5.1 Influence of azimuthal permeability anisotropy

We apply two separate treatments of azimuthal permeability anisotropy across a series of simulations. In ANITEST-T simulations, the permeability tensor is modified to generate increased permeability in the ridge-parallel direction relative to the ridge-perpendicular direction (10:1 and 100:1), based on the idea that a regional crustal fabric runs sub-parallel to the spreading ridge to the west [*Haymon et al.*, 1991; *Fisher et al.*, 2008]. In ANITEST-F simulations, anisotropy is introduced by means of a single vertical and thin (250 m wide) region of high-permeability nodes extending from the base to the top of the crustal aquifer (300 m tall). This region runs north-to-south through the center of the model domain, and represents a permeable ridge-parallel fault or fault network. Anisotropy in both cases is applied only to the crustal aquifer, with isotropic properties assigned to the outcrops and underlying crustal section. This treatment isolates the effects of anisotropy in the crust from outcrop permeability structure, shown in OCTEST simulations to significantly impact siphon behavior (Fig. 3-6), and is supported by the fact that both outcrops were most likely formed through separate processes than the underlying crust [*Karsten et al.*, 1998; *Becker et al.*, 2000].

Flow behaviors in cases with azimuthal anisotropy in k_A differ significantly from those without, as illustrated by results for T-11x12 (Fig. 3-8). This is the only simulation from ANITEST-T that does not result in excessive heat-flow suppression, yet still has Q_S (75.2 kg/s), well in excess of observational constraints. This example shows distinctively focused flow compared to that in Fig. 3-4, with the majority of outcrop-to-outcrop flow occurring within a relatively zone range between the outcrops rather than spreading significant flow towards the boundaries of the model domain. Indirect flow paths that do exist in this case also extend much farther to the north and south of the outcrops, as the increased north-south permeability allows fluids to take longer paths in this direction with minimal energy losses. The presence of anisotropy (10:1 for T-11x12) also changes the character of convection, with focused siphon flow causing smaller secondary flow cells to coalesce into larger rolls that span tens of kilometers (Fig. 3-8).

Results for ANITEST simulations are summarized in Table 3-3, including a subset of simulations with isotropic permeability for comparison. The range of k_A that allows a hydrothermal siphon to operate varies significantly between these sets. ANITEST-T yielded hydrothermal siphons over a wide range of properties with a variety of values for Q_S and F_S, while only a single ANITEST-F simulation (F-11x12) resulted in an active siphon. Simulations from ANITEST-F/T generally yield similar (but not identical) values for Q_S and F_S compared to isotropic simulations having a comparable range of k_A. Despite similar siphon flow, most ANITEST-T simulations (with anisotropy resulting from a regional crustal fabric) result in $F_H > 0.2$, which significantly exceeds observational constraints.

The most significant effect of anisotropy in terms of observational constraints is on seafloor heat-flow, which is significantly perturbed in all but one of the ANITEST-T simulations (Table 3-3). The requirement of minimal heat flow suppression outside the immediate influence of the outcrops is more likely to be violated in cases where hydrothermal flow is channeled into a smaller region. This effect would be exaggerated by secondary impacts on convection, which further concentrate heat-flow anomalies by creating larger and more persistent discrete convective structures. Several east-west seismic reflection and heat flux lines were run north of Grizzly Bare seamount to look for evidence of heat flux suppression associated with fluid flow towards the north [*Hutnak et al.*, 2006]. Although observational data are limited, there is no evidence for suppression of seafloor heat flux as would be expected if siphon flow were focused within a narrow (east-west) region, as occurs with simulations that include regional anisotropy. In general, simulations that include crustal anisotropy tend to result in outputs that are less consistent with observational constraints than do simulations without crustal anisotropy.

Simulations based on a single planar fault to represent anisotropy (ANITEST-F) require higher permeability to sustain hydrothermal siphons than do either those with bulk anisotropy applied via the permeability tensor (ANITEST-T) or simulations with isotropic properties. This result is similar in some way to results from two-dimensional representations of this system: when the bulk of hydrothermal flow is restricted to a plane between the two outcrops, either due to a fault or two-dimensional geometry, systems preferentially form two single-outcrop flow systems rather than a connected hydrothermal siphon. Thus even if much of the fluid flow were to occur within a narrow band defined by a fault zone, it appears that interactions with the rest of the crustal aquifer may be important for accurate representation of the hydrothermal siphon.

In addition to the two treatments we presented, there are many other ways to incorporate anisotropy into this system (e.g., vertical anisotropy, anisotropy within outcrops, additional permeability ratios), and each of which seems to have significant and varied affects on siphon behavior. Given the number of free parameters introduced by attempting to reproduce the geological complexity present in this anisotropic and potentially heterogeneous system, it is likely that additional data will be required to constrain the true permeability structure of this site. Forthcoming experimental results, particularly the analysis of a tracer experiment performed in the crust north of Baby Bare [*Fisher et al.*, 2011], may better inform proper treatment of azimuthal permeability anisotropy for this field site.

3.5.2 Influence of additional crustal discharge north of Baby Bare

Though this study focuses on the dipole system operating between the Grizzly Bare and Baby Bare outcrops, there are other outcrops nearby: Mama Bare seamount is located another 16 km to the north of Baby Bare, Papa Bare is located 20 km to the northeast, and Zona Bare outcrop is located another ~50 km to the north. Though there is no direct evidence for a hydraulic connection between the Grizzly Bare to Baby Bare system and other outcrops to the north, geochemical studies suggest that there is a systematic variation in basement fluid chemistry from Baby Bare to north of Mama Bare (Wheat et al., 2000). There is no estimate of the rate of fluid discharge at these additional outcrops, but it remains possible that some fluid associated with the Grizzly Bare to Baby Bare hydrothermal siphon discharges through one or more of the northern seamounts. We explore the potential impact of this possibility with the ADDQTEST simulations (Table 3-2), which we use to constrain the quantity of hydrothermal fluid that could recharge at Grizzly Bare seamount and then flow north of Baby Bare, without perturbing the discharge at Baby Bare beyond what is allowed by observational constraints.

To represent the influence of additional northern discharge (Q_N), we include a fluid sink within the upper aquifer at the northern boundary of the domain. We use this sink to remove water from the domain at a fixed rate, and assess the quantitative impact on the Grizzly Bare to Baby Bare hydrothermal siphon. The model domain used throughout this study extends 40 km south and north of the Grizzly Bare – Baby Bare dipole, with the goal of putting the domain boundaries far away from the main seamounts of interest. Explicitly modeling additional outcrops would require a significantly larger model domain (expanded in east-west width to accommodate the expansion in north-south geometry), and would require considerably more nodes/cells and a longer runtime. We avoid these complexities with a simple parameterization that helps to elucidate fundamental behavior, as described below.

Typical flow patterns found in ADDQTEST simulations are presented in Fig. 3-9. Flow behavior is similar to those presented in Fig. 3-4 in terms of flow velocities (specific discharge), and the presence of local circulation patterns. Flow rates to the east and west of the outcrops in this case are somewhat higher, spreading the thermal influence of the hydrothermal siphon over a larger area. In addition, these indirect paths bifurcate near the Baby Bare outcrop, separating Baby Bare discharge fluids from those traveling to the site of crustal outflow and creating distinct flow paths around the outcrop. The specific pattern presented is dependent on simple representation of northward flow, but similar behaviors (larger flows along long flow-paths, bifurcation in flow) should persist in systems with additional sites of discharge.

We present three sets of ADDQTEST simulations, each with distinct aquifer permeability values (Table 3-2, Fig. 3-10). Each case uses a 300 m aquifer and a moderate permeability assignment for both outcrops ($k_G = k_B = 10^{-12}$ m^2). Hydrothermal siphons appear to be supportable for any value of Q_N provided that Q_S stays above ~15 kg/s. Below this threshold, the siphon fails and Baby Bare becomes a site of recharge for fluids flowing to the north, which distinctly violates observational constraints. Most simulations resulting in hydrothermal siphons between Grizzly Bare and Baby Bare have Q_S above observed siphon discharge from Baby Bare, with two simulations near the upper end of this range (17 and 21 kg/s). Simulations with additional northern discharge of $Q_N \leq$ 70-100 kg/s (varies with k_A) also have $F_H <$ 0.05, consistent with regional heat flux observations. Increases in Q_N monotonically decrease siphon flow, but result in greater total flow through the system ($Q_N + Q_S$). Both responses follow a roughly linear trend with Q_N, the slope of which depends on k_A.

As an ensemble, ADDQTEST simulations demonstrate that a significant quantity of additional northern discharge (> 40 kg/s) can occur in tandem with siphon flow between Grizzly Bare and Baby Bare outcrops without halting the hydrothermal siphon, and a narrow range of conditions allows this to occur without perturbing the system far outside of observational constraints. Two simulations fall on the cusp of constrained behavior, with Q_N = 40 and 130 kg/s over a small difference in k_A. In each case, Q_N is larger than Q_S, suggesting that it is possible that more water recharged at Grizzly Bare is discharged north of Baby Bare than through Baby Bare itself. The nearly linear response for each set of simulations in Fig. 3-10 informs how Q_N impacts both Q_S and the rate of hydrothermal recharge at Grizzly Bare. For example, for simulations with $k_A = 10^{-12}$ m^2, the slope (dQ_S/dQ_N) is ~ -0.5, meaning that half of the fluid flow to Q_N is drawn from the siphon (directly reducing siphon discharge from Baby Bare seamount, Q_S), whereas half comes from an increase in recharge at Grizzly Bare.

That such large flows are possible with relatively low values of F_H relates to the fact that flow in the crust north of Baby Bare seamount occurs over a broad area (Fig 9A), which distributes its influence over a large fraction of the model domain. This effect might be more pronounced if Q_N were divided among multiple distributed sources (e.g., outcrops, exposed faults) or could be greatly diminished if flow were instead concentrated into a relatively small number of discrete fractures, as may be the case in the upper ocean crust [*Fisher et al.*, 1994; *Fisher and Becker*, 2000; *Spinelli and Fisher*, 2004]. While significant Q_N appears possible in the context of ADDQTEST simulations, additional hydrologic and geochemical observations will be needed to establish the existence and nature of flow outside the Grizzly Bare – Baby Bare siphon.

3.6 Summary and conclusions

The range of properties that yield simulations consistent with observational constraints varies somewhat between each parametric set, depending on dimensionality (2DTEST) and on the inclusion of additional complexity (ADDQTEST, ANITEST). In general, simulations with $k_A > 10^{-13}$ m^2 generate outcrop-to-outcrop hydrothermal siphons, with systems with k_A from 3×10^{-13} to 2×10^{-12} m^2 being most consistent with observational constraints. A similar range is reasonable for permeability in both outcrops, and simulations with higher values for k_A and either k_G or k_B (10^{-12} to 10^{-11} m^2) tend to result in F_H and Q_S well beyond associated constraints. If discharge from Baby Bare were, in fact, somewhat higher than previously estimated, the reasonable range for permeability would be somewhat wider (3×10^{-13} to 10^{-11} m^2 for $Q_S \leq 75$ kg/s). Simulations with 600 m aquifers yield active siphons with somewhat lower values of k_A, but typically have excessive values of F_H. This is not the case for simulations with moderate to thin aquifers ($b \leq 300$ m), which therefore provide the best match to observed behaviors. Azimuthal anisotropy in k_A, as tested in ANITEST, modifies flow behavior significantly and tends to result in more substantial heat-flow suppression. The two cases where heat-flow suppression was acceptable ($F_H < 0.05$) resulted in higher siphon flow rates ($Q_S > 40$ kg/s), suggesting that anisotropic properties are less suitable for meeting the observational constraints for this system, unless the siphon discharge rate has been underestimated.

Estimates of geometry and permeability are based on simulations designed to study a specific system, and thus only strictly apply to the hydrothermal siphon system operating between the Grizzly Bare and Baby Bare outcrops. However, the most important features of this problem are fairly general: no heat-flow suppression, thick sedimentation, and significant distance between outcrops. We expect that other locations on the seafloor that share these properties should operate in a similar fashion, and that many of our findings regarding property dependencies, fluid flow patterns, and characteristics of convection should be generalizable to such cases. Though the characteristics of this site are fairly specific (including burial by thick sediments at a relatively young age), the geologic history of the crust itself (relatively young, intermediate spread-rate crust) is not excptional. As such, estimates of crustal properties and geometry may be more broadly applicable outside locations characterized by similar physics to this system. Given that F_H is highest in this study in simulations with thick (> 300 m) aquifers and high (> 10^{-12} m^2) aquifer permeability, it is likely that outcrop-to-outcrop hydrothermal siphons that do mine significant heat have one or both of these characteristics. This is also possible by simply increasing the amount of fluid circulating through the crust, which suggests that such systems may involve multiple outcrops or operate over shorter distances than in this system, as seems to be the case on average globally [*Anderson et al.*, 2012].

Future modeling work could improve on these efforts by incorporating more realistic geology into the construction of three-dimensional model domains. More realistic treatment of bathymetry and basement relief should be a priority, as both are variable but well-constrained on the eastern flank of the Juan de Fuca Ridge [*Davis et al.*, 1992; *Hutnak et al.*, 2006] and topography has been shown to significantly impact the character of hydrothermal circulation [*Hartline and Lister*, 1981; *Fisher et al.*, 1990; *Wang et al.*, 1997; *Bani-Hassan et al.*, 2012]. Beyond this, the inclusion of more geologically realistic (i.e., heterogeneously distributed) properties, by either significantly refining the current representative elemental volume approach or implementing a discrete fracture network, seems to be an obvious next step. In addition to computational difficulties with either proposal, the primary challenge at this time is lack of field data to sufficiently characterize the detailed permeability structure of the ocean crust. Without additional observations, heterogeneous property casting through geostatistical methods would introduce a number of free parameters that may not accurately reflect the physical system.

3.7 References

Anderson, B. W., L. A. Coogan, and K. M. Gillis (2012), The role of outcrop-to-outcrop fluid flow in off-axis oceanic hydrothermal systems under abyssal sedimentation conditions, *J. Geophys. Res.*, *117*(B5), doi:10.1029/2011JB009052.

Anderson, R., and M. Zoback (1982), Permeability, underpressures, and convection in the oceanic-crust near the costa-rica rift, eastern equatorial pacific, *J. Geophys. Res.*, *87*(NB4), 2860–2868, doi:10.1029/JB087iB04p02860.

Bani-Hassan, N., K. Iyer, L. H. Rüpke, and A. Borgia (2012), Controls of bathymetric relief on hydrothermal fluid flow at mid-ocean ridges, *Geochem. Geophys. Geosystems*, *13*, doi:10.1029/2012GC004041.

Becker, K., M. Langseth, and R. Von Herzen (1983), Deep crustal geothermal measurements, hole-504b, deep-sea drilling project leg-69 and leg-70, *Initial Rep. Deep Sea Drill. Proj.*, *69*(MAY), 223–235.

Becker, K., A. T. Fisher, and T. Tsuji (2013), New packer experiments and borehole logs in upper oceanic crust: Evidence for ridge-parallel consistency in crustal hydrogeological properties, *Geochem. Geophys. Geosystems*, *14*(8), 2900–2915, doi:10.1002/ggge.20201.

Becker, N. C., C. G. Wheat, M. J. Mottl, J. L. Karsten, and E. E. Davis (2000), A geological and geophysical investigation of Baby Bare, locus of a ridge flank hydrothermal system in the Cascadia Basin, *J. Geophys. Res.-Solid Earth*, *105*(B10), 23557–23568, doi:10.1029/2000JB900204.

Cowen, J. P., S. J. Giovannoni, F. Kenig, H. P. Johnson, D. Butterfield, M. S. Rappe, M. Hutnak, and P. Lam (2003), Fluids from aging ocean crust that support microbial life, *Science*, *299*(5603), 120–123, doi:10.1126/science.1075653.

Davis, E. et al. (1992), Flankflux: an experiment to study the nature of hydrothermal circulation in young oceanic-crust, *Can. J. Earth Sci.*, *29*(5), 925–952, doi:10.1139/e92-078.

Davis, E. E., and K. Becker (2004), Observations of temperature and pressure: constraints on ocean crustal hydrologic state, properties, and flow, in *Hydrogeology of the Oceanic Lithosphere*, edited by E. E. Davis and H. Elderfield, pp. 225–271, Cambridge University Press, Cambridge, UK.

Edwards, K. J., W. Bach, and T. M. McCollom (2005), Geomicrobiology in oceanography: microbe-mineral interactions at and below the seafloor, *Trends Microbiol.*, *13*(9), 449–456, doi:10.1016/j.tim.2005.07.005.

Elderfield, H., C. G. Wheat, M. J. Mottl, C. Monnin, and B. Spiro (1999), Fluid and geochemical transport through oceanic crust: a transect across the eastern flank of the Juan de Fuca Ridge, *Earth Planet. Sci. Lett.*, *172*(1), 151–165.

Fisher, A., K. Becker, T. Narasimhann, M. Langseth, and M. Mottl (1990), Passive, off-axis convection through the southern flank of the Costa-Rica rift, *J.*

Geophys. Res.-Solid Earth Planets, *95*(B6), 9343–9370, doi:10.1029/JB095iB06p09343.

Fisher, A., K. Becker, and T. Narasimhann (1994), Off-axis hydrothermal circulation : parametric tests of a refined model of processes at Deep-sea Drilling Project/Ocean Drilling Program Site 504, *J. Geophys. Res.-Solid Earth*, *99*(B2), 3097–3121, doi:10.1029/93JB02741.

Fisher, A., J. P. Cowen, C. G. Wheat, and J. F. Clark (2011), Preparation and injection of fluid tracers during IODP Expedition 327, eastern flank of Juan de Fuca Ridge, edited by A. Fisher et al., *Proc. Integr. Ocean Drill. Program*, *327*, 26.

Fisher, A. T. (1998), Permeability within basaltic oceanic crust, *Rev. Geophys.*, *36*(2), 143–182, doi:10.1029/97RG02916.

Fisher, A. T., and K. Becker (2000), Channelized fluid flow in oceanic crust reconciles heat-flow and permeability data, *Nature*, *403*(6765), 71–74, doi:10.1038/47463.

Fisher, A. T., and C. G. Wheat (2010), Seamounts as conduits for massive fluid, heat, and solute fluxes on ridge flanks, *Oceanography*, *23*(1), 74–87.

Fisher, A. T., C. A. Stein, R. N. Harris, K. Wang, E. A. Silver, M. Pfender, M. Hutnak, A. Cherkaoui, R. Bodzin, and H. Villinger (2003a), Abrupt thermal transition reveals hydrothermal boundary and role of seamounts within the Cocos Plate, *Geophys. Res. Lett.*, *30*(11), 1550, doi:10.1029/2002GL016766.

Fisher, A. T. et al. (2003b), Hydrothermal recharge and discharge across 50 km guided by seamounts on a young ridge flank, *Nature*, *421*(6923), 618–621, doi:10.1038/nature01352.

Fisher, A. T., E. E. Davis, and K. Becker (2008), Borehole-to-borehole hydrologic response across 2.4 km in the upper oceanic crust: Implications for crustal-scale properties, *J. Geophys. Res.*, *113*(B7), doi:10.1029/2007JB005447.

Germanovich, L., and R. Lowell (1992), Percolation theory, thermoelasticity, and discrete hydrothermal venting, *Science*, *255*(5051), 1564–1567, doi:10.1126/science.255.5051.1564.

Hartline, B., and C. Lister (1981), Topographic forcing of supercritical convection in a porous-medium such as the ocean crust, *Earth Planet. Sci. Lett.*, *55*(1), 75–86, doi:10.1016/0012-821X(81)90088-1.

Haymon, R. M., D. J. Fornari, M. H. Edwards, S. Carbotte, D. Wright, and K. C. Macdonald (1991), Hydrothermal vent distribution along the East Pacific Rise crest (9 09′–54′ N) and its relationship to magmatic and tectonic processes on fast-spreading mid-ocean ridges, *Earth Planet. Sci. Lett.*, *104*(2), 513–534.

Hutnak, M., and A. T. Fisher (2007), Influence of sedimentation, local and regional hydrothermal circulation, and thermal rebound on measurements of seafloor heat flux, *J. Geophys. Res.*, *112*(B12), doi:10.1029/2007JB005022.

Hutnak, M., A. T. Fisher, L. Zuhlsdorff, V. Spiess, P. H. Stauffer, and C. W. Gable (2006), Hydrothermal recharge and discharge guided by basement outcrops on 0.7-3.6 Ma seafloor east of the Juan de Fuca Ridge: Observations and numerical models, *Geochem. Geophys. Geosystems*, *7*, Q07O02, doi:10.1029/2006GC001242.

Hutnak, M., A. T. Fisher, R. Harris, C. Stein, K. Wang, G. Spinelli, M. Schindler, H. Villinger, and E. Silver (2008), Large heat and fluid fluxes driven through mid-plate outcrops on ocean crust, *Nat. Geosci.*, *1*(9), 611–614, doi:10.1038/ngeo264.

Karsten, J. L., N. Becker, M. J. Mottl, and C. G. Wheat (1998), Petrology of Baby Bare and Mama Bare lavas, *Geophys. Res. Lett.*, *25*(1), 117–120, doi:10.1029/97GL53564.

Kim, S.-S., and P. Wessel (2011), New global seamount census from altimetry-derived gravity data: New global seamount census, *Geophys. J. Int.*, *186*(2), 615–631, doi:10.1111/j.1365-246X.2011.05076.x.

Mottl, M. J. et al. (1998), Warm springs discovered on 3.5 Ma oceanic crust, eastern flank of the Juan de Fuca Ridge, *Geology*, *26*(1), 51–54, doi:10.1130/0091-7613(1998)026<0051:WSDOMO>2.3.CO;2.

Spinelli, G. A., and A. T. Fisher (2004), Hydrothermal circulation within topographically rough basaltic basement on the Juan de Fuca Ridge flank, *Geochem. Geophys. Geosystems*, *5*, Q02001, doi:10.1029/2003GC000616.

Stein, C., and S. Stein (1992), A model for the global variation in oceanic depth and heat-flow with lithospheric age, *Nature*, *359*(6391), 123–129, doi:10.1038/359123a0.

Stein, C., and S. Stein (1994), Constraints on hydrothermal heat-flux through the oceanic lithosphere from global heat-flow, *J. Geophys. Res.-Solid Earth*, *99*(B2), 3081–3095, doi:10.1029/93JB02222.

Stein, J. S., and A. T. Fisher (2003), Observations and models of lateral hydrothermal circulation on a young ridge flank: Numerical evaluation of thermal and chemical constraints, *Geochem. Geophys. Geosystems*, *4*, 1026, doi:10.1029/2002GC000415.

Strens, M., and J. Cann (1982), A model of hydrothermal circulation in fault zones at mid-ocean ridge crests, *Geophys. J. R. Astron. Soc.*, *71*(1), 225–240, doi:10.1111/j.1365-246X.1982.tb04995.x.

Strens, M., and J. Cann (1986), A fracture-loop thermal balance model of black smoker circulation, *Tectonophysics*, *122*(3-4), 307–324, doi:10.1016/0040-1951(86)90149-6.

Thomson, R. E., E. E. Davis, and B. J. Burd (1995), Hydrothermal venting and geothermal heating in Cascadia Basin, *J. Geophys. Res.-Solid Earth*, *100*(B4), 6121–6141, doi:10.1029/95JB00030.

Underwood, M. B., K. D. Hoke, A. T. Fisher, E. E. Davis, E. Giambalvo, L. Zuhlsdorff, and G. A. Spinelli (2005), Provenance, stratigraphic architecture, and hydrogeologic influence of turbidites on the mid-ocean ridge flank of northwestern Cascadia Basin, Pacific Ocean, *J. Sediment. Res.*, *75*(1), 149–164, doi:10.2110/jsr.2005.012.

De Villiers, S., and B. K. Nelson (1999), Detection of low-temperature hydrothermal fluxes by seawater Mg and Ca anomalies, *Science*, *285*(5428), 721–723, doi:10.1126/science.285.5428.721.

Villinger, H., I. Grevemeyer, N. Kaul, J. Hauschild, and M. Pfender (2002), Hydrothermal heat flux through aged oceanic crust: where does the heat escape?, *Earth Planet. Sci. Lett.*, *202*(1), 159–170, doi:10.1016/S0012-821X(02)00759-8.

Walker, B. D., M. D. McCarthy, A. T. Fisher, and T. P. Guilderson (2007), Dissolved inorganic carbon isotopic composition of low-temperature axial and ridge-flank hydrothermal fluids of the Juan de Fuca Ridge, *Mar. Chem.*, *108*(1-2), 123–136, doi:doi:10.1016/j.marchem.2007.11.002.

Wang, K. L., J. H. He, and E. E. Davis (1997), Influence of basement topography on hydrothermal circulation in sediment-buried igneous oceanic crust, *Earth Planet. Sci. Lett.*, *146*(1-2), 151–164, doi:10.1016/S0012-821X(96)00213-0.

Wheat, C. G., and M. J. Mottl (2000), Composition of pore and spring waters from Baby Bare: Global implications of geochemical fluxes from a ridge flank hydrothermal system, *Geochim. Cosmochim. Acta*, *64*(4), 629–642, doi:10.1016/S0016-7037(99)00347-6.

Wheat, C. G., and M. J. Mottl (2004), Geochemical fluxes through mid-ocean ridge flanks, in *Hydrogeology of the Oceanic Lithosphere*, edited by E. E. Davis and H. Elderfield, pp. 627–658, Cambridge University Press, Cambridge, UK.

Wheat, C. G., H. Elderfield, M. J. Mottl, and C. Monnins (2000), Chemical composition of basement fluids within an oceanic ridge flank: Implications for along-strike and across-strike hydrothermal circulation, *J. Geophys. Res.-Solid Earth*, *105*(B6), 13437–13447, doi:10.1029/2000JB900070.

Wheat, C. G., H. W. Jannasch, M. Kastner, J. N. Plant, and E. H. DeCarlo (2003), Seawater transport and reaction in upper oceanic basaltic basement: chemical data from continuous monitoring of sealed boreholes in a ridge flank environment, *Earth Planet. Sci. Lett.*, *216*(4), 549–564, doi:10.1016/S0012-821X(03)00549-1.

Wheat, C. G., M. J. Mottl, A. T. Fisher, D. Kadko, E. E. Davis, and E. Baker (2004), Heat flow through a basaltic outcrop on a sedimented young ridge flank, *Geochem. Geophys. Geosystems*, *5*, Q12006, doi:10.1029/2004GC000700.

Wheat, C. G., H. W. Jannasch, A. T. Fisher, K. Becker, J. Sharkey, and S. Hulme (2010), Subseafloor seawater-basalt-microbe reactions: Continuous sampling of borehole fluids in a ridge flank environment: SUBSEAFLOOR BOREHOLE FLUIDS, *Geochem. Geophys. Geosystems*, *11*(7), n/a–n/a, doi:10.1029/2010GC003057.

Wheat, C. G., S. M. Hulme, A. T. Fisher, B. N. Orcutt, and K. Becker (2013), Seawater recharge into oceanic crust: IODP Exp 327 Site U1363 Grizzly Bare Outcrop: seawater recharge into basaltic crust, *Geochem. Geophys. Geosystems*, *14*(6), 1957–1972, doi:10.1002/ggge.20131.

Winslow, D. M., and A. T. Fisher (2015), Sustainability and dynamics of outcrop-to-outcrop hydrothermal circulation, *Nat. Commun.*, in review.

Winslow, D. M., A. T. Fisher, and K. Becker (2013), Characterizing borehole fluid flow and formation permeability in the ocean crust using linked analytic models and Markov chain Monte Carlo analysis: Borehole Flow and Formation Permeability, *Geochem. Geophys. Geosystems*, *14*(9), 3857–3874, doi:10.1002/ggge.20241.

Zyvoloski, G. A., B. A. Robinson, Z. V. Dash, S. Kelkar, H. S. Viswanathan, R. J. Pawar, and P. H. Stauffer (2011), Software Users Manual (UM) for the FEHM Application Version 3.1, *Los Alamos Natl. Lab.*, 265.

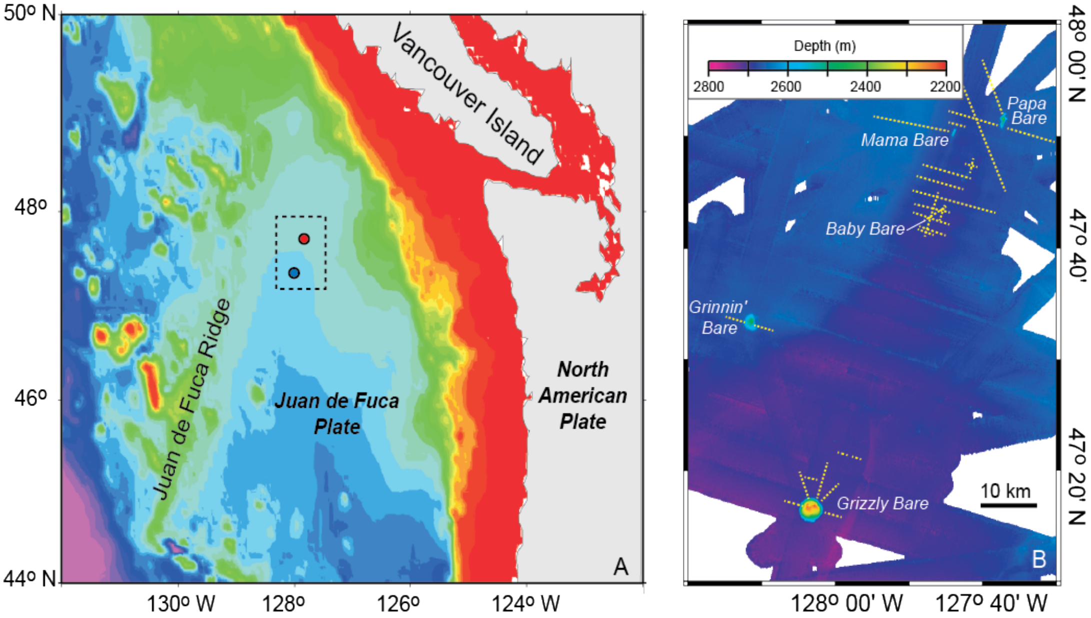

Fig. 3-1: Map of field site and observational data.
Regional map modified from [*Wheat et al.*, 2010].
A: Regional orientation to field site on the Juan de Fuca ridge flank. Blue and red dots depict locations of the Grizzly Bare and Baby Bare outcrops, respectively.
B: Locations of outcrops and collected data. Approximate locations of heat-flow measurements are shown as yellow dashed lines [*Hutnak et al.*, 2006].

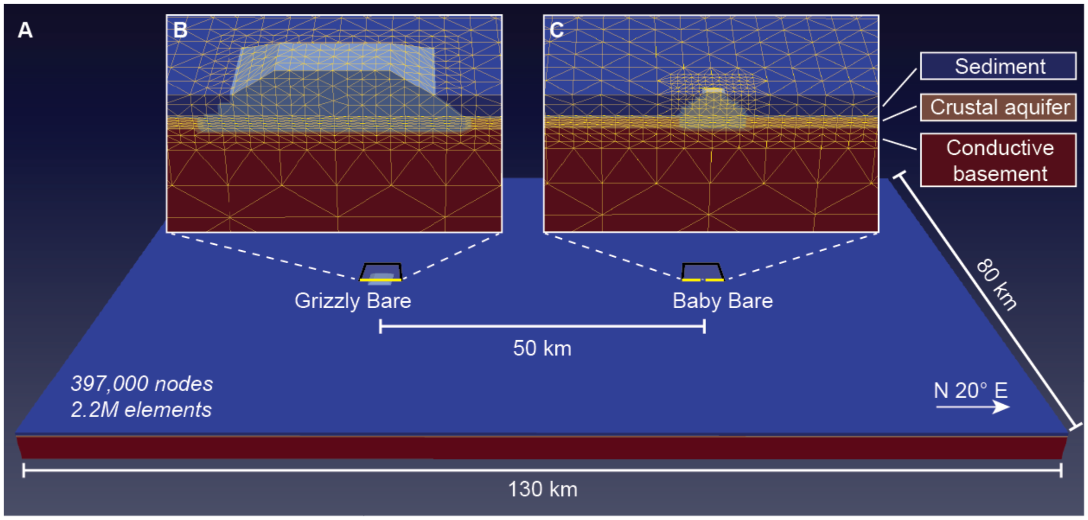

Fig. 3-2: Model domain and grid geometry

A: Full extent of model domain and dimensions. Layering shown is for 300 m aquifer; thicker and thinner aquifers extend more or less, respectively, into underlying conductive basement. Thick yellow lines and boxes around outcrops depict cut-planes and magnified regions (**B** and **C**).

B: Magnified grid near Grizzly Bare, with cut-plane through outcrop center. Yellow lines depict grid resolution, with nodes at intersections. Same scale as in **C**.

C: Magnified grid near Baby Bare, with cut-plane through outcrop center. Yellow lines depict grid resolution, with nodes at intersections. Same scale as in **B**.

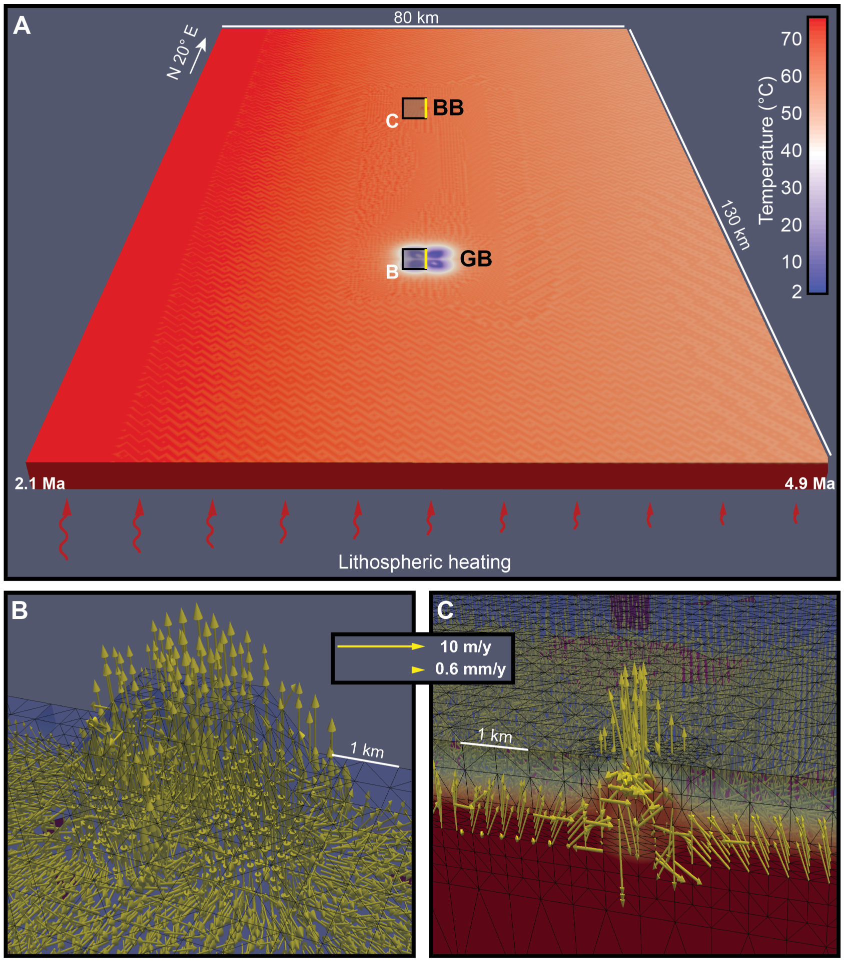

Fig. 3-3: Temperature and flow in crustal aquifer and outcrops
Simulation has isotropic properties (part of AQTEST), with $b = 300$ m and $k_A = 3\times10^{-12}$ m^2. Colors show domain temperature (2 to 70 °C).

A: Temperature map of the top of the crustal aquifer (450 m below seafloor), viewed from the south. Basal heat input is applied based on crustal age according to a lithospheric cooling curve [*Stein and Stein*, 1992], resulting in west-to-east decrease in temperature across the model domain. Coolest and warmest temperatures are associated with hydrothermal recharge and discharge, respectively, through outcrops. Thick yellow lines and boxes around outcrops depict cut-planes and magnified regions (**B** and **C**).

B: Side-perspective view (from the west) of flow pattern in Grizzly Bare outcrop with cut-plane through outcrop center. Recharge occurs near outcrop corners, with discharge near center. Lengths of flow vectors are on a natural-log scale, with largest flow (7 m/y) near the outcrop center.

C: Side-perspective view (from the east) of flow pattern in Baby Bare outcrop with cut-plane through outcrop center. Flow pattern is primarily that of discharge. Lengths of flow vectors are on a natural-log scale, with largest flow (10 m/y) near the outcrop center.

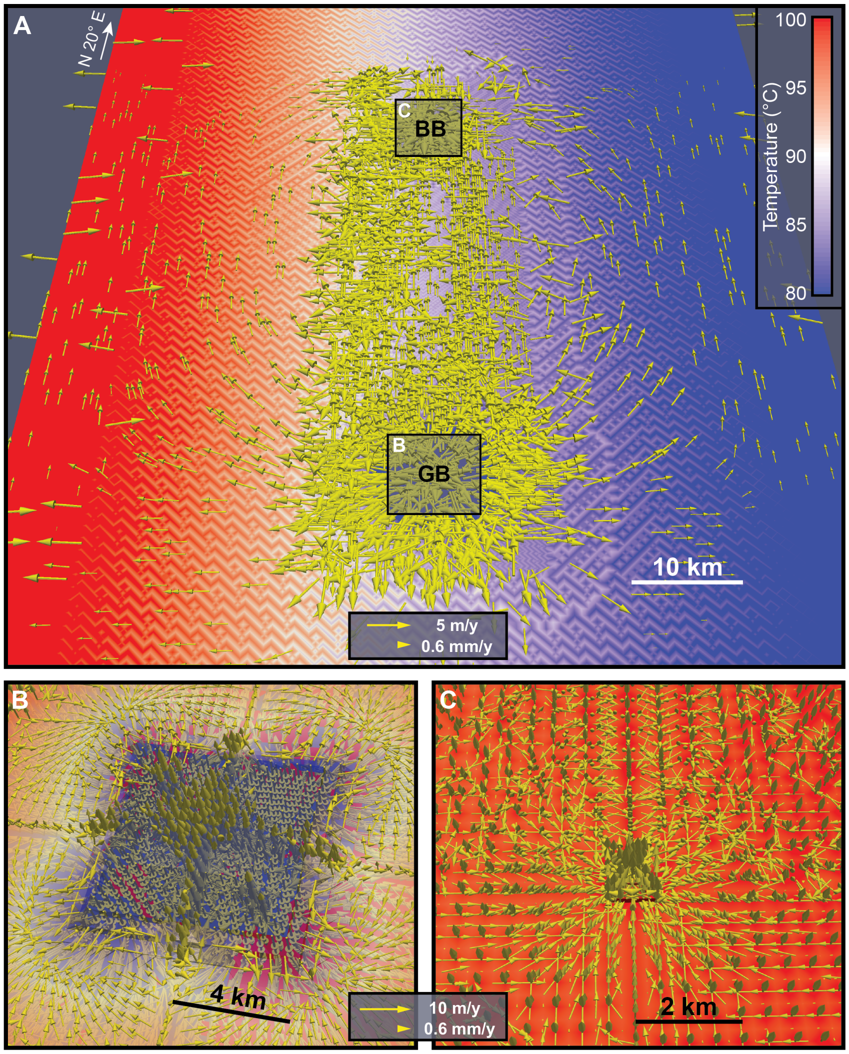

Fig. 3-4: Hydrothermal siphon dipole flow

Simulation has isotropic properties (part of AQTEST), with $b = 300$ m and $k_A = 3\times10^{-12}$ m^2. Colors show domain temperature (80 to 100 °C).

A: Top-down perspective view (from the south) of dipole flow pattern within the crustal aquifer. Flow vectors include only lateral components, with lengths on a natural-log scale. Only 3% of the flow vectors are shown, for clarity. Vector density is higher near the center of the model domain due to higher grid-resolution near the outcrops. Shaded boxes depict magnified regions in **B** and **C**.

B: Top-down perspective view (from the south) of flow pattern in Grizzly Bare outcrop and surrounding aquifer, including recharge near outcrop corners and discharge near center. Flow vectors include vertical and lateral components, with lengths on a natural-log scale.

C: Top-down perspective view (from the south) of flow pattern in Baby Bare outcrop and surrounding aquifer, which is dominantly discharging. Flow vectors include vertical and lateral components, with lengths on a natural-log scale.

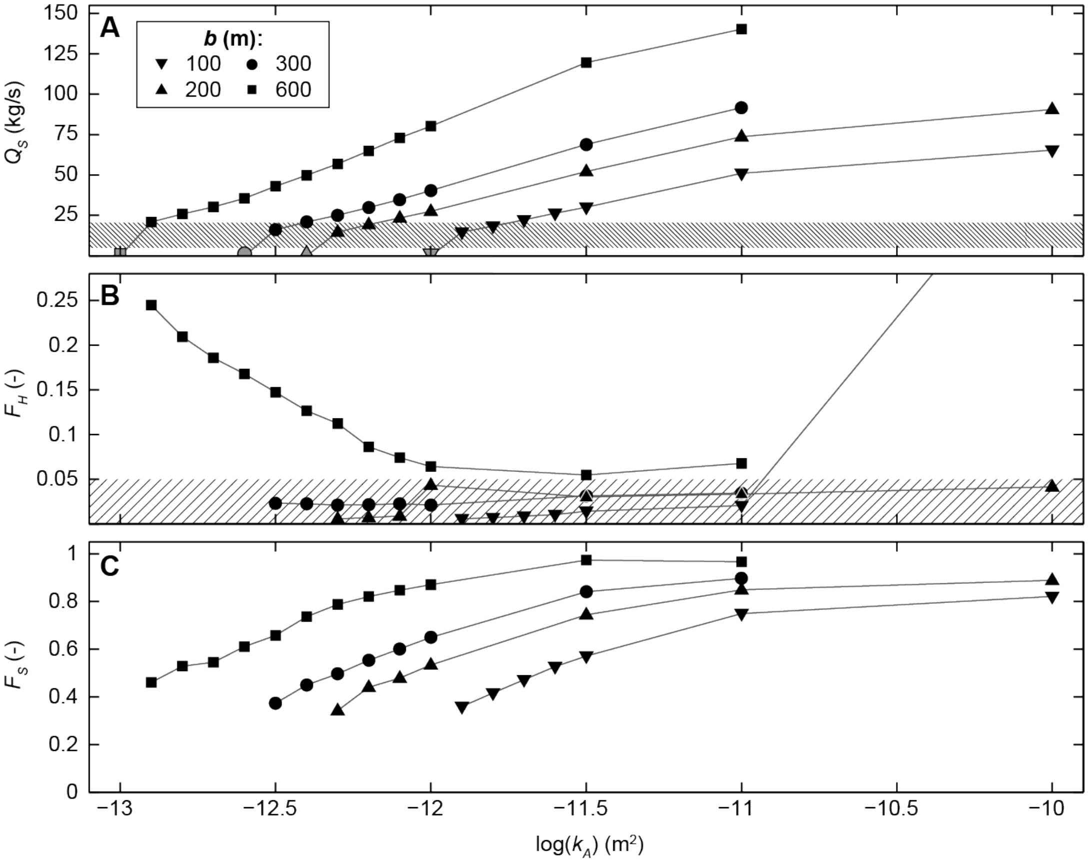

Fig. 3-5: Results from AQTEST simulations

A: Siphon flow (Q_S) by aquifer permeability, with symbol type differentiating aquifer thickness. Each symbol represents a single simulation. The shaded area is the acceptable range of siphon flow established by observations [*Thomson et al.*, 1995; *Mottl et al.*, 1998; *Wheat et al.*, 2004]. Grey symbols show the highest values of k_A for which the hydrothermal siphon fails.

B: Heat-suppression fraction (F_H) by aquifer thickness and permeability. The shaded area highlights simulations with $F_H < 0.05$.

C: Siphon fraction (F_S) by aquifer thickness and permeability.

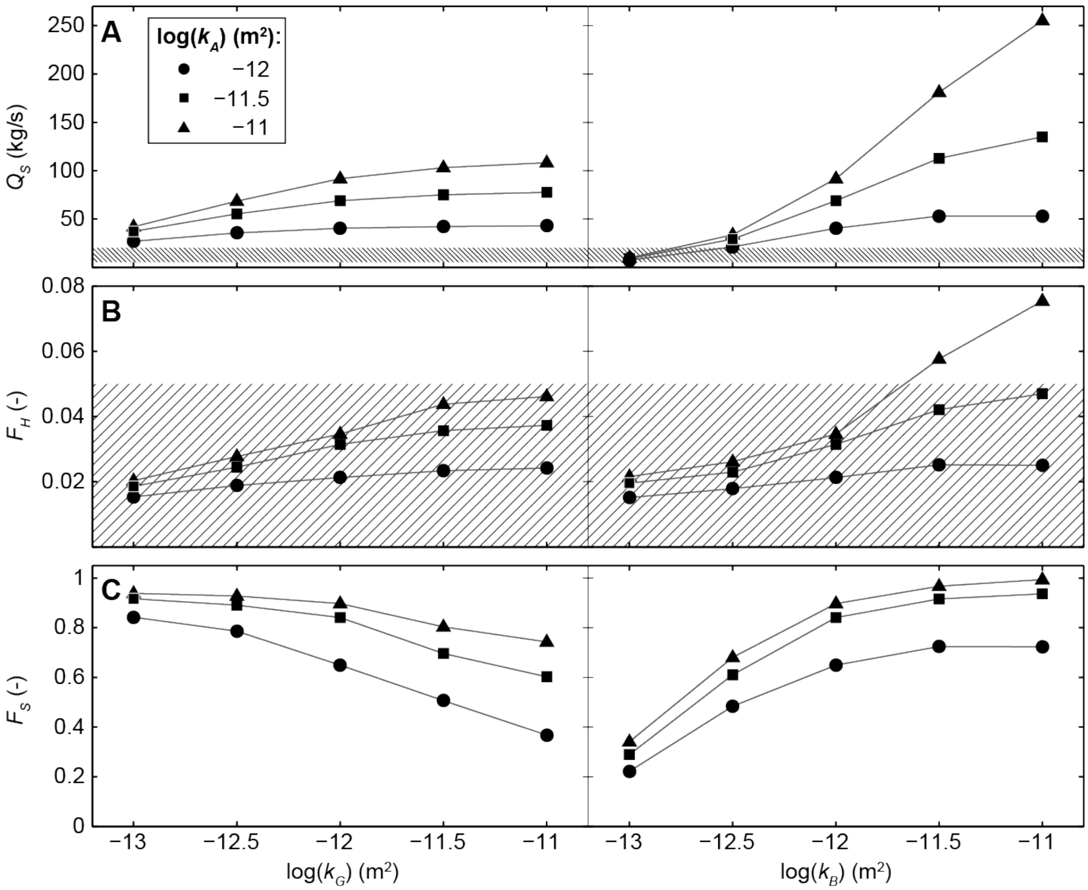

Fig. 3-6: Results from OCTEST simulations for Grizzly Bare and Baby Bare
A: Siphon flow (Q_S) by outcrop permeability for each outcrop, with symbol type differentiating aquifer permeability. Each symbol represents a single simulation. The shaded area is the acceptable range of siphon flow established by observations [*Thomson et al.*, 1995; *Mottl et al.*, 1998; *Wheat et al.*, 2004].
B: Heat-suppression fraction (F_H) by outcrop and aquifer permeability. The shaded area highlights simulations with $F_H < 0.05$.
C: Siphon fraction (F_S) by outcrop and aquifer permeability.

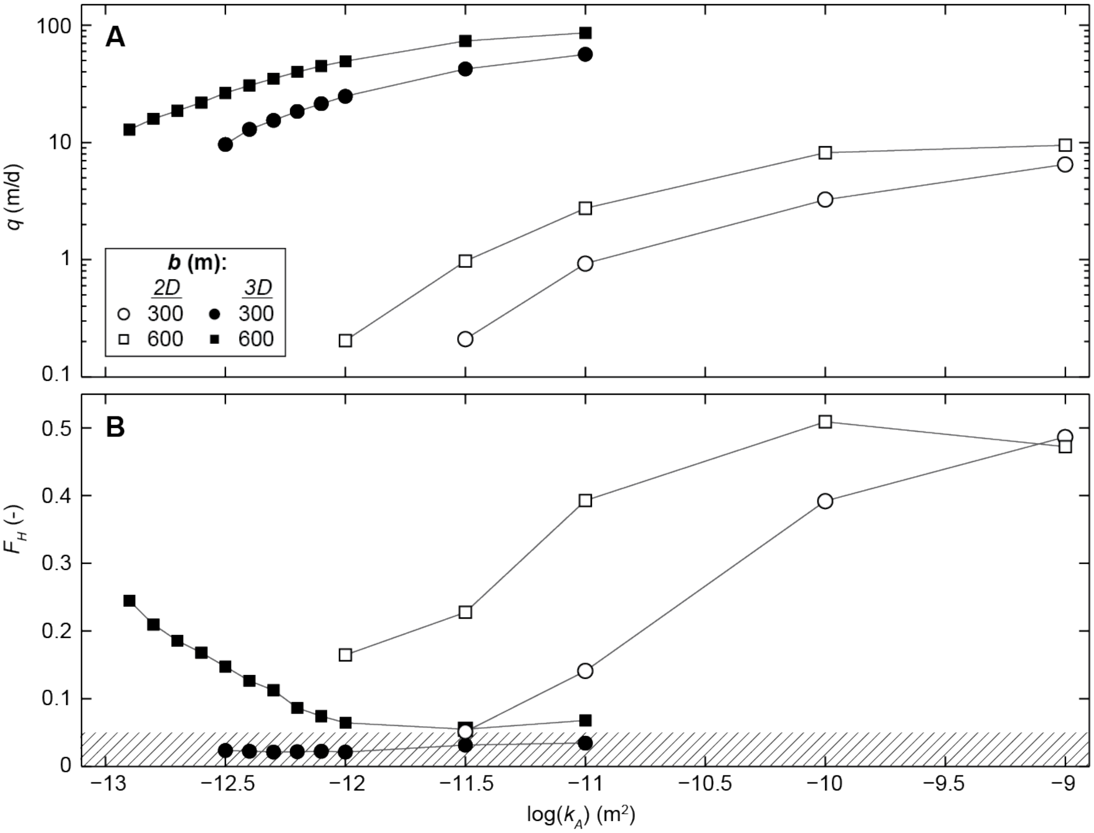

Fig. 3-7: Results from 2DTEST simulations, contrasting dimensionality

A: Mean specific discharge at Baby Bare ($\overline{q}$) by aquifer permeability, with symbol type differentiating aquifer thickness. Open and closed symbols show results from two- and three-dimensional simulations, respectively.

B: Heat-suppression fraction (F_H) by aquifer thickness and permeability. The shaded area highlights simulations with $F_H < 0.05$.

C: Siphon fraction (F_S) by aquifer thickness and permeability.

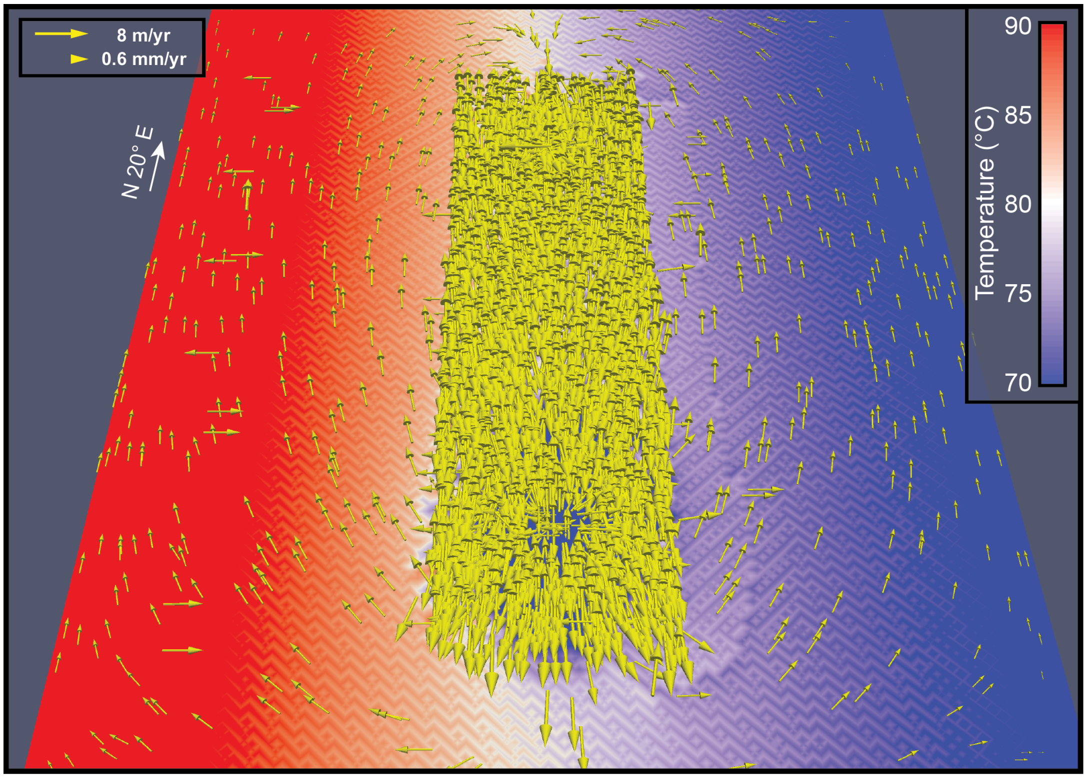

Fig. 3-8: Flow pattern with azimuthal aquifer permeability anisotropy
Simulation T11x12 (part of ANITEST; properties detailed in Table 3-3). Colors show domain temperature (70 to 90 °C). Top-down perspective view (from the south) of dipole flow pattern within the crustal aquifer. Flow vectors include only lateral components, with lengths on a natural-log scale. Only 3% of the flow vectors are shown, for clarity. Vector density is higher near the center of the model domain due to higher grid-resolution near the outcrops.

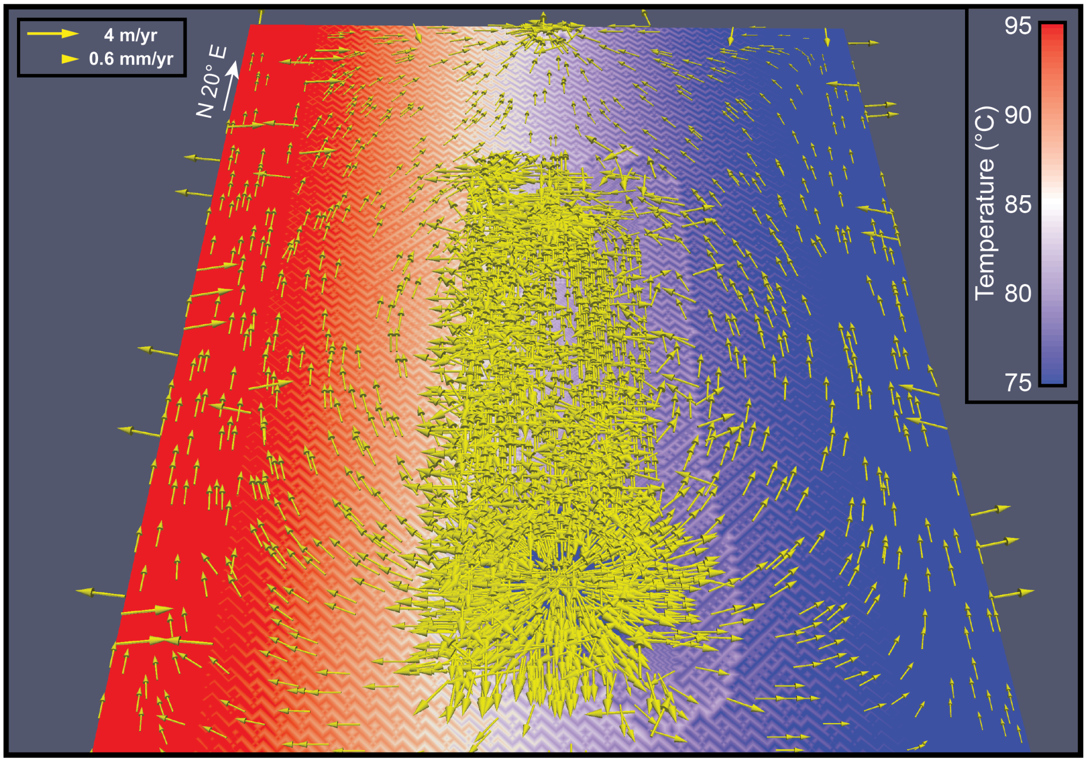

Fig. 3-9: Flow behavior with additional northern discharge
Simulation has isotropic properties and additional northern outflow (part of ADDQTEST), with $Q_N = 40$ kg/s, $b = 300$ m and $k_A = 10^{-12}$ m^2. Colors show domain temperature (75 to 95 °C). Top-down perspective view (from the south) of dipole flow pattern within the crustal aquifer. Flow vectors include only lateral components, with lengths on a natural-log scale. Only 3% of the flow vectors are shown, for clarity. Vector density is higher near the center of the model domain due to higher grid-resolution near the outcrops.

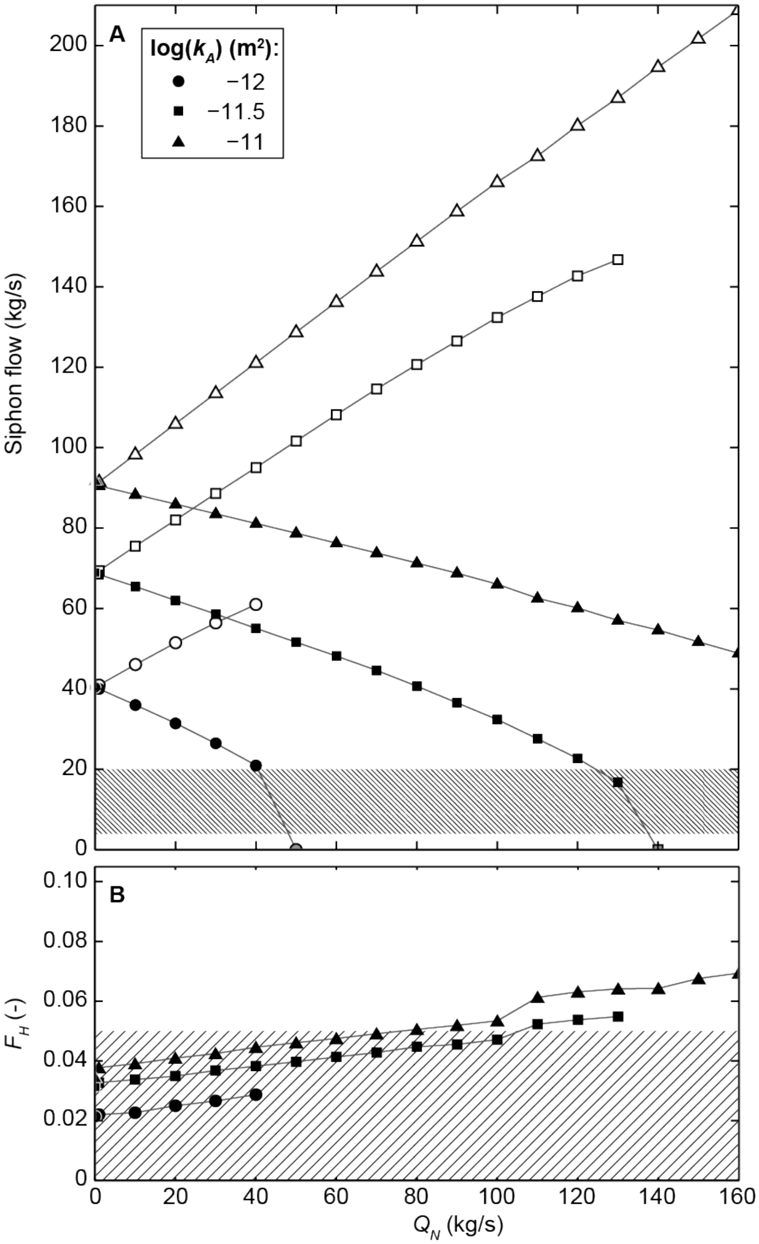

Fig. 3-10: Results from ADDQTEST simulations: additional northern discharge
A: Siphon flow (Q_S) by additional northern outflow (Q_N), with symbol type differentiating aquifer permeability. Closed symbols show Q_S only, and open symbols show the total flow through the system ($Q_S + Q_N$). Grey symbols show the minimum Q_N for which the hydrothermal siphon fails. The shaded area is the acceptable range of siphon flow established by observations [*Thomson et al.*, 1995; *Mottl et al.*, 1998; *Wheat et al.*, 2004].
B: Heat-suppression fraction (F_H) by outcrop and aquifer permeability. The shaded area highlights simulations with $F_H < 0.05$.

Table 3-1. Formation properties used in coupled-flow simulations

	Porosity, n (unitless)	Thermal conductivity, λ (W/m·K)	Permeability, k (m^2)
Sediment [a]	0.39 to 0.52	1.36 to 1.51	1.1×10^{-17} to 2.2×10^{-17}
Outcrop [b,c]	0.1	1.82	10^{-12} to 10^{-11}
Aquifer [b]	0.1	1.82	10^{-14} to 10^{-9}
Deep crust [b]	0.05	1.93	10^{-18}

[a] Values vary with depth, are consistent through all simulations. The relatively narrow range of sediment permeability applies to the full sediment column, representing a range at a smaller scale of several orders of magnitude.

[b] Values assigned homogeneously throughout each region.

Table 3-2. Geometry and parameter ranges used in parametric tests

	Aquifer thickness, *b* (m)	Aquifer permeability, k_A (m^2)	Outcrop permeability [a], k_R, k_D (m^2)	Additional northern discharge [b], Q_N (kg/s)
AQTEST	100 200 300 600	10^{-14} to 10^{-10}	10^{-12}	0
OCTEST	300	10^{-13} to 10^{-11}	10^{-12} to 10^{-11}	0
2DTEST	300 600	10^{-13} to 10^{-9}	10^{-12}	0
ANITEST	300	10^{-14} to 10^{-11}	10^{-12}	0
ADDQTEST	300	10^{-12} to 10^{-11}	10^{-12}	0 to 160

[a] Outcrop permeability is assigned homogenously within the outcrop and underlying crustal rocks, to the same depth as the crustal aquifer for each simulation.

[b] For crustal flow >0, the specified flow leaves the model at the northern boundary of the aquifer. This process is represents discharge through outcrops outside the model domain.

Table 3-3. Summary of simulations with azimuthally anisotropic permeability [a]

	High-k (m^2)	Low-k (m^2)	Siphon flow, Q_S (kg/s)	Heat-suppression fraction, F_H (unitless)	Siphon fraction, F_S (unitless)
Isotropic [b]					
AQ300-14	10^{-14}	10^{-14}	0	-	0
AQ300-13	10^{-13}	10^{-13}	0	-	0
AQ300-12	10^{-12}	10^{-12}	40.4	0.02	0.65
AQ300-11	10^{-11}	10^{-11}	91.7	0.03	0.90
Tensor anisotropy [c]					
T-12x14	10^{-12}	10^{-14}	5.5	0.34	0.14
T-12x13	10^{-12}	10^{-13}	22.7	0.30	0.46
T-11x13	10^{-11}	10^{-13}	57.1	0.24	0.77
T-11x12	10^{-11}	10^{-12}	75.2	0.04	0.86
Single-fault [d]					
F-12x14	10^{-12}	10^{-14}	0	-	0
F-12x13	10^{-12}	10^{-13}	0	-	0
F-11x13	10^{-11}	10^{-13}	0	-	0
F-11x12	10^{-11}	10^{-12}	42.5	0.04	0.69

---

[a] Aquifer thickness is 300 m for all cases, with anisotropic k_A assigned only within the aquifer. Outcrop permeability is assigned isotropically (10^{-12} m^2) in all cases.

[b] Isotropic aquifer permeability tensor. Subset of simulations presented in Fig. 3-5.

[c] Anisotropic k_A tensor: high-k in the ridge-parallel direction, low-k in the ridge-perpendicular and vertical directions.

[d] Anisotropy represented by a single high-k fault between and continuing on the far-sides of the outcrops. Low-k is used elsewhere throughout the aquifer.

CONCLUSIONS

Ridge-flank hydrothermal circulation has far-reaching consequences, including influences on ocean chemistry, the deep biosphere, lithospheric heat flux, and the evolution of the oceanic crust, all of which are ultimately dependent on the physical nature of hydrothermal flow. This thesis characterizes heat and fluid flow in ridge-flank systems by synthesizing multiple datasets to construct geologically accurate models. Chapter 1 presents the application of analytic models to estimate crustal permeability based on thermal records in flowing boreholes. This work improves on previous methods by linking a series of calculations so provide a single set of self-consistent results, and by incorporating a Markov chain Monte Carlo analysis to provide rigorous estimates on uncertainty. The first three-dimensional heat and fluid flow patterns in systems of this kind are presented explicitly in Chapters 2 and 3, describing the magnitude, vigor, and connectivity of hydrothermal flow. All chapters provide estimates for the value and structure of permeability in the upper ocean crust, quantifying a primary control on ridge-flank hydrothermal circulation globally.

Each of these studies makes significant improvements over previous work, and contributes to our understanding of ridge-flank hydrogeology. In the first chapter, we use an analytic approach to infer formation permeability from borehole thermal logs, ultimately finding that the application of a consistent approach yields a narrow range of crustal permeability across a breadth of locations. The second chapter establishes a mechanism for how outcrop-to-outcrop hydrothermal siphons self-sustain, and uses numerical methods to identify the hydrologic properties that determine whether this behavior is possible. This knowledge helps to constrain the range of properties at sites where hydrothermal siphons are active, and informs future fieldwork aimed at locating or characterizing similar systems. The third chapter focuses on a well-studied outcrop-to-outcrop hydrothermal siphon on the eastern flank of the Juan de Fuca Ridge, using three-dimensional numerical models to characterize heat and fluid flow at the site in context of field observations.

Results from the first two chapters broadly characterize the properties of ridge-flank hydrothermal systems in general. In the first case, our analytic model suggests a striking similarity in permeability estimates for the upper crust surrounding four boreholes, with all shallow crustal estimates ranging from 4 to 7×10^{-12} m^2 despite differences in location, setting, and seafloor age. The model is constructed by linking three separate analytic equations describing the thermal response in flowing subsea boreholes with an iterative model, and applying Bayesian statistical techniques to estimate the value and uncertainty in flow rates and formation permeability for each borehole. The application of rigorous statistical methods is novel in this type of analysis, and is ultimately necessary to assess the significance of the similarity between these estimates. Results from the second chapter identify the properties and conditions under which outcrop-to-outcrop hydrothermal siphons can operate. This process is not well understood and has previously only been treated with highly idealized one- and two-dimensional models, despite likely being the dominant mode of hydrothermal circulation in ridge-flank environments. The results from Chapter 2 reduce this gap by demonstrating the conditions and behaviors present in three-dimensional simulations of outcrop-to-outcrop flow.

Chapters 2 and 3 present the first results from three-dimensional coupled-flow (heat and fluid) simulations of outcrop-to-outcrop hydrothermal systems, which set a new standard by significantly improving the geological accuracy and general applicability of modeling results. Two- and three-dimensional representations are compared directly in Chapter 3, and are shown to generate widely different results in terms of fluid flow behavior and magnitude, and impact on seafloor heat flow. Given these differences, and the difficulty of relating two-dimensional modeling results to field observations that are inherently three-dimensional in nature (outlined in Chapter 3), future use of simpler representations will be difficult to justify.

As additional fieldwork continues to probe finer geologic structure and generate a more complex understanding of hydrologic processes, our models must also become more sophisticated. Our three-dimensional simulations with largely homogenous properties are a first step, and should eventually be improved with geologically realistic heterogeneous properties or through representation as a discrete fracture network, when field observations to characterize such treatment become technically feasible. Next steps for studies of outcrop-to-outcrop hydrothermal siphons include realistic (non-flat) treatment of bathymetry and basement relief, and generalizing the work done in Chapter 2 to systems influenced by multiple outcrops. Each of these should have a significant impact on outcrop-to-outcrop hydrothermal circulation, and are relevant to future work building on results from both Chapters 2 and 3. This is particularly true for the latter, which focuses on a site with substantial basement relief and a number of additional nearby outcrops. Future work for the use of flowing subsea boreholes to study crustal hydrogeology should see the model applied to additional thermal records from boreholes in other locations, which could lead to permeability estimates across a broad range of crustal settings. These projects provide insight into ridge-flank hydrogeology by elucidating the permeability structure in the ocean crust and constraining the behavior of outcrop-to-outcrop hydrothermal siphons, and have the potential to impact related work on crustal evolution, marine geochemistry, and the deep crustal biosphere.